New Technical Concepts for Velocity Map Imaging in a THz Streak Camera

Dissertation

zur Erlangung des Doktorgrades
an der Fakultät für Mathematik, Informatik und Naturwissenschaften
Fachbereich Physik
der Universität Hamburg

vorgelegt von

Mamuna Anwar

Hamburg
2018

Gutachter/innen der Dissertation:	Prof. Dr. Markus Drescher Dr. Micheal Martins
Zusammensetzung der Prüfungskommission:	Prof. Dr. Markus Drescher Prof. Dr. Daniela Pfannkuche Priv. Doz. Dr. Tim Laarman Dr. Micheal Martins Prof. Dr. Ulrike Frühling
Vorsitzende/r der Prüfungskommission	Prof. Dr. Daniela Pfannkuche
Datum der Disputation:	13. 12. 2018
Vorsitzender Fach-Promotionsausschusses PHYSIK:	Prof. Dr. Wolfgang Hansen
Leiter des Fachbereichs PHYSIK:	Prof. Dr. Micheal Potthoff
Dekan der Fakultät MIN:	Prof. Dr. Heinrich Graener

Abstract

In this dissertation the development of a novel type of streak-camera enabling multi-dimensional electron spectroscopy implying energy, angular as well as time resolution is presented. The new setup is based on a Velocity Map Imaging(VMI) spectrometer in collinear geometry for electron spectroscopy and Terahertz streaking adding time resolution to the setup. A highly efficient detection scheme being operational at comparably bad vacuum conditions allows for highest target densities up to 3 x 10^{22}/ m^3 making the setup particularly suited for low photon flux laboratory sources. The detection efficiency is explicitly calculated. In the proof of principle experiment xenon 4d photoelectrons are streaked and the ionizing and streaking pulses are characterized. Not only a successful streaking experiment has been carried out but also the work is supported by electron-optical simulations investigating the influence of the VMI DC-field on the streaking mechanism.

Zusammenfassung

In dieser Dissertation wird die Entwicklung einer neuartigen Schmierbild-Kamera vorgestellt, die eine mehrdimensionale Elektronenspektroskopie ermöglicht, die Energie-, Winkel- und Zeitauflösung beinhaltet. Der neue Aufbau basiert auf einem Velocity Map Imaging (VMI) Spektrometer in kollinearer Geometrie für die Elektronenspektroskopie und Terahertz-Schmieren, die dem Setup Zeitauflösung hinzufügt. Ein hocheffizientes Detektionssystem, das bei vergleichsweise schlechten Vakuumbedingungen betrieben wird, ermöglicht höchste Targetdichten von bis zu 3 x 10^{22}/ m^3, was das Setup besonders geeignet für Laborquellen mit niedrigem Photonenfluss macht. Die Detektionseffizienz wird explizit berechnet. In dem Beweis des Prinzipexperiments werden Xenon-4d-Photoelektronen geschmiert und die Ionisierungs- und Schmierenpulse charakterisiert. Nicht nur ein erfolgreiches Schmierenexperiment wurde durchgeführt, sondern auch die Arbeit wird durch elektronenoptische Simulationen unterstützt, die den Einfluss des VMI DC-Feldes auf den Schmierenmechanismus untersuchen.

Contents

Chapter 1

Introduction

The quest to learn about the dynamics of atoms and molecules occuring at fundamental scales has been the driver of much research in the last decades. The challenge in these studies is the ultrashort time scale down to attoseconds [1] which requires an ultrafast detection system. This is analogous to a camera capturing an image if a movement is faster than the image acquisition time: the image will be blurred and single movement steps will not be resolved. One needs a fast camera to resolve fast movements. In order to deal with this efforts are made on a number of fronts. The most important development in this regard is the realization of laser sources with few-femtosecond pulse duration.

The next important step is to set up techniques with which the process can be studied. In order to perform the investigations in a controlled way the process is initiated by a light pulse with sufficient energy. A typical technique used for this purpose is pump-probe spectroscopy [2]. In this technique an ultra-short pulse is split into two parts. A stronger part, the so-called pump pulse, is utilized to trigger a process and the other weaker part, the so-called probe pulse, is used to monitor the change generated by the pump pulse. The trick is to monitor the effect as a function of the time delay between the pump and probe pulses. Among several other processes studied using this techniques is photoemission or photoelectron spectroscopy (PES) where the electronic properties of a material are investigated by measuring the energy distribution of electrons emitted from a target [3]. The spectral resolution for photoelectrons achievable with this technique is however limited by the spectral width of the pulses [4].

Femtosecond-pulsed lasers also provide high peak intensities and enable the utilization of nonlinear processes for frequency conversion from XUV [5] to far-infrared radiation [6]. High Harmonic Generation has proven to be a well applied source of XUV [7] with pulse duration reaching down to attoseconds [1]. Moreover optical rectification has proven to be an efficient tool to fill the long-lasting THz gap due to the lack of THz-generation techniques.

For the investigation of ultrashort processes, however, the knowledge of the pulse duration is very critical [8]. Without this information the measured data cannot be evaluated correctly. Several methods have been employed for this purpose in the last years [9–11].

Light-based streaking has emerged as a novel tool with the advantage of being able to measure the pulses down to attoseconds [1]. In this technique electrons are created in the presence of a low-frequency field such that a momentum exchange occurs between the electrons and the radiation's electric field [12]. The electron distribution resembles the ionizing pulse in time. The electron generated in the presence of an external field gets

accelerated or deccelerated according to the phase of the field at the time of electron's creation, this relationship between electron wavepacket and external field is then used for diagnotics of the ionizing pulse [13]. Unlike the pump-probe technique, where a whole delay scan has to be performed in order to extract the pulse parameters, in electron streaking all the information can be attained in a single sweep, making it more robust [14]. Electron streaking, using femtosecond lasers to streak the electrons generated by attosecond pulses, has been used to study electron dynamics in real time in the last years [15–18]. By combing the electron streaking with THz science, the studies of ultrafast processes has been carried out using free electron lasers and laboratory sources of X-ray pulses with duration in few femtosecond range [19, 20].

Until now the majority of THz electron streaking experiments have relied on Time of flight (TOF) spectroscopy, which provides well-resolved electron spectroscopy. However, the initial angular distribution is not preserved due to a limited acceptance angle. On the contrary Velocity Map Imaging (VMI) spectroscopy has opened up the possibility of recording fully angle and energy resolved spectra of charged particles in a reasonable time [21]. The method first implemented by Eppnik and Parker [22] in 1997 has been extensively used in the last few years to study the dynamics of charged particles in photodissciation or photoionization experiments [23–25]. The fundamental goal of this project is to carry out the time, angle and energy resolved study of streaked electrons using velocity map imaging spectroscopy. By combining THz streaking with velocity map imaging the robustness of measuring electronic correlations can be enhanced significantly as a three-dimensional electron distribution can be collected in one measurement. By adding more dimensions in a single measurement a comprehensive investigation of the system under study is aimed.

Along with the interest in ultrashort and energy-resolved measurements, the efforts for combining various techniques such that a more complete image of the system under study can be attained in a single measurement has motivated much research. An example of this is angle-resolved Time of flight spectroscopy with various TOF spectrometers at different angles [26], adding time resolution to velocity map imaging spectroscopy [27]. In the work presented here various technical concepts are combined in order enhance the efficiency of the whole system for time, energy and angle resolved electron spectroscopy.

This work is divided into three parts: theory, experimental setup and experimental results. Chapter 2 discusses the physical basis of the work and its components. Chapter 3 describes the setup used for the measurements. Chapter 4- 6 report on the important results obtained in this work: chapter 4 deals with the characterization of the developed radiation sources, chapter 5 outlines the results on the newly-implemented velocity map imaging spectroscopy technique and chapter 6 describes the proof of principle streaking experiment with this novel setup. The work is concluded in chapter 7 with an outlook on possible future uses of the developed setup.

Chapter 2

Theoretical Background

In this chapter the focus is on the theoretical basis of different processes encountered in the project, starting with the indication of studied processes responsible for electron release from an atom in section 2.1. The targets of interest for studying electronic correlation are rare gases for which the ionization potential is some tens of electron volts (eV). The overview of the electromagnetic (EM) spectrum in Fig. 2.1 shows that this energy range lies in the eXtreme UltraViolet radiation(XUV) region.

The main light source used in this work is a commercial Ti-sapphire laser providing a fundamental photon energy of 1.5 eV. For the purpose of frequency upconversion the process of Higher Harmonic Generation(HHG) is implemented, the physical basis of this technique is described in section 2.2. The ultimate goal of this project is to study the interaction of electrons after they left the parent atom, The phenomenon is called Post Collision Interaction (PCI). This process occurs at a time scale of few femtoseconds(fs) [1] hence a time resolved observation is only possible when the ionizing pulse has a duration smaller than the time span of the effect. To generate XUV pulses with few femtosecond duration that can be used to study this interaction, the pump pulses for the HHG source are compressed using the technique of self phase modulation, details of this phenomena are narrated in subsection 2.2.3. Terahertz radiation(THz-radiation), the 0.1 - 10 THz frequency range in the EM spectrum, is required for the streaking purpose (more details on this requirement in section. 2.6), section 2.3 is dedicated to the explanation of phenomena involved in the generation and detection of THz-radiation.

The angle-resolved measurement of electrons is an important goal of this project. Section. 2.4 is dedicated to a description of angular distributions of electron emission. The theory of energy and angle resolved detection of electrons using VMI spectrometer with a brief note on the algorithms for the inversion of experimental images is described in section. 2.5. The concept of the streak-camera is described in section 2.6 where both, quantum and semiclassical model for the process are presented.

2.1 Mechanism of photo and Auger electrons release and their correlations

The light interaction with matter causes the release of electrons depending on the photon energy and the electron shell properties of the target. Here two different types of electron emission processes are considered for the purpose of studying electronic correlations. These

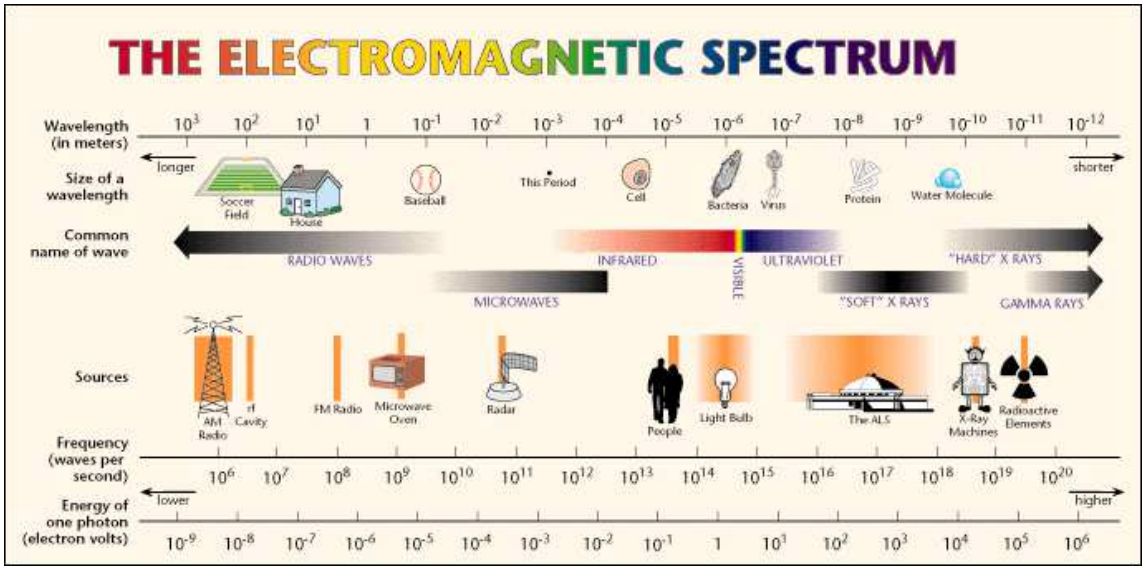

Figure 2.1: Overview of electromagnetic spectrum taken from [28]

are the direct photoionization and the Auger decay. Mechanisms of photoelectron and Auger electron emission and their correlations are explained in the following.

Direct photoionization can be explained by considering a single photon interacting with an atom such that its energy E_{ph} is higher than the ionization potential IP of a bound electron

$$E_{ph} = h\nu > IP, \tag{2.1}$$

where h is Planck constant and ν is the frequency of the photon. The photon energy is transferred to the electron and it is released into the continuum with a kinetic energy equal to the difference of the photon energy and the ionization potential. This is a linear process and a tool to determine the ionization potential of different elements after measuring the photon and electron energies.

When a photon of rather higher energy interacts with an atom such that it creates an inner shell hole, another electron from an outer shell may come in to fill the vacancy. There are also other competing processes for example fluorescence through which the excess energy can also be released. With a certain probability a third electron from an outer shell gets ionized with an energy equal to the energy difference of the two shells, this is called the Auger electron. The process is named as Auger decay and is depicted in Fig. 2.2. The nomenclature used for an Auger electron consists of the names of the shells of the involved electrons. For example in the name "KLM" the first letter K stands for the K-shell where due to initial photo-ionization a hole is created. The second letter stands for the L-shell from which the gap is filled and the third for the M shell from which the Auger electron is emitted.

The kinetic energy of the Auger electron is given by the difference of the singly ionized and the doubly ionized state. It is independent of the energy of the exciting photon. As the mechanism of Auger decay involves multiple steps it is a secondary process. The spectral width of the peaks corresponding to the Auger electrons (called Auger peaks in the text further) is determined by the exponential decay associated with the lifetime of the inner shell hole.

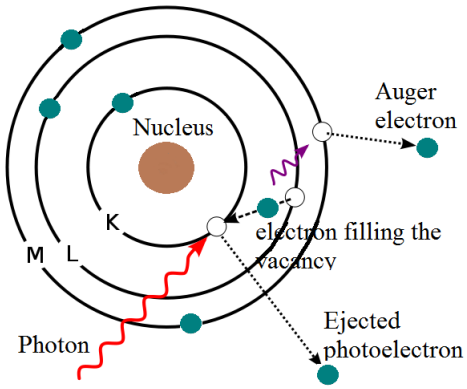

Figure 2.2: Illustration of the Auger decay. In the first step, a highly energetic photon creates an inner shell hole, another electron from a higher level comes in to fill the vacancy and the energy is transferred to a third electron which is emitted with an energy equal to the difference of the singly ionized and doubly ionized state.

Auger decay is also termed as double photoionization (DPI) where absorption of one photon leads to the emission of two electrons [29] as expressed below,

$$\gamma + X \rightarrow e + X^{+*} \rightarrow e + e' + X^{++}, \tag{2.2}$$

If the electrons do not interact with each other after emission then the Auger peaks have a Lorentzian shape. However for the case when the Auger electron is more energetic than the photo electron, and the difference in scattering angles for both electrons is small, Auger electron over takes the photoelectron and a momentum exchange occurs between the two electrons, so called PCI. It can be understood based on classical mechanics. The change in momentum of the two electrons occurs at the moment of over take as shown in Fig. 2.3.

The distance at which the PCI effect occurs depends on the difference of emission time of the two electrons. The mechanism of the interaction can be explained as following: In the final state there are three charged particles, the photo electron, the Auger electron, and the ion. All of these are still influenced by each other due to the long range Coulomb force. Due to the creation mechanism the Auger electron has a strong correlation with the photo-electron created before [30]. One reason for this correlation is the intermediate inner shell hole which is created with the emission of the photoelectron and is filled with the emission of the subsequent Auger electron. This correlation can be expressed as the probability amplitudes for creation and annihilation of this hole. Still in case where both electrons have a large energy difference the possibility of further interaction can be neglected as both electrons do not see each other after being released from the atom. However in case of comparable energies three body Coulomb interaction and electronic correlation affect the DPI process [31].

The photoelectron initially experiences the Coulomb interaction with a singly charged ion, however as the Auger electron over takes this photoelectron, it comes uder the influence of a doubly charged ion and its energy decreases. The Auger electron initially sees a doubly charged ion as it crosses the photoelectron the ionic potential for Auger electron gets shielded by the photoelectron and hence it gains energy. This change of energy leads

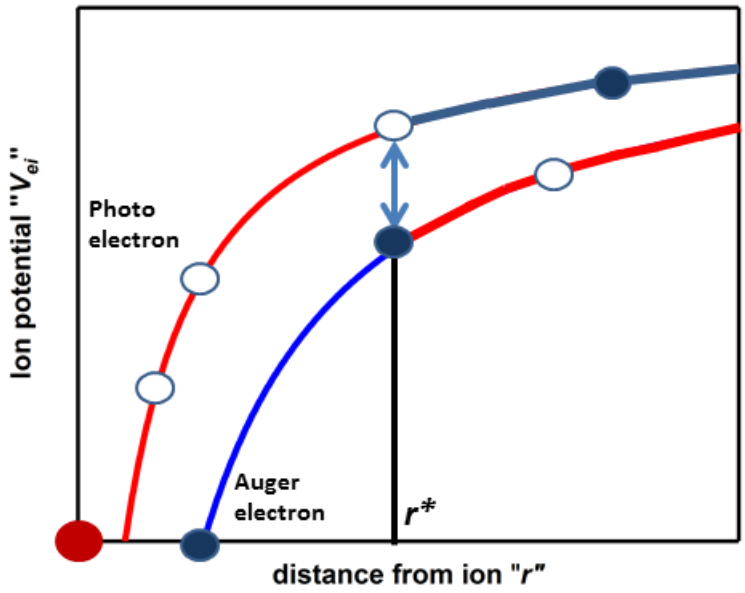

Figure 2.3: Illustration of post collision interaction phenomenon. The fast Auger electron overtakes the slow photoelectron at a distance $r*$ from the ion. At this instance both electrons exchange momentum. As a result the Auger electron gains energy and the photoelectron loses energy.

to the distortion of Auger peak making it broader and/or asymmetric, also the maximum intensity changes. All these spectral changes depend on the energy difference as well as the scattering angles of the particles with respect to the polarization axis of the ionizing photons. Angular correlation of photo and Auger electron demands a coincidence detection of both electrons and is not a subject of this work.

2.2 High order harmonic generation (HHG)

For the frequency up conversion from the infrared-radiation to the XUV-radiation, the technique of high harmonic generation (HHG) is used. This is a typical way of generating spatially and temporally coherent radiation in the vacuum ultraviolet to soft X-ray range with pulse durations down to attoseconds. The frequency of the generated radiation is an odd multiple of the fundamental frequency. Targets used for the non-linear frequency conversion are usually the noble gases [32–35]. A semi classical three step model is suggested by Corkum [36] to describe the physics of the HHG process. This model describes the microscopic effects and has found very good agreement with experiment.

2.2.1 Three step model

The model considers a single electron interacting with the laser pulse. The initial assumption for the three step model is as follows:

$$U_p >> IP >> \hbar\omega \tag{2.3}$$

where $\hbar\omega$ is the photon energy, IP is the ionization potential and U_p is the ponderomotive energy of an electron oscillating in a strong field given by

$$U_p = \frac{e^2 E_{max}^2}{4 m_e \omega^2}. \tag{2.4}$$

e and m_e are the charge and mass of the electron, E_{max} and ω are the maximum amplitude and frequency of the driving laser field. Eq. (2.4) is also called a low frequency-strong field limit [8]. In addition the model necessitates that the driving laser is linearly polarized. This model suggests that the HHG process comprised of three steps, these steps are described in the following.

Step 1 - Tunnel ionization

According to this model when the light electric field is comparable to the atomic electric field experienced by the weakest bound electron then the effective potential for the electrons is a superposition of the light and atomic potential. The modification is such that the electron can tunnel through the modified potential barrier, this is the first step in the semi classical model. To achieve this deformed potential barrier for rare gas targets the required intensity is around 10^{14} W/cm^2 [36]. The rate of tunnel ionization depends on the amplitude of the light electric field [37]. In this case the ionization or tunnelling rate is derived by Ammosov et. al (known as ADK tunnelling rate) [37] given as

$$\Gamma(t) = AIP(\frac{4\sqrt{2IP^3}}{|\varepsilon(t)|})^{2n^*-|m|-1} exp(-\frac{4\sqrt{2IP^3}}{3|\varepsilon(t)|}), \tag{2.5}$$

where $\varepsilon(t)$ is the instantaneous electric field, $IP > 0$ is the ionization potential of the atom, $n^* = Z/\sqrt{2IP}$ is the effective principal quantum number, Z is the charge of the nucleus and m is the projection of the angular momentum in the direction of laser polarization. The constant A depends on the actual and effective quantum numbers. The derivation of this expression assumes that the Keldysh parameter $\gamma = \sqrt{IP/2U_p}$ is smaller than unity. It is obvious from Eq. 2.5 that the ionization rate has a sharp maximum at times when the instantaneous field $\varepsilon(t)$ is maximum.

Step 2 - Electron acceleration

After the ionization the electron becomes quasi free. In the second step the electron accelerates in the electric field of the laser and during this acceleration it acquires energy from the laser electric field. The effect of the atomic potential is ignored as the oscillation amplitude of the electron is much higher than the atomic diameter. This acceleration of electrons can be fully described using classical mechanics. It turns out that after tunnel ionization the velocity of the electron vanishes, therefore it starts with zero velocity in the laser electric field. The electric field for a linearly polarized laser is defined as

$$\overrightarrow{E}(t) = E_0(t)\cos(\omega t + \phi)\overrightarrow{x}, \tag{2.6}$$

where $E_0(t)$ is the envelope of the field, $\overrightarrow{x}$ denotes the direction of polarization and ϕ is the phase of the electric field. The electron's acceleration in the laser's electric field can be described by the following set of equations:

$$\begin{aligned} a(t) &= \frac{eE_0}{m_e}\cos(\omega t + \phi), \\ v(t) &= \frac{eE_0}{m_e\omega}(\sin(\omega t + \phi) - \sin(\omega t_0 + \phi), \\ x(t) &= \frac{eE_0}{m_e\omega^2}(\cos(\omega t_0 + \phi) - \cos(\omega t + \phi)) - \frac{eE_0}{m_e\omega}(t - t_0)\sin(\omega t_0 + \phi), \end{aligned} \tag{2.7}$$

here t_0 is the time of release for the electron. The quantum nature of the electron allows to assume that it is released at all possible t_0 simultaneously, for each point in time there is a probability amplitude for release depending on the amplitude of the electric field at that time. Depending on t_0 an electron will follow a specific trajectory and will acquire a particular amount of energy during acceleration in the laser electric field.

Step 3 - Electron recombination and photon emission

As the oscillating electric field changes its sign there is a significant probability for the electron to recombine with the parent ion with a simultaneous emission of a photon. For this it is necessary that the laser is linearly polarized since only then an electron can recombine with its parent ion. This is the third step in this semi classical model. The energy of the emitted photon is equal to the sum of ionization potential and the kinetic energy gained by the electron from the laser field. The three steps are depicted in Fig. 2.4. Due to the quantization of energy acquired by the electron from the laser field and the condition $U_p >> IP$, the photon frequency equals to higher order multiples of the fundamental frequency. The maximum energy an electron can gain is equal to 3.17 U_p [36], this leads to a condition for the maximum photon energy achievable in HHG given by

$$E_{cut-off} = \hbar\omega_{cut-off} = 3.17U_p + IP. \tag{2.8}$$

Hence the cut-off will be different for different target gases with varying ionization potentials. In order to achieve higher photon energy, it is better to use a target gas with higher ionization potential. Moreover it is advantageous to have a higher laser intensity and hence higher energy gained by the ejected electron in the laser field. According to this model the harmonic generation is periodic in time and occurs twice every laser cycle where the electric field experiences a sign change. Due to this periodicity in time, in frequency domain this

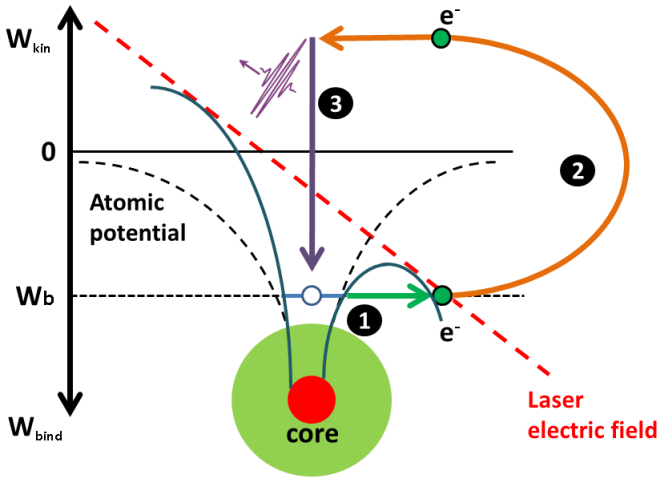

Figure 2.4: The three-step model description of HHG. In the first step an electron escapes the tunnel barrier formed by the superposition of light and atomic electric field, in the second step it accelerates in the light field and in the third step it recombines with the parent ion emitting the sum of gained energy and the ionization potential as a high energetic photon. The figure is adapted from [38]

means that only odd high harmonics of the fundamental frequency are emitted. A typical high harmonic spectrum is shown in Fig. 2.5.

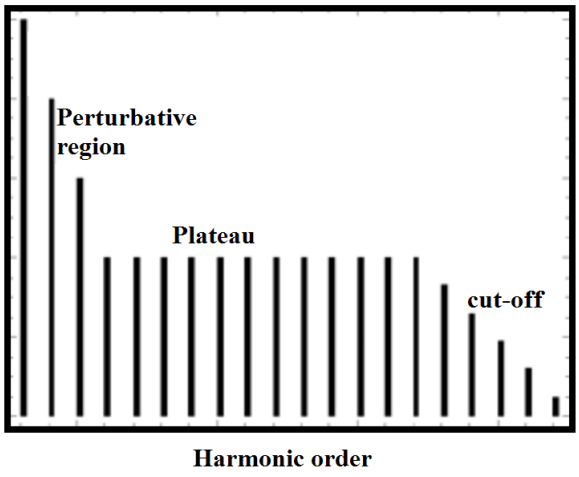

Figure 2.5: A typical high harmonics spectrum showing the pertubative region following by plateau and ending at strong cut-off.

The spectrum can be divided into three distinguishable regions namely an exponentially decaying region for lower order harmonics known as perturbation region where the intensity drops exponentially and the photon energy is below the ionization potential of the target, followed by a region of harmonics with equal intensity known as plateau and a strong cut off.

2.2.2 Macroscopic effects description

The semi classical model explains very well the microscopic effects however not the macroscopic effect including phase matching and effects emerging upon propagation like absorption, dispersion, nonlinear interaction with the medium like self focusing or plasma generation. The description of these effects requires to consider multiple atoms.

Fundamentally higher harmonic generation is a coherent process meaning at any point in space and time the phase of a harmonic can be determined from the properties of the generating laser. Due to this characteristic the harmonic intensity can increase quadratically with the number of sources (atoms of target) if they radiate in phase with each other, this is called the phase matching condition. For fulfilling this condition the driving laser and the generated harmonics should have the same phase velocity. For the following discussion the concepts are adopted from [39–42].

The approach applied to describe the propagation effects is solving the Maxwell equations for the driving laser as well as some qth order harmonic [39]. The formalism can be simplified by assuming that the medium is isotropic, non magnetic, neutral and dielectric. Moreover for the electromagnetic field a slowly varying envelope approximation is considered. For a linearly polarized fundamental and harmonic field the propagation equations with paraxial approximation are then given as [39]

$$\begin{aligned} \Delta_{\perp} E_l(\overrightarrow{r},t) + 2ik_l(\overrightarrow{r},t)\frac{\partial E_l(\overrightarrow{r},t)}{\partial z} &= 0, \\ \text{and } \Delta_{\perp} E_q(\overrightarrow{r},t) + 2ik_q(\overrightarrow{r},t)\frac{\partial E_q(\overrightarrow{r},t)}{\partial z} &= -\frac{q^2\omega_l^2}{\epsilon_0 c^2} P_q^{nl}(\overrightarrow{r},t)\exp[i(qk_l - k_q)z]. \end{aligned} \tag{2.9}$$

In the above equations E_l and E_q denote the amplitudes of the envelopes of fundamental and qth harmonic field propagating with wave vectors k_l and k_q respectively, in the medium. For the fundamental field no depletion term is included owing to the low conversion efficiency of the higher harmonics. Due to the high intensity of the fundamental the polarization of the medium has a nonlinear relation with the incident electromagnetic field, this nonlinear polarization serves as a source term for the harmonic field. This nonlinear polarization is given as

$$P_q^{nl}(\overrightarrow{r},t) = n_a(z,t)\, d_q(\overrightarrow{r},t), \tag{2.10}$$

where $n_a(z,t)$ is the atomic density and $d_q(\overrightarrow{r},t)$ is the qth harmonic component of the total atomic dipole moment that contains contributions from all active electrons [39]. For these equations a constant group velocity for laser and harmonic pulse is assumed owing due the fact that low atomic densities are used for higher harmonic generation. After this formulation of the propagation of laser and harmonic pulses the main propagation effects can be described one by one.

Absorption also plays an important role as the harmonic photons have sufficient energy to ionize the rare gas used as the generating medium. A quantitative analysis of this phenomenon can be carried out by taking into account the refractive index of the medium

at the wavelength of the qth harmonic, in particular the imaginary part of the qth harmonic wave vector namely

$$\mathrm{Im}k_q = \frac{r_0 \lambda_l f_2(\lambda_q) n_a}{q} = \frac{n_a \sigma_q}{2} \tag{2.11}$$

where λ_l is the wavelength of the fundamental radiation, $f_2(\lambda_q)$ is the imaginary part of the atomic scattering factor at harmonic wavelength λ_q and σ_q is the photoionization cross section. An absorption length can be defined as the length over which a freely propagating field is attenuated to half of its maximum. From the above expression this length is given as $L_{abs} = 1/n_a\sigma_q$.

The most important aspect encountered during propagation is the phase matching, namely matching the phase velocities of the laser and harmonic fields. In order to achieve a coherent growth of the harmonic field it is essential to avoid the destructive interference of the field corresponding to harmonics generated at successive longitudinal positions. A general phase matching condition can be stated as [43]

$$\mathbf{k}_q = qk_l + \nabla\phi_q \tag{2.12}$$

where ϕ_q is the inherent dipole phase of the harmonic. Various factors causing a phase mismatch are discussed in the following.

The electron achieves a dipole phase due to its acceleration in the laser field. This phase depends on the time the electron has for acceleration before it returns to its parent ion, hence this phase term can be approximated as $\phi_q \approx -U_p\tau \approx -I_l\theta$ where τ is the time electron is subject to the laser field, I_l is the laser intensity and the θ is the slope that depends on the electron's return time. Electrons acquire different dipole phases across the transversal beam profile of the laser as well as when they make long or short trajectories. Where an electron's trajectory depends on its time of release and the phase of the laser field at this point in time.

Focussing of Gaussian beams leads to variation of phase while propagating through the focus. This longitudinal phase change is termed as Gouy-phase. On the optical axis this phase dispersion is given as $\phi_{Gouy} = tan^{-1}(z/z_R)$ where z denotes the longitudinal axis and z_R is the Rayleigh length of the beam. For the wave vector the approximation for this geometrical phase reads

$$\Delta\mathbf{k}_q \approx -\frac{q}{z_R}\mathbf{z} \tag{2.13}$$

where $\mathbf{z}$ is a unit vector along the optical axis. For a given propagation distance in the gaseous medium the geometrical phase mismatch can be reduced by using a longer focusing length and hence increasing the Rayleigh length.

Polarization of the neutral atoms of the target medium may also cause a phase dispersion, the quantification of this factor is given as [39]

$$\Delta\mathbf{k}_{atom} \approx n_a(\pi\alpha_1\frac{q}{\lambda_l} + r_0 f_1(\lambda_q)\frac{\lambda_l}{q})\mathbf{z}, \tag{2.14}$$

where α_1 is the static polarizability and $f_1(\lambda_q)$ is the real part of atomic scattering factor, r_0 is the classical electron radius. The influence of atomic dispersion can be however neglected for low density targets used in the present work. The final factor that needs to be considered for phase matching is the influence of free electrons which also affect the propagation of the fundamental beam. This factor has a noticeable effect when a larger

number of atoms get ionized. The mathematical form of phase dispersion due to free electrons is given as

$$\Delta\mathbf{k}_{elec} = r_0\lambda_q n_e(-q + \frac{1}{q})\mathbf{z} \approx -r_0 q\lambda_l n_e\mathbf{z}, \tag{2.15}$$

where n_e is the density of free electrons. Collecting all the factors together the phase matching condition is given as

$$\mathbf{k}_q = q\mathbf{k}_l - \theta\nabla I_l + \Delta\mathbf{k}_{geo} + \Delta\mathbf{k}_{atom} + \mathbf{k}_{elec}. \tag{2.16}$$

For the purpose of achieving phase matching in the experiment the parameters optimized are gas density and the laser intensity moreover the focusing parameters and relative position of the laser focus and target is optimized. The criterion is always the maximization of the output energy of the desired harmonic order.

2.2.3 Pulse compression via self phase modulation (SPM)

In this project the pump pulses for the harmonic source are compressed to reach shorter XUV pulses as the pulse duration of the pump pulse determines the pulse duration for the XUV pulse. This is due to the fact that high harmonic generation starts at a critical intensity.

For this purpose self phase modulation in a gas filled hollow core fiber is used which is a technique discovered and in use for quite some time [44–46].

When a short pulsed laser propagates through an optical fiber the high intensity and the confinement to very small transverse dimensions lead to nonlinear effects. In particular the refractive index experienced by the laser pulse becomes a linear function of the intensity. Hence the refractive index is higher at the position of the peak intensity and decreases on either side of it. This change of refractive index is given as

$$n(\lambda, I) = n_0(\lambda) + n_2 I(t), \tag{2.17}$$

where n_2 is the nonlinear refractive index indicating the coupling between the pulse intensity and the material response, the phenomenon is usually referred to as Kerr effect. This nonlinear refractive index then changes the phase of the laser pulse, hence the pulse gets modulated by itself therefore the name "self phase modulation". The phase change is given as

$$\phi_{nl} = \frac{2\pi}{\lambda} n_2 I(t) L, \tag{2.18}$$

where λ is the wavelength of the laser and L is the physical length of the fiber. The time dependence of the the phase leads to chirping of the pulse which is proportional to $\partial\phi_{nl}/\partial t$ that is an instantaneous frequency variation inside the pulse. Now for ultrashort pulses with duration of femtoseconds and very high peak power, the instantaneous frequency can wiggle around in a range of many terahertz. The resulting frequency spectrum is given as

$$F(\omega) = \frac{1}{2\pi}\int_{-\infty}^{\infty} P(t)^{0.5} e^{i\phi_{nl}(t)} e^{i(\omega-\omega_0)t} dt \tag{2.19}$$

where $P(t)$ is the power contained in the pulse in watts and ϕ_{nl} is the term given in Eq. 2.18. Hence due to the nonlinear phase change induced by the intensity dependent refractive index new frequency components arise in the spectrum of an ultrashort pulse and a spectral broadening is achieved. However the pulse becomes chirped. After compensating the chirp using chirped mirrors the resulting pulse gets shorter than the fundamental pulse by a factor of up to 4 (40 fs to 10 fs) [47].

2.3 THz-radiation - generation and detection

The part of the electromagnetic spectrum in the THz range from 0.1 - 10 THz remained unexplored for many years due to lack of possible generation techniques. Out of the different techniques discovered in recent years, optical rectification has emerged as most efficient, this technique has significant advantages over other techniques when an ultra short pulsed laser is used as pump. The generation of THz-radiation using optical rectification was first achieved by Auston [48], this scheme is extensively used and improved till date [49–55].

2.3.1 Optical rectification

The basic process of Optical rectification (OR) discovered in 1962 [56] is the basis for THz-radiation generation in non-linear materials with less inversion symmetry [54]. OR refers to the generation of a DC polarization inside a material upon interaction with an oscillating electric field. The electric polarization of a material is related to the applied electric field through the following relation [57]

$$P = \chi(E)E, \tag{2.20}$$

where $\chi(E)$ is the electric susceptibility of the material also named as the response function. As the amplitude of the applied electric field increases the relation becomes nonlinear as higher order terms become significant, hence

$$P = (\chi^{(1)} + \chi^{(2)}E + \chi^{(3)}E^2...)E, \tag{2.21}$$

where $\chi^{(n)}$ is an nth order nonlinear susceptibility described by a tensor of rank $n+1$ with 3^n components. The OR process is connected to the second order term $\chi^{(2)}$ which is a third rank tensor with 27 components. The symmetry properties of the material decide which components of the susceptibility tensor are non-zero. In a centro-symmetric medium, $\chi^{(2)}$ is identically zero and no difference frequency generation occurs. In certain crystalline dielectrics, however, it is non-zero making them possible candidates for THz generation.

Now if the driving electric field is provided by an ultrashort laser pulse that provides a rather broad spectral bandwidth causing the mixing of different frequency components, this leads to the emission of electromagnetic radiation in the THz range [58]. For electric field $E_0\cos\omega t$ the term responsible for OR is given as

$$P_2^{nl} = \epsilon\chi^{(2)}E^2 = \epsilon\chi^2\frac{E_0^2}{2} + \epsilon\chi^2\frac{E_0^2}{2}\cos 2\omega t \tag{2.22}$$

The first term in the above equation refers to the DC polarization indicating the optical rectification of the incident optical electric field by the nonlinear electric susceptibility of the material. The second term is responsible for second harmonic generation of the incident frequency and is not relevant here. For two different frequencies the relation 2.22 is given as

$$P_2^{nl} = \epsilon\chi^2 E_1 E_2 = \epsilon\chi^2\frac{E_0^2}{2}[\cos(\omega_1 - \omega_2)t + \cos(\omega_1 + \omega_2)t] \tag{2.23}$$

The difference frequency term contributes to the THz-radiation generation, the sum frequency term corresponds to second harmonic generation and can be ignored as the phase

Material	d_{eff}[pm/V]	n_{IR}^{gr}	n_{THz}	$\alpha_{THz}[cm^{-1}]$	FOM[pm^2/V^2]
GaAs	65.6	4.18	3.61	0.5	87.9
GaP	24.6	3.57	3.34	1.9	18.2
ZnTe	68.5	3.31	3.17	1.3	180
$LiTaO_3$	161	2.22	6.42	46	882
$LiNbO_3$	168	2.23	5.16	16	1170

Table 2.1: Table showing the relevant material parameters for THz generation.

matching conditions are not fulfilled for it here. For a THz-radiation generation at a frequency Ω the polarization is given as [59]

$$\begin{aligned} P_2^{nl}(\Omega) &= \epsilon\chi^2 E_1(\omega)E_2(\omega+\Omega) \\ &\propto \Omega.d(\Omega).E_1(\omega)E_2(\omega+\Omega), \end{aligned} \tag{2.24}$$

where $d(\Omega) = \epsilon\chi^2$ is the nonlinear coefficient of the material. For an ultra short pulse Ω ranges from 0 to laser bandwidth.

2.3.2 Material selection

The material selection for THz-radiation generation requires the consideration of different aspects. As OR is a non-linear process, a large non-linear coefficient is desirable. For higher conversion efficiency the absorption of THz-radiation inside the crystal should be minimum. A higher demage threshold of the generation material is preferred so that high pump intensities can be utilized. Ideally the refractive index for optical and THz wavelength should not be too different so a collinear set-up could be realized. The relevant parameters for different materials used for THz generation are listed in table. 2.1, the values are taken from [60]. In the first column the effective nonlinear coefficients are listed, the second column gives the group refractive index at the pump wavelength of 800 nm. The third column lists the refractive indices at 1 THz. The fourth column tells the absorption coefficients again at 1 THz and the last column gives the figure of merit for given materials, which is defined as

$$\text{FOM} = \frac{d_{eff}^2}{n_{pump}n_{THz}}, \tag{2.25}$$

where d_{eff} is the effective nonlinear coefficient, n_{pump} and n_{THz} are the refractive indices in the for the pump and the THz wavelengths. $LiNbO_3$ has a large non-linear coefficient, although it has a large discrepancy in the refractive indices for optical and THz it is still a prominent candidate for THz generation. $LiNbO_3$ also has a high band gap of 3.8 eV making two photon absorption impossible when pumping at 800 nm. Two-photon absorption leads to high absorption of THz inside the generation crystal. The large refractive index discrepancy for infrared(IR) and THz-radiation presents some challenges. However some specific experimental arrangements (discussed in Subsec. 2.3.4) lead to highest conversion efficiencies at the given pump wavelength. $LiNbO_3$ also suffers from strong photorefraction, in order to suppress this it is doped with MgO which also prevents the crystal from damage at high pump irradiation [61].

There are some organic crystals like DAST [62] and BNA [63] also used as generation crystals however due to their degradation over time their use in long lasting experiments

is still a question, moreover DAST requires a pumping wavelength in the mid-infrared making it impossible to pump it directly with Ti-sapphire laser.

2.3.3 THz generation in Lithium Niobate

The main process of optical rectification in $LiNbO_3$ is impulsive stimulated Raman scattering [64]. Hereby, the fs laser pulse induces lattice vibrations which lead to the generation of THz phonon-polariton waves. The following discussion follows the description given in [19, 65].

The largest component of the nonlinear susceptibility tensor is χ_{333} giving the largest component for the nonlinear coefficient $d_{33} = \frac{1}{2}\chi^2_{333}(\Omega)$. The reason for a particularly high non-linear coefficient in this crystal is the presence of an ionic resonance in the THz range giving a frequency dependent $\chi_i(\Omega)$ as

$$\chi_i(\Omega) = \chi_{i0}(1 - \frac{\Omega^2}{\omega_i^2} + \frac{i\gamma\Omega}{\omega_i^2})^{-1}, \tag{2.26}$$

where $\chi_{i0} = 23.36$, $\gamma = 0.34$ THz and $\omega_i/2\pi$ is 7.6 THz. And the overall non-linear coefficient is given as

$$d_{33}(\Omega) = \frac{1}{2}\delta_{eee}(\Omega)\chi_e^2(\Omega)\chi_e^*(\Omega) + \frac{1}{2}\delta_{iee}\chi_i(\Omega)\chi_e(\Omega)\chi_e^*(\Omega), \tag{2.27}$$

where the coefficients (δ_{eee} and δ_{iee}) are the electronic and mixed ionic terms equal to 0.761 pm/V and 0.421 (pm/V) [66]. $\chi_e(\Omega)$ is a constant equal to 3.674 in the THz range. The dispersion and the absorption of the THz-radiation inside the generation crystal determine the possible efficiency of the generation process. For this purpose the refractive index $n(\Omega)$ and the absorption amplitude $\alpha(\Omega)$ at the THz frequency Ω are derived from the dielectric function $\varepsilon(\Omega)$ through the relations [67]

$$\begin{aligned} n(\Omega) &= Re\sqrt{\epsilon}, \text{ and} \\ \alpha(\Omega) &= (2\pi\Omega)\mathrm{Im}(\sqrt{\epsilon}). \end{aligned} \tag{2.28}$$

The dielectric function is estimated using an oscillator model as [67]

$$\varepsilon(\Omega) = \varepsilon_s + \sum_j A_j \frac{\omega_j^2}{\omega_j^2 - \Omega^2 - 2i\gamma_j\Omega}. \tag{2.29}$$

The formula for the efficiency for difference frequency mixing by long plane waves, neglecting the pump absorption and taking into account the THz absorption, reads ([68] with a correction mentioned in [69]),

$$\eta_{THz} = \frac{2\omega^2 d_{eff}^2 L^2 I_0}{\epsilon_0 n_{pump}^2 n_{THz} c^3} \exp(-\alpha_{THz}L/2).\frac{\sinh^2(\alpha_{THz}L/4)}{(\alpha_{THz}L/4)}, \tag{2.30}$$

where ω is the angular difference frequency , d_{eff} is the effective nonlinear coefficient, I_0 is the pump intensity, ϵ_0 is the vacuum permittivity, c is the speed of light in vacuum, L is the length of the nonlinear crystal, α_{THz} is the absorption coefficient for THz-radiation, n_{pump} and n_{THz} are the refractive indices of the material at IR and THz-wavelengths.

Two extreme cases can be taken into account. For the case of negligible absorption the expression for the efficiency reduces to

$$\eta_{THz} = \frac{2\omega^2 d_{eff}^2 L^2 I}{\epsilon_0 n_{pump}^2 n_{THz} c^3} \quad (\alpha_{THz} L << 1),$$

whereas for the case of a very strong absorption, the formula reads

$$\eta_{THz} = \frac{8\omega^2 d_{eff}^2 I}{\epsilon_0 n_{pump}^2 n_{THz} c^3 \alpha_{THz}^2} \quad (\alpha_{THz} L >> 1).$$

It is obvious that for the case of strong absorption the efficiency is independent of the length of the crystal. For the practical purpose the consequence is that it is useless to use a crystal length greater than the penetration depth of THz-radiation. Only those THz photons can successfully contribute to the THz emission that are produced within a region $L = \alpha_{THz}^{-1}$of the exit surface of the crystal.

2.3.4 Pulse front tilt - requirements and implementation

$LiNbO_3$ offers the highest conversion efficiency however the challenge associated with it is the large discrepancy in refractive index for infrared and THz-radiation leading to unwanted consequences. First of all optical and THz-radiation travel with different velocities inside the crystal causing the loss of phase matching hence decreasing the conversion efficiency. On the other hand the THz-radiation travels away from the pump radiation with an angle Θ_c such that

$$\cos\Theta_c = \frac{n_{NIR}^{gr}}{n_{Thz}} \tag{2.31}$$

resulting in the emergence of radiation from the crystal in a cone with opening angle equal to Θ_c and it is very challenging to collect them as depicted in Fig. 2.6.

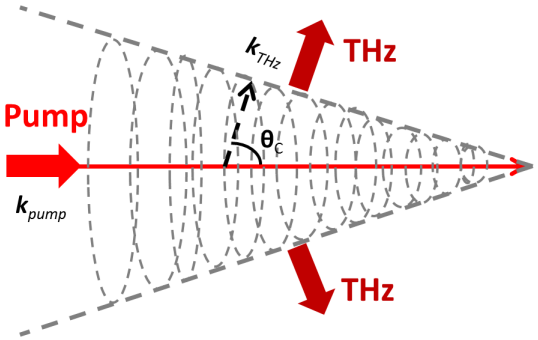

Figure 2.6: Cheronkov radiation emitted as a cone with opening angle Θ_C because the group velocity of the pump radiation is greater than the phase velocity of the emitted radiation. $\mathbf{k}_{pump}$ and $\mathbf{k}_{THz}$ are the wave vectors for pump and THz-radiation respectively. Figure adapted from [70].

.

Moreover generation of THz-radiation at a given wavelength requires a spot size for the pump beam considerably smaller than the wavelength for THz-radiation and can not be

scaled up to achieve higher output due to distructive intereference of radiations generated at different lateral positions along the pulse.

The tilted pulse front technique provides a solution to all of these problems as proposed in [71]. The THz-radiation generation process in Lithium niobate using tilted pulse front has been extensively studied experimentally [67, 72–75] as well as theoretically [76, 77]. By tilting the pulse front with respect to the propagation direction the phase velocity of the THz-radiation is matched with the group velocity of the pump radiation. This tilting angle is given as

$$\cos\Theta = \frac{\mathbf{v}_{THz}^{ph}}{\mathbf{v}_{NIR}^{gr}}. \tag{2.32}$$

where $\mathbf{v}_{THz}^{ph}$ is the phase velocity of THz-radiation and $\mathbf{v}_{NIR}^{gr}$ is the group velocity of pump beam. Once phase matching is achieved, THz-radiation is emitted as plane waves perpendicular to the pulse front.

In order to tilt the pulse front a diffractive element like a grating can be used. The resulting tilt angle depends on the orientation of the grating with respect to the incoming beam as shown in Fig. 2.7.

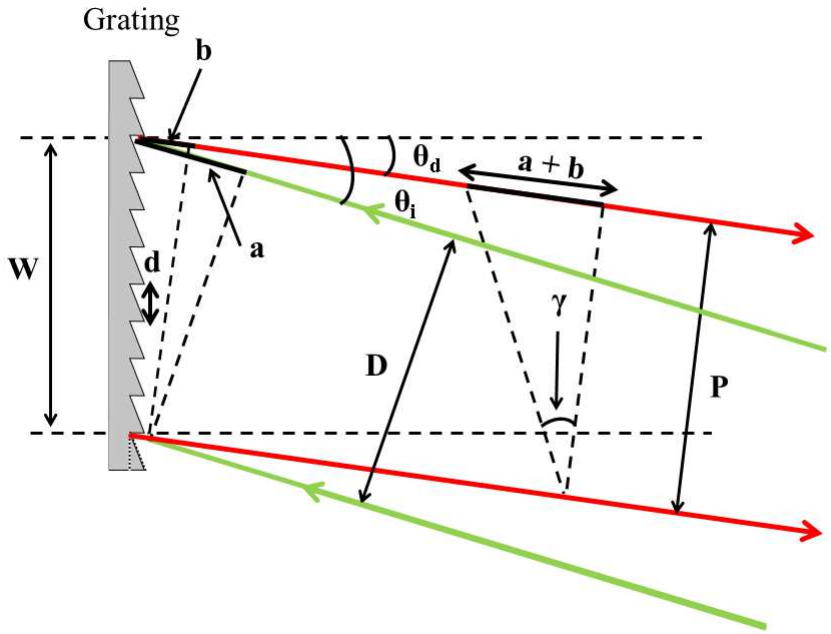

Figure 2.7: A tilt of the pulse front introduced both by the orientation of the grating and diffraction angle θ_d of it. The outgoing beam travels an additional optical path $a+b$ causing the pulse front of the beam to deviate from the phase front. (Figure adapted from [65].)

The resulting tilt angle is given as

$$\tan\gamma = \frac{\lambda}{d cos\theta_d} = \lambda \frac{d\theta_d}{d\lambda} \tag{2.33}$$

where λ is the wavelength of pump beam and d is the grating period and θ_d is the diffraction angle. As the grating disperses the spectral components spatially, a recollection of all component is done using an imaging optics (a converging lens) which introduces a demagnification M and hence a modification of the tilt angle given as

$$\tan\gamma^{'} = M\lambda\frac{d\theta_d}{d\lambda}. \tag{2.34}$$

The final factor affecting the tilt angle is the refractive index alteration when the beam enters the crystal. Hence the final tilt angle Θ inside the crystal can be calculated as

$$\tan\Theta = \frac{M}{n_g}\lambda\frac{d\theta_d}{d\lambda}, \tag{2.35}$$

where n_g is the group refractive index of $LiNbO_3$ for the 800 nm pump beam. For the given values of $n_g = 2.25$, $\lambda = 800$ nm, $d = 500$ nm for 2000 lines/ mm, $M = 2$ the tilt angle is $\Theta = 63°$and the corresponding angles for incoming and outgoing beams are $\theta_i = 44°$and $\theta_d = 66°$. With these parameters an optimal conversion efficiency can be achieved [78].

2.3.5 Electro-optical sampling

Electro-optical sampling(EOS) is a special technique used to characterize the electric field of a THz field in the time domain and hence measures its amplitude as well as its phase [79]. It is the most efficient technique [80,81] that can be used for a broad frequency range [57]. It is based on the Pockels effect. For the following discussion of the physical basis of this process, the concepts are borrowed from [57, 65, 68, 79, 82, 83].

For an isotropic material the induced polarization is linearly related to the incident electric field through a scalar susceptibility (Eq. 2.20) and is parallel to the electric field. On the other hand an anisotropic material has a direction-dependent susceptibility and hence is represented by a tensor. The relationship between electric field and material polarization for such a case is

$$P = \epsilon_0\chi_{ij}E_j. \tag{2.36}$$

The choice of the coordinate system with respect to the crystal lattice determines the coefficients of the tensor. Through a linear orthogonal transformation of the co-ordinate system the tensor matrix can be diagonalized, The new co-ordinate system is referred to as principal axes system. In this system the χ_{ij} are given as

$$\chi_{ij} = \begin{bmatrix} \chi_{11} & 0 & 0 \\ 0 & \chi_{22} & 0 \\ 0 & 0 & \chi_{33} \end{bmatrix}. \tag{2.37}$$

A birefringent behaviour is observed if not all χ_{ii} are equal resulting in different indices of refraction n_e and n_0 for polarizations parallel (extraordinary) and perpendicular(ordinary) to the axis of anisotropy, that is the axis along which the isotropy is broken. The dielectric permittivity ϵ_{ij} is related to the susceptibility χ_{ij} through the relation

$$\epsilon_{ij} = 1 + \chi_{ij}, \tag{2.38}$$

hence equation 2.36 can be re-written for electric displacement field D_{ij} as

$$D_{ij} = \sum_j \epsilon_{ij}E_j, \tag{2.39}$$

using the same argument for permittivity as for susceptibility it can be stated that for an anisotropic medium the polarization of outgoing beam get modified except the case where the polarization is parallel to one of the optical axes of the crystal. For any other direction of polarization, the electric field vector get decomposed into an extraordinary and an ordinary component which propagate with different velocities through the crystal. The difference of velocities leads to a phase shift between the two orthogonal components, consequently a change of polarization occurs after propagation through the crystal.

In order to quantify this change of polarization for high electric field of the incident beam here also higher order terms needs to be considered such that

$$P = \epsilon_0(\chi^{(1)} + \chi^{(2)}E + \chi^{(3)}E^2 + ...)E = \epsilon_0\chi E. \tag{2.40}$$

The refractive index with applied field n can be related to the refractive index n_0 without field as

$$\begin{aligned} n^2 &= \epsilon = 1 + \chi \\ &= 1 + \chi^{(1)} + \chi^{(2)}E + \chi^{(3)}E^2 + ... \\ n^2 &= n_0^2 + \chi^{(2)}E + ... \\ &= (n_0 + \Delta n)^2 \\ &\approx n_0^2 + 2n_0\Delta n \\ &. \end{aligned} \tag{2.41}$$

The last expression above is the mathematical form of the Pockels effect giving the change of refractive index.

Assuming a constant THz field in time $E_k(\omega \sim 0)$ the polarization component can be expressed as

$$P_i^{(2)} = 2\sum_{j,k} \epsilon_0\chi_{ijk}^{(2)}(\omega = \omega + 0)E_j(\omega)E_k(\omega \sim 0), \tag{2.42}$$

hence the $\chi^{(2)}$ signal is linear with respect to the optical probe field $E_j(\omega)$ as well as the THz field $E_k(\omega \sim 0)$. Conversely the electric field amplitude can be deduced from the measured field induced birefringence.

Now from 2.39 the electric field component E_i can be expressed as

$$E_i = \sum_j \eta_{ij}D_j, \tag{2.43}$$

where $\eta_{ij}(= \epsilon_{ij}^{-1})$ is the impermeability tensor. The electro-optical tensor r_{ijk} is related to η_{ij} by

$$\eta_{ij} = \sum_k r_{ijk}E_k. \tag{2.44}$$

η_{ij} is a real and symmetric tensor that means $\eta_{ij} = \eta_{ji}$ and hence it consists of only six distinct terms. Therefore it can be recast using a single index h that runs from 1 to 6.

$$\eta_h = \sum_k r_{hk}E_k \tag{2.45}$$

The change of refractive index in response to the THz electric field E_k can be written as

$$(\Delta\frac{1}{n^2})_h = \sum_{k=1}^{3} r_{hk}E_k \tag{2.46}$$

where k = 1,2,3 denotes the direction of the applied field and r_{hk} is the simplified notation of the electro-optical tensor, whereas the index h runs from 1 to 6.

The most sensitive crystal for low frequency THz detection is Zinc Telluride (ZnTe) [84, 85]. The electro-optic tensor of ZnTe has only one independent entry [79]

$$r_{hk} = \begin{bmatrix} 0 & 0 & 0 \\ 0 & 0 & 0 \\ 0 & 0 & 0 \\ r_{41} & 0 & 0 \\ 0 & r_{41} & 0 \\ 0 & 0 & r_{41} \end{bmatrix}. \tag{2.47}$$

A THz field changes the refractive index in a certain direction. Hence the index ellipsoid gets modified in size and orientation. An initially linearly polarized beam will get elliptically polarized after propagation through the crystal. The intensity difference ΔI of the corresponding polarization components for the case $n_0^2 r_{41} E_{THz} << 1$ can be calculated from

$$\Delta I(\alpha, \phi) = I_P \frac{\omega n^3 E_{THz} r_{41} L}{2c} (\cos\alpha \sin 2\phi + 2\sin\alpha \cos 2\phi) \tag{2.48}$$

where I_p is the intensity of probe beam, ϕ is the angle between the optical probe beam polarization and the [110] axis of ZnTe, ω is the frequency of the probe pulse, and L is the crystal thickness and α is the angle between the polarization of THz beam and the [110] axis of the crystal [65]. The maximum value of the trigonometric functions in Eq. 2.48 is achieved when ($\alpha = 0°$and $\phi = 0°$or $90°$) . Numerical values for the electro-optic coefficient and the refractive index of ZnTe are r_{41} = 4.04 pm/V and n_0 = 2.854 [86]. For 800 nm wavelength the frequency is given as ω = 2.36 x 10^{15} Hz for the probe beam. The THz electric field can be calculated using

$$E_{THz}[\mathrm{MV/m}] = \frac{1.36}{L[\mathrm{mm}]} . \frac{\Delta I_{max}}{I_P} \tag{2.49}$$

this formula can be used for small intensity changes ($\Delta I_{max} << I_P$). Hence electro-optical sampling can be used for mapping the THz electric field and also the maximum electric field can be estimated for fields upto 4 MV/m with the here used 0.3 mm thick ZnTe crystal. For the measurement of even higher fields either the over rotation of the signal has to be included in the analysis or a thinner crystal should be used to reduce the phase retardation [65]. The full temporal waveform of the THz can be constructed by varying the time delay between the probe and THz beams.

2.4 Angular distribution of electron

The spatial distribution of electrons created by polarized light depends on its kinetic energy and the single or multipohoton transition selection rules.

The angular dependence of the electron distribution ionized by a linearly polarized light is described by the following expression [87]:

$$I(\Theta) = \sum_n \beta_{2n} P_{2n}(\Theta), \tag{2.50}$$

where n is the number of involved photons, β_{2n} is the asymmetry parameter, P_{2n} is the Legendre polynomial used to describe the angular distribution of electrons and Θ is defined as $\cos(\Theta) = \hat{p}.\hat{e}$ where $\hat{p} = \mathbf{p}/p$ is the direction of electron momentum and $\hat{e}$ is the direction of polarization of the radiation [88]. The presence of angle dependent terms in Eq. 2.50 shows that photoionization does not produce a homogeneous distribution over all angles [89].

For single photon interaction the second order Legendre polynomial is $P_2 = \frac{1}{2}(3\cos^2\Theta - 1)$ and the limits for β_2 are given as

$$-1 \leq \beta_2 \geq 2 \tag{2.51}$$

For $\beta_2 = -1$ the maxima of the angular distribution follow the direction perpendicular to the light polarization. For $\beta_2 = 0$ the electrons are distributed homogeneously over all angles and there is no maxima of angular distribution and for $\beta_2 = 2$ the maxima of electron angular distribution follow the direction of light polarization and most of them travel along the direction of polarization.

2.5 VMI spectroscopy

First introduced by Chandler [90] and greatly improved by Eppink and Parker [22] VMI spectroscopy is a rather young but already a competitive spectroscopy technique.

Generally in a VMI spectrometer the original 3-Dimensional (3D)electron distribution (named as Newton's sphere) is projected on a 2-dimensional (2D) position sensitive detector with the help of an imaging electric field. The electric field is generated by applying electric potentials on two out of three plates whereas the third plate is grounded. This electric field is constant in time and inhomogeneous in space so to form a lens, the electric field contours are shown in Fig. 2.8. A VMI focuses the electrons such that all electrons with same velocity are focused to one single radial distance from the center of a 2D detector as shown in Fig. 2.9.

In the following the understanding of the physical basis of VMI is presented in steps based on the occurance of events. The concepts are taken from [22, 23, 91–93].

2.5.1 Newton sphere formation

It is necessary to consider the initial distribution of electrons formed as a results of photoionization. Typically a light beam with sufficient photon energy interacts with a target and causes electrons from different shells to be released. The total energy of the system is distributed between the final products as kinetic and internal energy.

Now electrons fly in different directions and after accumulation of several electrons a spherical distribution in velocity space is formed which is the so called Newton spheres for the process. The radius of these spheres depend on the initial kinetic energies of electrons. Typically the laser polarization axis serves as the axis of symmetry and directionality in the process as depicted in Fig. 2.10 where polarization axis is x-axis, The surface pattern of the Newton sphere indicates the angular distribution of electron with respect to the symmetry axis leading to inhomogeneous distribution (as mentioned in section. 2.4) as shown on the right side of Fig. 2.10.

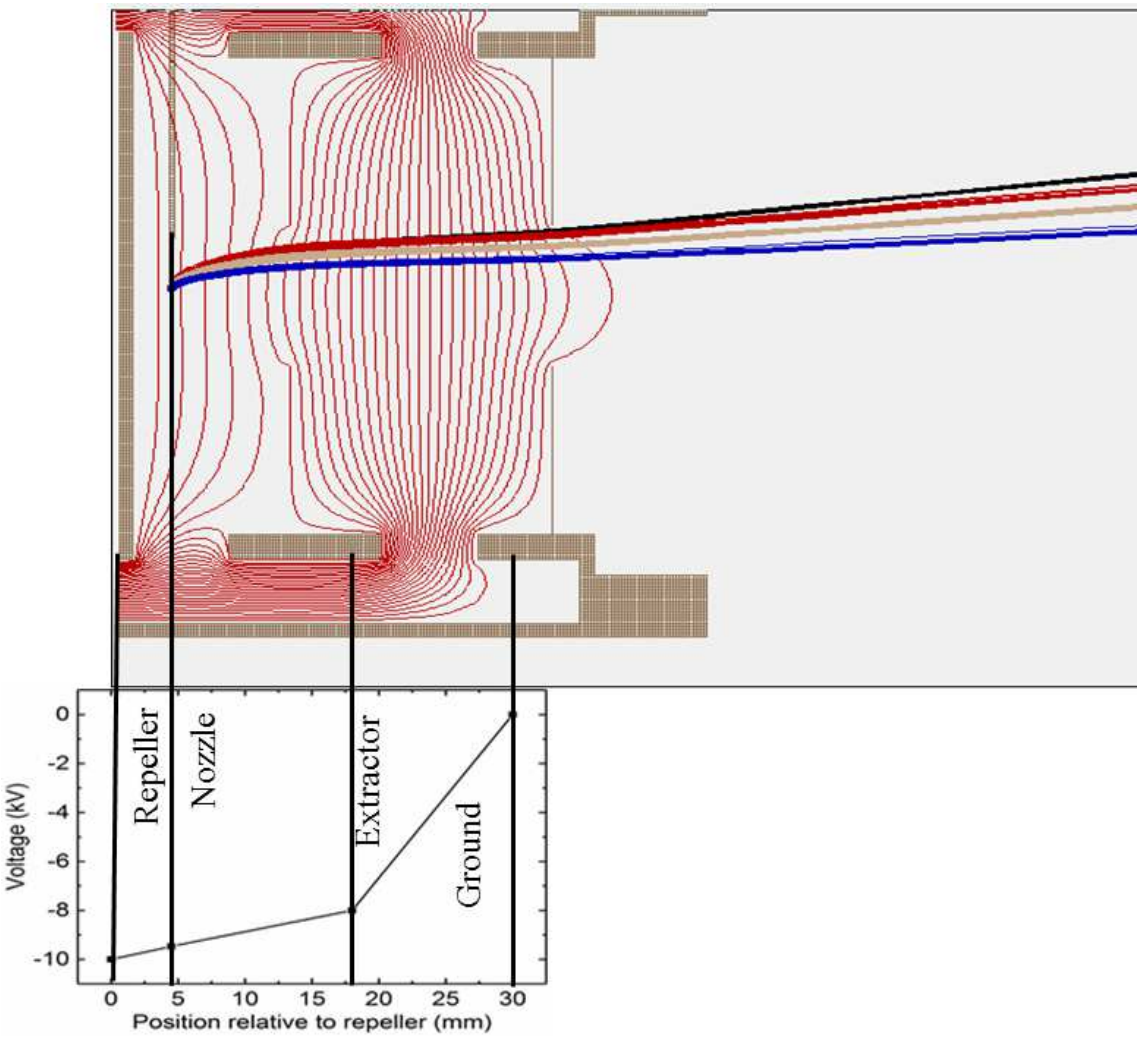

Figure 2.8: Depiction of inhomogeneous electric field distribution in a VMI lens, the red lines are some of the electric field contours, the electron trajectories for 20 eV, 40 eV, 60 eV and 80 eV are depicted in blue, yellow, red and black colour respectively.

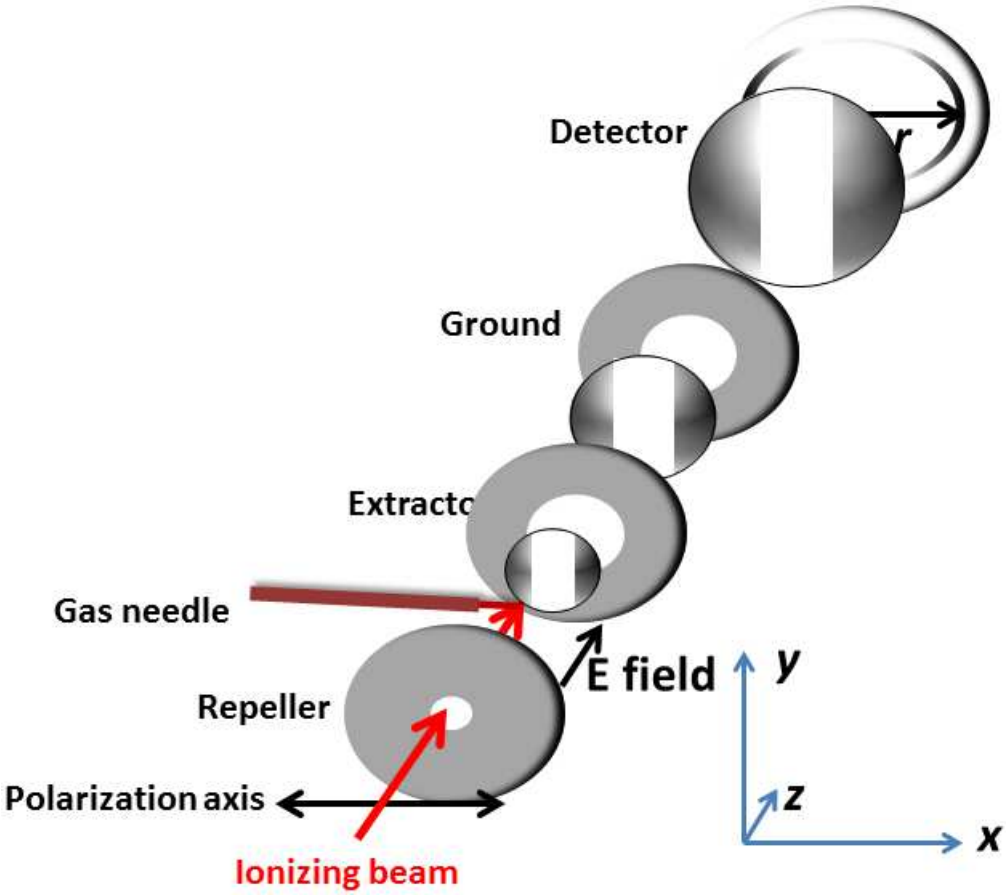

Figure 2.9: Illustration of basic principle of VMI. An ionizing radiation interacts with a target (provided through the gas needle in present case) and creates a distribution of electrons. The distribution is projected to a 2D PSD. All electrons with same velocity are mapped to a certain radial distance r from the detector center, where r is proportional to the initial velocity.

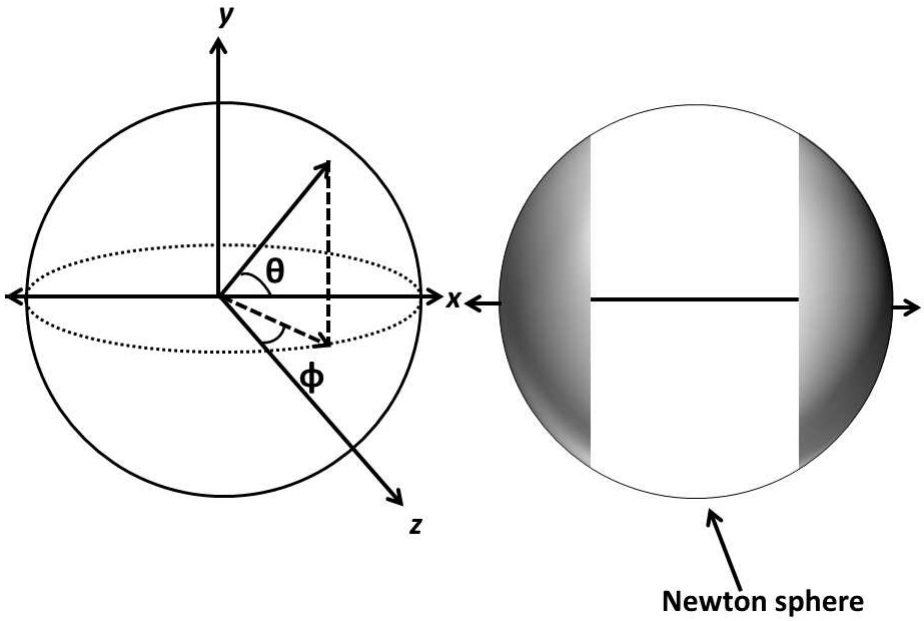

Figure 2.10: Formation of a newton sphere in cartesian and spherical coordinates. Electrons with a certain energy appear on a sphere of a specific radius. Here x-axis is the polarization axis and the symmetry axis for electron distribution. A surface pattern appear after accumulation of several events (shown on the right side). Most of the surface intensity is at the poles which is a typical $\cos^2\theta$ distribution.

2.5.2 Projection onto a two dimensional screen

An ionizing beam interacts with target atoms in between the two electrodes, see Fig. 2.9, and forms multiple Newton spheres of electrons. A VMI spectrometer basically consists of three electrodes provided with potentials to produce an inhomogeneous electric field affecting the trajectories of the electrons up to the detector. The potentials on the electrodes are adjusted so that the whole assembly behaves as a lens for the electron's velocity. This means the VMI field bends the electron trajectories such that all the electrons with the same velocity are focused to the same point on a 2D-detector, placed far away from the electrodes assembly, regardless of the initial spatial position. With this arrangement the original 3-dimensional distribution is squashed onto the 2D-detector where it appears as a partially filled circle (due to the angular distribution section. 2.4) as depicted in Fig. 2.11.

It is critical for the accurate capture of the Newton spheres that nothing disturbs the electron velocity during its flight towards the detector. Only then the 2D-image can be related to the original 3d-distribution.

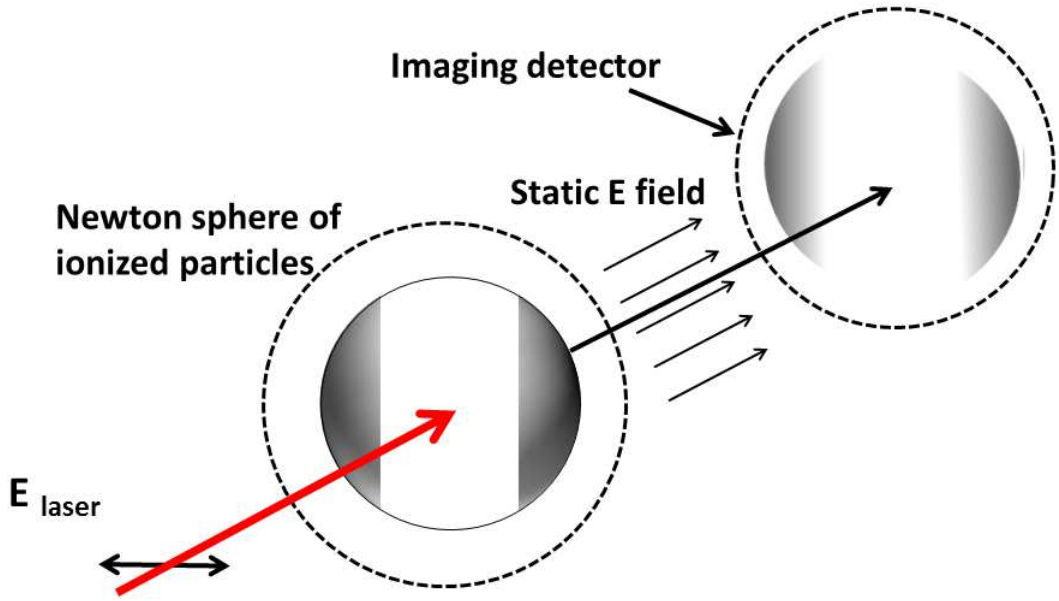

Figure 2.11: Imaging of a Newton sphere. The laser propagation direction is chosen such that the polarization vector remains parallel to the detector. Figure reproduced from [23].

In this way one measurement provides information about velocities over all angles.

2.5.3 Assigning a kinetic energy to a measured electron distribution

For the measured electron distributions the radius is related to the initial kinetic energy of the particles and the angle with respect to the symmetry axis corresponds to the initial ejection angle with respect to the polarization axis. In order to assign a kinetic energy value for electrons their radial distance of flight is measured at the detector(given that the detector is set to a fixed distance from interaction point: radial distance depends on electron's initial kinetic energy). The higher the kinetic energy the larger is the distance covered by the electron, consequently it hits the detector further away from the center. The electric fields and the geometry of the electrodes determine the time-of-flight toward the detector.

A very simple analytical model is established for the VMI spectrometer with three electrodes described in the following, see Fig. 2.12, where a single electron trajectory in the VMI setup is shown. R is the electrode with repelling voltage, E is the electrode with extractor or focusing voltage and G is the grounded electrodes. For the detection of electrons the electrodes are provided with negative voltages and the ratio of the repelling and focusing voltages needs to be optimized in order to achieve better focusing conditions of electrons of the same energy and hence higher resolution of the whole setup. A higher VMI field focuses the electrons closer to the center of the detector. The distance of the electron impinging point from the detector center is

$$r = vt, \tag{2.52}$$

where v and t are the electron's radial velocity and time of flight, respectively. Now the electron's flight to the detector can be divided into two parts depending on the fields it experiences as

$$t = t_s + t_d \tag{2.53}$$

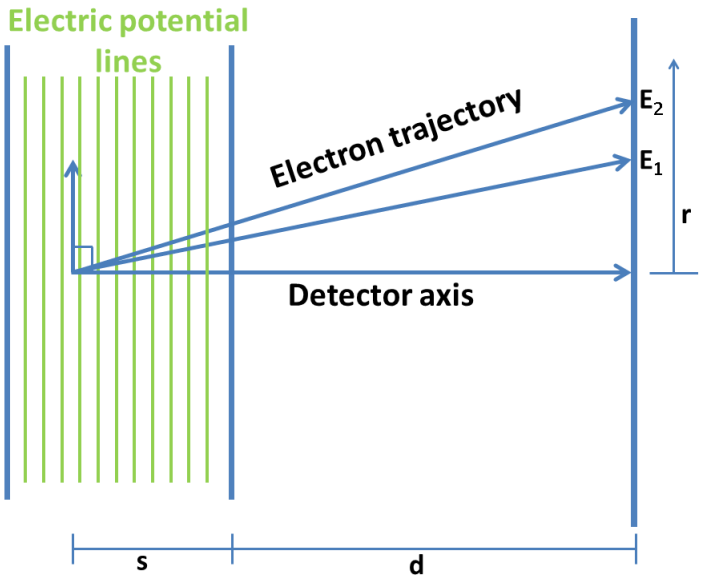

Figure 2.12: Electon trajectories inside velocity map imaging spectrometer. s corresponds to the distance covered by an electron in regions with electric field whereas d is the distance covered in field free region where $E_2 > E_1$

where t_s is the time of flight in an electric field and t_d is the time for a field-free flight. Using basic formulas of classical mechanics and electromagnetism the following relation between the radius of the measured electron distribution and electron's kinetic energy is achieved

$$r = a\sqrt{E}. \tag{2.54}$$

Here a is a constant which depends on the VMI configuration and the distance of the detector from the electrode assembly. An electron with higher energy will be detected at a larger distance from the detector center as shown is Fig. 2.12.

Compared to the conventional time of flight spectroscopy VMI spectroscopy has several advantages. The main advantage is that VMI preserves the original angular distribution of the electrons and measures electron velocity and angular distribution simultaneously. Moreover no variation of the experimental setup is required in case the linear polarization of the ionizing radiation gets rotated. Another feature associated with VMI spectroscopy is that by changing the polarity of the applied voltages and connecting the detector to an oscilloscope the setup can be used as a ion time of flight spectrometer.

2.5.4 Image inversion Algorithms

Some general dynamic information, for example the initial kinetic energy or the ejection angle can be extracted by a simple inspection of the primary images obtained from the VMI. However, these images are in fact projections of the initial 3D-distribution onto a 2D-screen. In order to extract all the information potentially avaible in this data, one needs to consider techniques to reconstruct the 3D velocity distribution for the charged particles created in the experiment.

When a linearly polarized ionizing radiation is used a cylindrical symmetry is present in the generated electron distribution and most of the electrons are ejected with cylindri-

cal symmetry about this polarization axis, as shown in Fig. 2.11, following the $\cos^2(\Theta)$ distribution (refer to section. 2.4).

When the symmetry axis is set parallel to the detector then an inversion method can be used to reconstruct the 3D-distribution giving the momentum vector associated with the electrons. Only under this condition the 2D-projection on the detector contains enough information to reconstuct the full 3D-distribution. A mathematical procedure like an inverse Abel transform [94] can recover the 3D-momentum distribution from the 2D-projection.

The data presented in this theses are reconstructed using two image inversion methods. The first approach is the one proposed by Vrakking [95] which produces a 2D-slice out of the initial 3D-distribution after processing the 2D-image. The other approach is the polar onion peeling method proposed by Robert [96] which is proved to be more efficient for our datasets. Both methods are briefly described in the following.

Vrakking inversion code

This method is based on the fact that there is a close relationship between the 3D angular and velocity distribution and the measured 2D angular and radial distribution. Here the inversion problem is treated as a single 2D to 2D problem with one radial and one angular distribution. An iterative procedure is developed that gives a converged 3D velocity and angular distribution.

The main advantage of this iterative procedure is the fact that the noise in the inversion, which is usually projected onto the symmetry axis of the 3D velocity and angular distribution, is projected toward the center of the image, where it generally does not interfere with the observation of important features in the image. The formalism is described in Appendix. A.

Polar onion peeling (POP)

This code is a combination of onion peeling using polar coordinate [97] and a basis set expansion in polar coordinates [98]. The formalism is explained in Appendix. A. The method is computationally faster than Vrakking code.

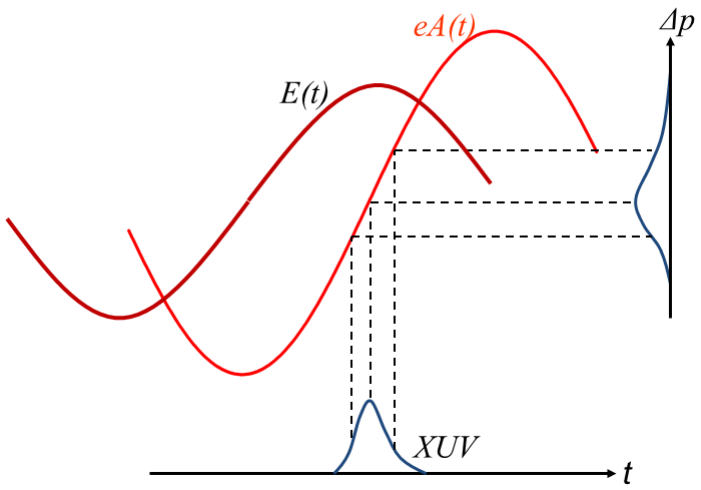

Figure 2.13: The principle of electron streaking by the electric field associated with a light pulse. Figure adapted from [101].

2.6 THz streak camera

In a conventional streak camera [99] a light pulse hits a photocathode and generates an electron bunch with a temporal distribution identical to the light pulse itself. These electrons travel perpendicular to a time dependent electric field after which they are detected by a position sensitive detector. Electrons are deflected by the electric field by different amounts depending on the phase of the electric field at the time they interact with the field. In this way the time and phase information is imprinted on a spatial axis [13]. From the spatial image of the streaked electrons and the slope of the electric field, it is possible to extract the temporal structure of the ionizing pulse. Here, the time resolution depends on the speed of the electronics generating the time-varying electric field and the ultimate limit is the spread of the electron transit times due to a spread in their initial momenta, the best resolution reported by this technique is 200 fs [100].

This resolution obtained with the conventional streaking technique is not enough for characterizing few femtosecond long light pulses. For that purpose, a new idea is implemented where the electric field of another light pulse is used to deflect the electrons as shown in Fig. 2.13.

Both semiclassical and quantum mechanical formalism give equivalent results. In the following the quantum and semi classical description of the light field driven streak is given with ideas taken from [1, 11–13, 20, 83, 102–104].

2.6.1 Quantum mechanical model

For the quantum mechanical description of the streaking effect the fundamental principle of wave particle duality is used [11]. For the formulas stated here atomic units are used where $e = m_e = \hbar = 1$ where e is electron's charge, m_e is electron's mass and $\hbar$ is Planck's constant. The ionization of an atom by an X-ray field is considered and the single active electron approximation is applied that is all electron-electron interactions in the atom are

neglected. Implementing the first-order perturbation theory, for times large enough for the X-ray field to vanish, the amplitude of the transition probability $a_{\mathbf{v}}$, from the ground state to the final continuum state $|\mathbf{v}>$ with momentum $\mathbf{v}$, is given by

$$a_v = -i \int_{-\infty}^{+\infty} \mathrm{d}t \mathbf{d}_{\mathbf{v}} \mathbf{E}_X(t) \exp[i(W + IP)], \tag{2.55}$$

where $W = \mathbf{v}^2/2$ is the energy of the final continuum state, $\mathbf{E}_X(t)$ is the electric field of the X-ray pulse, $\mathbf{d}_{\mathbf{v}}$ is the element of the dipole transition matrix from the ground to the $|\mathbf{v}>$ state and IP is the ionization potential of the atom.

Eq. 2.55 relates the electron's wave packet to the X-ray spectrum that promotes it in the continuum. It shows that the electron spectrum a_v is directly related to the X-ray field spectrum, both in phase and amplitude.

The two spectra might have different amplitudes given that $|\mathbf{d}_{\mathbf{v}}|$ depends on $\mathbf{v}$. The ionization cross-section is well known in general, therefore one can correct for this dependence.

The phase difference between the two spectra is neglected because of the negligible phase dependence of $|\mathbf{d}_{\mathbf{v}}|$ on $\mathbf{v}$ as the bandwidth of X-ray pulse is not too large. With these considerations, the electron wave packet can be viewed as a replica of the X-ray field. Hence the characterization of the electron wave packet provides all the information on the temporal structure of the X-ray field, given that the response of the atom used as a converter is known.

Now the influence of the low frequency THz field can be taken into account. For this purpose the influence of the ionic potential on the electron dynamics after ionization can be left out given that $\hbar\omega_X >> IP$. The free electron interacts with the THz field and its energy starts changing. At a certain time t the electron's energy is given as

$$W_T(t) = \frac{\mathbf{v}_T^2(t)}{2}, \tag{2.56}$$

where $\mathbf{v}_T$ is the electron's momentum in the THz field and is equal to the vector sum of the electron momentum without THz field and the vector potential of the THz field $\mathbf{v}_T = \mathbf{v} + \mathbf{A}_{THz}(t)$. Inserting this in Eq. 2.56 one gets

$$W_T(t) = W_0 + (\mathbf{v}\mathbf{A}_{THz}(t) + \frac{\mathbf{A}_{THz}^2(t)}{2}). \tag{2.57}$$

The term in the bracket is the result of the interaction with the field whereas W_0 is the electron's energy before interacting with the THz field. This modified energy expression needs to be inserted in Eq. 2.55 in order to calculate the transition amplitude due to interaction with the THz field. Once both the X-ray and THz pulse have passed the transition amplitude $a_{\mathbf{v}}(\tau)$for a delay τ between the pulses (obtained by solving the Schrödinger equation) is given as

$$a_{v_T}(\tau) = -i \int_{-\infty}^{+\infty} \mathrm{d}t \exp[i\phi(t)] \mathbf{d}_{\mathbf{v}_T(t)} . \mathrm{E_X}(t-\tau) \exp[i(W + IP)t]. \tag{2.58}$$

The term $\phi(t)$ is the phase accumulated by the electron wave packet during the interaction with the THz field and reads

$$\phi(t) = -\int_t^{+\infty} (\mathbf{v}\mathbf{A}_{THz}(t') + \frac{\mathbf{A}_{THz}^2(t')}{2}) dt', \tag{2.59}$$

where the integration runs from the time of ionization t when the electron starts interacting with the THz field. Eq. 2.58 and Eq. 2.59 give the temporal phase modulation induced by the THz field on the electron packet generated by the X-ray field.

For a linearly polarized THz field $\mathbf{A}_{THz}(t) = -(\mathbf{E}_{THz}(t)/\omega_{THz})\sin(\omega_{THz}t)$ with a slowly varying envelope, that is $\mathbf{E}_{THz} \approx$ constant, the term $\phi(t)$ can be written as

$$\phi(t) = -\int_t^{+\infty} (\frac{\mathbf{E}_{THz}^2(t')}{2\omega_{THz}^2}\sin^2(\omega_{THz}t') - \frac{\mathbf{v}\mathbf{E}_{THz}(t')}{\omega_{THz}}\sin(\omega_{THz}t')\cos\theta)dt' \tag{2.60}$$

$$\approx \phi_1(t) + \phi_2(t) + \phi_3(t) \tag{2.61}$$

where θ is the observation angle, the angle between the electron's final velocity vector and the polarization of the THz field. The three components of the phase are

$$\begin{aligned}
\phi_1(t) =& -\int_t^{+\infty} U_p(t')\mathrm{d}t', \\
\phi_2(t) =& \frac{\sqrt{8WU_p(t)}}{\omega_{THz}}\cos\theta\cos(\omega_{THz}t), \\
\phi_3(t) =& \frac{U_p(t)}{2\omega_{THz}}\sin(2\omega_{THz}t).
\end{aligned} \tag{2.62}$$

Here $U_p(t) = E_{THz}^2(t)/4\omega_{THz}^2$ is the ponderemotive potential of the field, the potential changes slowly in time as the envelope of the THz field evolves. The other two terms $\phi_2(t)$ and $\phi_3(t)$ vary very fast due to the dependence on the frequency of the THz field and its second harmonic respectively. For the majority of the experiments $W >> U_p$, therefore the main contribution to the phase $\phi(t)$ is $\phi_2(t)$ which depends on the observation angle and the phase of the THz field $\omega_{THz}t$. This $\phi_2(t)$ defines the temporal evolution of phase associated with the electron wave packet which is embedded in a continuum with momentum v_T.

Let us consider that the ionizing X-ray pulse is a Gaussian with a linear chirp c_l. Then it can be defined as

$$\mathbf{E}_x(t) = \mathbf{E}_{0x}\exp[-a(t-t_0)^2]\exp[i(\omega_x(t-t_0) + c_l(t-t_0)^2)], \tag{2.63}$$

where $\mathbf{E}_{0x}$ is the amplitude of the X-ray field, the parameter a is $= 1/\sqrt{2\tau_x^2}$ where τ_x is the rms pulse duration of the X-ray pulse. The spectral intensity $I_x = |E_x(\omega)|^2$ can be obtained by a Fourier transformation of the above expression, giving the following dependence

$$I_x(\omega) = \exp[-\frac{a(\omega-\omega_x)^2}{2(a^2+c_l^2)}], \tag{2.64}$$

indicating that the spectral width of the X-ray pulse is $\sigma_x = \sqrt{\frac{a^2+c_l^2}{a}}$

In order to compute the photoelectron spectrum we need to take the square of the transition amplitude from the bound state to the continumm state with momentum v_T in the presence of the THz field that is $S(\omega) = |a_{\mathbf{v}_T}|^2$. Inserting the phase from Eq. 2.62 and X-ray field from Eq. 2.63 into Eq. 2.58 the spectrum is given as

$$\begin{aligned}
S(\omega) = |-i\int_{-\infty}^{+\infty} \mathrm{d}t\exp[i\phi(t)]\mathbf{d}_{\mathbf{v}_T(t)}\mathbf{E}_{0x}\exp[-a(t-t_0)^2] \\
\exp[i(\omega_x(t-t_0) + c_l(t-t_0)^2)]\exp[i(W+I_P)t|^2
\end{aligned} \tag{2.65}$$

This integral can be solved with some assumptions. The probability of ionization is taken to be unity: $\mathbf{v}_T(t) = 1$. As $W >> U_p$, $\phi(t)$ can be replaced by $\phi_2(t)$. The final assumption is that the pulse duration of the X-ray pulse is much shorter than the period of the THz field. Thus $\phi_2(t)$ can be written as

$$\phi_2(t) \approx \frac{\sqrt{8WU_p(t)}}{\omega_{THz}} \cos\theta (1 - \frac{\omega_{THz}^2 t^2}{2}). \tag{2.66}$$

Numerically solving the integral in Eq. 2.65 for electrons parallel to the THz field's polarization gives the following dependence:

$$S(\omega) = \exp[-\frac{a(\omega - \omega_0)^2}{2(a^2 + (c_l \pm s/2)^2)}]. \tag{2.67}$$

Here $s = \partial\, \delta W/\partial t$ is the streaking speed, the rate of change of electron's energy due to streaking, this is the spectrum for maximum streaking that is for the zero transition of vector potential. Eq. 2.67 tells that the rms width of the spectral envelope of streaked electrons is

$$\sigma_{st} = \sqrt{\frac{a^2 + (c_l \pm s/2)^2}{a}}. \tag{2.68}$$

The sign $\pm$ corresponds to the electrons propagation in the direction of the THz field and opposite to it. Inserting the value of a in terms of the temporal duration of the X-ray pulse τ_x and its spectral width σ_x, σ_{st} can be rewritten as

$$\sigma_{st}^2 = \sigma_x^2 + \tau_x^2 (s^2 \pm 4cs). \tag{2.69}$$

This result shows that the spectral width of the electron spectrum changes in the presence of the THz field because of the duration of the ionizing pulse and a linear chirp associated with it. Also this result relates the width of the photoelectron spectrum to the temporal pulse duration of the X-ray pulse. If it is assumed that in the absence of the THz field the spectrum of the photoelectrons mimics the spectrum of the X-ray pulse $\sigma_0 = \sigma_x$, the rms length of the X-ray pulse can be expressed as

$$\tau_x = \sqrt{\frac{\sigma_{st}^2 - \sigma_0^2}{s^2 \pm 4cs}}. \tag{2.70}$$

This final expression can be used for the temporal diagnostics of short X-ray pulses.

2.6.2 Semi classical model

When an electron is ionized in the presence of an external field it interacts with the fields in terms of momentum exchange. The following formulism is based on the concepts given in [1], [102], [11]. The frequency of the ionizing field is much higher than the frequency of the streaking field. This fact allows a separate analysis of ionization and streaking processes. The semiclassical model of the streaking process divides it into two steps. In the first step a highly energetic X-ray photon pulls out an electron. The initial energy of this electron is given as

$$W_0 = \frac{v_0^2}{2} = \omega_X - IP, \tag{2.71}$$

where v_0 is the initial velocity of the electron and ω_X is the energy of the X-ray field in atomic units. Before considering the next step in the process two assumptions are made. The first assumption is that $IP >> \omega_{THz}$, that is the THz field is not strong enough to affect the bound state of the electrons inside the atom. The second assumption is $\omega_x >> IP$ that is the ionic field does not affect the ejected electron any more. With these conditions the velocity of an electron, emitted in the direction of the THz field, can be written as

$$v(t) = -A_{THz}(t) + (v_0 + A_{THz}(t = t_i)). \tag{2.72}$$

Here v_0 is the initial velocity at the time of ionization $t = t_i$, whereas $A_{THz}(t)$ is the vector potential of THz field. In Eq. 2.72 the first term on the right hand side corresponds to a quiver oscillation that is averaged to zero once the THz pulse ends : $A_{THz}(t) = 0$. This leads to the conclusion that the final velocity of the electron stays constant after the THz pulse has passed and it depends on the THz field at the very moment of ionization t_i

$$v_f = v_0 + A_{THz}(t_i). \tag{2.73}$$

This change in velocity indicates the energy exchange between the electron and the THz field. Depending on the time of the ionization the electons interact with the THz field at different phases, leading to different kinetic energies. This fact allows the calculation of the X-ray pulse arrival time with respect to the THz pulse by measuring the central energy of the photoelectron spectrum. Assuming a linearly polarized THz field with electric field vector

$$\mathbf{E}_{THz}(t) = \mathbf{E}_{0THz}(t)\cos(\omega_{THz}t + \varphi), \tag{2.74}$$

and vector potential given as

$$\mathbf{A}_{THz}(t_i) = \int_{t_i}^{\infty} \mathbf{E}_{THz}(t)dt. \tag{2.75}$$

For a THz field with slowly varying envelope the vector potential at the time of ionization can be expressed as

$$\mathbf{A}_{THz}(t_i) = -\frac{\mathbf{E}_{0THz}}{\omega_{THz}}\sin(\omega_{THz}t_i + \varphi). \tag{2.76}$$

The argument of the sine function can be rewritten as $\omega_{THz}t_i + \varphi = \phi_i$ where ϕ_i is the phase of the THz field at the time of ionization. Taking this into consideration and using Eq. 2.73 for the final kinetic energy of an electron after streaking $W_{kin} = v_f^2/2$ one gets the result

$$W_{kin} = W_0 + 2U_p\cos2\theta\sin^2\phi_i \pm (1 - (2U_p/W_0)\sin^2\theta\sin^2\phi_i)\sqrt{8W_0U_p}\cos\theta\sin\phi_i, \tag{2.77}$$

where W_0 is the initial kinetic energy of electron, θ is the angle between the final velocity of the electron with the polarization axis and U_p is the ponderemotive energy as given by Eq. 2.4. This result shows that the final kinetic energy of the electron after streaking depends on the phase of the THz field ϕ_i at the time of ionization. Moreover the streaking is an angle dependent effect, depending on the the orientation of electron's initial velocity vector with respect to the THz light polarization it will get a certain shift in energy plus a certain deflection from its original direction see Fig. 2.14.

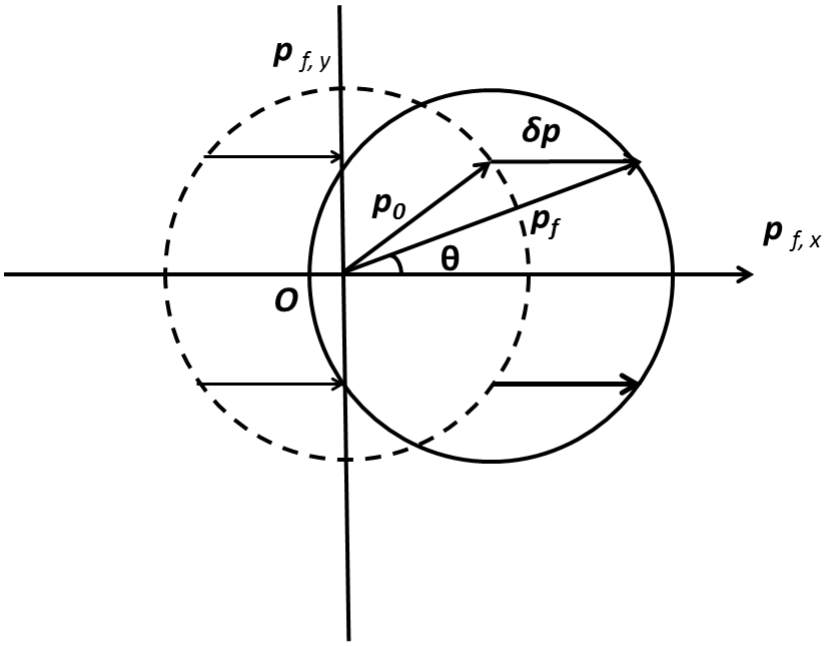

Figure 2.14: Streaking effect on photoelectrons generated at a given phase ϕ_i. The dashed circle is the initial momentum distribution in the xy plane and the solid circle represents the distribution after deflection by the streaking field. p_0 is the initial momentum vector, δp is the change of the momentum and p_f is the final momentum vector having an angle θ with respect to the polarization axis. Figure adapted from [102]

For the case of a final velocity along the polarization axis Eq. 2.77 reduces to

$$W_{kin,0} = W_0 + 2U_p sin^2\phi_i \pm \sqrt{8W_0U_p} sin\phi_i. \tag{2.78}$$

For most of the experiments $U_p << W_0$ is valid, thus Eq. 2.78 simplifies to

$$W_{kin,0} = W_0 \pm \sqrt{8W_0U_p} sin\phi_i. \tag{2.79}$$

The X-ray pulse with a certain temporal duration creates electrons at different points in time. Each electron has its own ionization time t_i and hence sees a different phase of the THz field ϕ_i. The final energy spectrum of the electrons contains information of temporal structure of X-ray pulse. To be more precise the final spectrum is a convolution of the energy with the streaking field and the temporal profile of the X-ray pulse. Now for deconvolving the rms width of the photoelectron spectrum has to be taken into account. With a linear energy chirp in the X-ray pulse, the rms spectral width of the streaked electron spectrum is

$$\sigma_{st}^2 = \sigma_0^2 + \tau_x^2(s^2 \pm 4cs). \tag{2.80}$$

The contribution from the linear chirp depends on the direction of the photoelectron velocity with respect to the streaking field: it can either broaden or narrow the spectral width.

To better understand this it is necessary to consider the streaking process once again with respect to the slope of the streaking field as shown in Fig. (2.15). The same initial

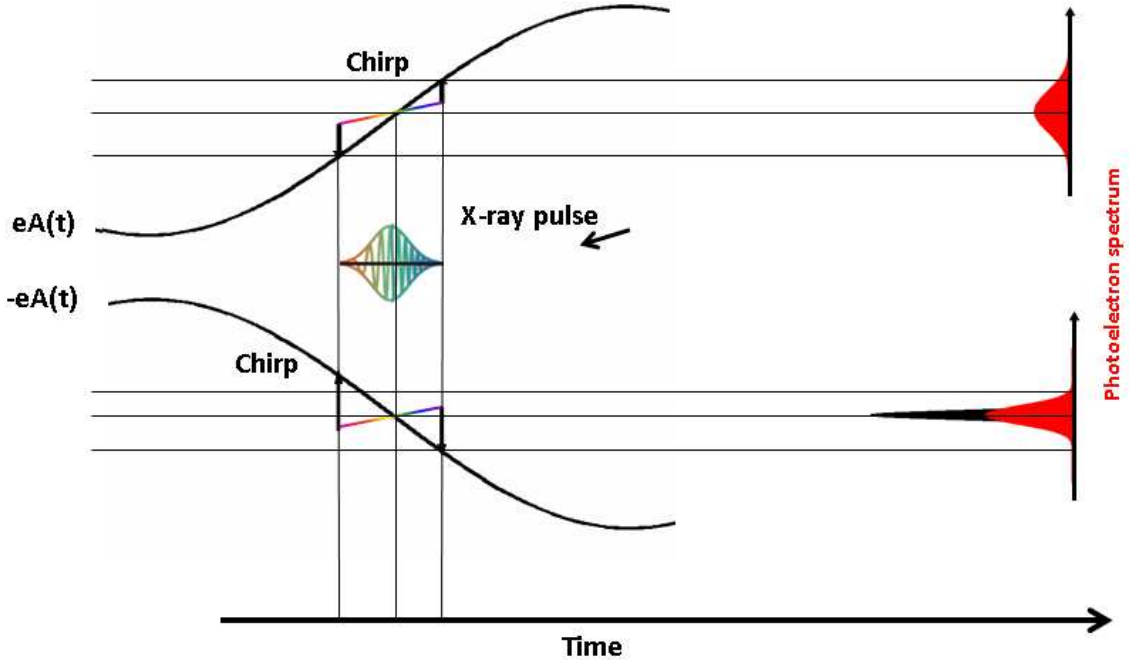

Figure 2.15: Depiction of the streaking process. The photo electron spectrum becomes broader due to streaking but the amount of broadening depends on the slope of the streaking field. Figure adapted from [83]

chirp is translated in opposite ways depending on the slope of the streaking field. The solution to the problem is to measure the electrons propagating parallel to and opposite to the streaking fields simultaneously, which is conveniently done in a VMI spectrometer with a 4π steradians acceptance angle. By carefully measuring the spectral width of the electron spectra for electrons propagating parallel or anti-parallel with respect to the THz field one can achieve $\Delta\sigma_{\pm}^2 = \sigma_{st}^2 - \sigma_0^2 = \tau_x^2(s^2 \pm 4cs)$, where $+(-)$ corresponds to measurement along (opposite to) the THz field. The pulse duration is then calculated as

$$\tau_x = \sqrt{\frac{\Delta\sigma_+^2 + \Delta\sigma_-^2}{2s^2}}. \tag{2.81}$$

When both X-ray and THz pulses are generated from same laser no jitter occurs between them and hence a more reliable measurement can be performed.

If the semiclassical and quantum models are compared to each other one finds that both models give equivalent expressions for the energy change for a streaked electron. The comparison also tells that the semiclassical model shows that the final kinetic energy of the electron is defined by the phase of the THz field at the time of ionization and quantum model shows that the phase accumulated by the electron wave packet during the process is temporally modulated by the THz field.

2.6.3 Unique advantage of using velocity map imaging

Velocity map imaging spectroscopy of electrons created by attosecond pulses and streaked by the femtosecond infra-red laser is in use for some time [17, 18, 105]. Now if we consider

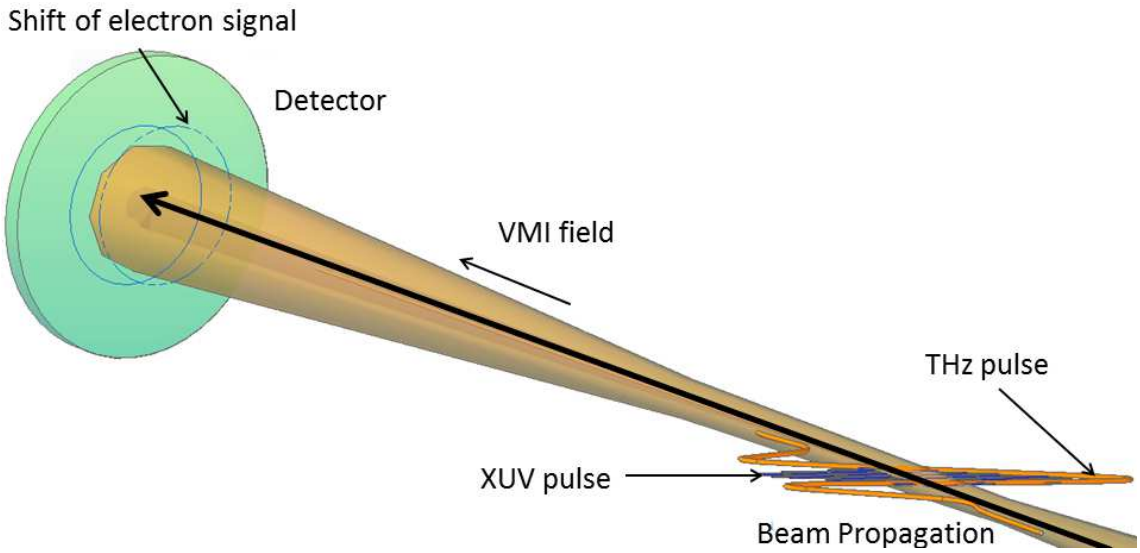

Figure 2.16: Illustration of the streaking effect. Electrons generated by an XUV pulse are streaked by a THz pulse and the effect can be directly observed on a position sensitive detector using VMI spectroscopy.

the image obtained on the VMI detector in momentum space with the x-axis being the polarization axis then the momentum of a streaked electron is given as

$$\mathbf{p} = (\mathbf{p}_x - \mathbf{A}(t)) + \mathbf{p}_y \tag{2.82}$$

Which indicates that the x component of momentum gets the shift as shown in Fig. 2.14. The dashed circle of radius p_0 is the electron momentum distribution in the xy plane produced by the X-ray pulse with no THz field present. The solid circle represents the drift momentum distribution in the presence of the THz field. By using the VMI spectroscopy both energy and angular shift as a result of streaking can be measured as a complete picture of the electron's momentum is measured.

Chapter 3

Experimental setups

In this chapter the setups of different segments of the work are described with a main focus on the working principle of major components. Sec. 3.1 is dedicated to the Ti-Sapphire laser system. Section 3.2 summarizes the radiation sources, including concise accounts of the setup of a source for higher order harmonic generation (HHG) with the hollow fiber compressor and the experimental part where THz- radiation is generated. Section 3.3 explains the electro-optical sampling setup. The streaking setup is described in section 3.4 with detailed description of the VMI spectrometer and the position sensitive detector used to detect the electrons.

3.1 Femtosecond pulsed laser system

The Ti-Sapphire laser invented by [106] has rapidly become commercially available. This is the working horse for most of the laboratories now-a-days. A Ti-Sapphire laser system from Amplitude Technologies with an oscillator from Femtolasers(Synergy) is used in this project. The different components of the system are represented in Fig. 3.1. The active medium in the oscillator is the Ti-Sapphire crystal and it is pumped by a frequency doubled diode laser at 532 nm (Verdi V-5, Coherent). The basic working principle of the laser system is chirped pulse amplification [107] depicted in Fig. 3.2. The oscillator provides pulses with a bandwidth of 90 nm with a pulse energy of 5 nJ at 75 MHz rate. These pulses are first stretched in time by using a grating. This grating stretches the pulses by a factor of 1000. The stretching is necessary in pursuance of keeping the intensity under the damage threshold of the amplifying medium. The stretched pulses then enter the regenerative amplifier where they propagate for several round-trips in a z-shaped cavity. 1000 pulses per second are amplified in a titanium sapphire crystal such that the repetition rate is reduced to 1 kHz from the initial 75 MHz produced in the oscillator. Each pulse is coupled out by a Pockels cell after it has reached its maximum energy. Every 40th pulse is then sent to a different amplification system and used for different experiments. The remaining 975 pulses are further amplified, therefore they propagate 5 times though another Ti-Sapphire crystal, this is called multi-pass amplification. Both amplification crystals are pumped by a diode laser in the green spectral range (DM30-527, Photonics Industries). Afterwards the pulses are re-compressed by a pair of gratings to obtain a pulse duration of 35-40 fs. Each pulse has an energy of about 2.5 - 3 mJ.

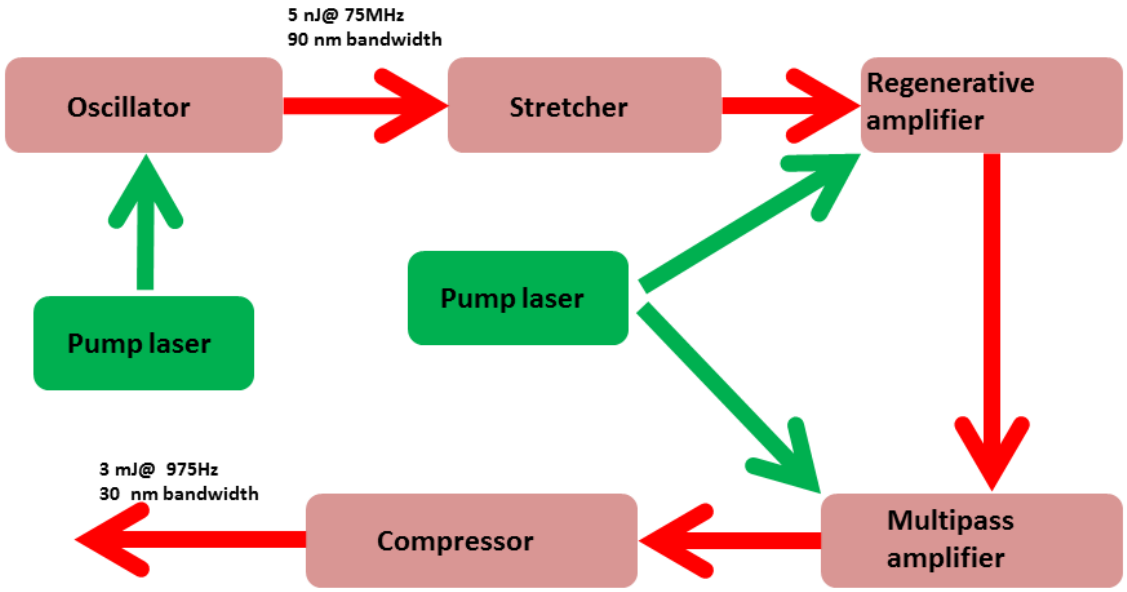

Figure 3.1: Different parts of laser system.

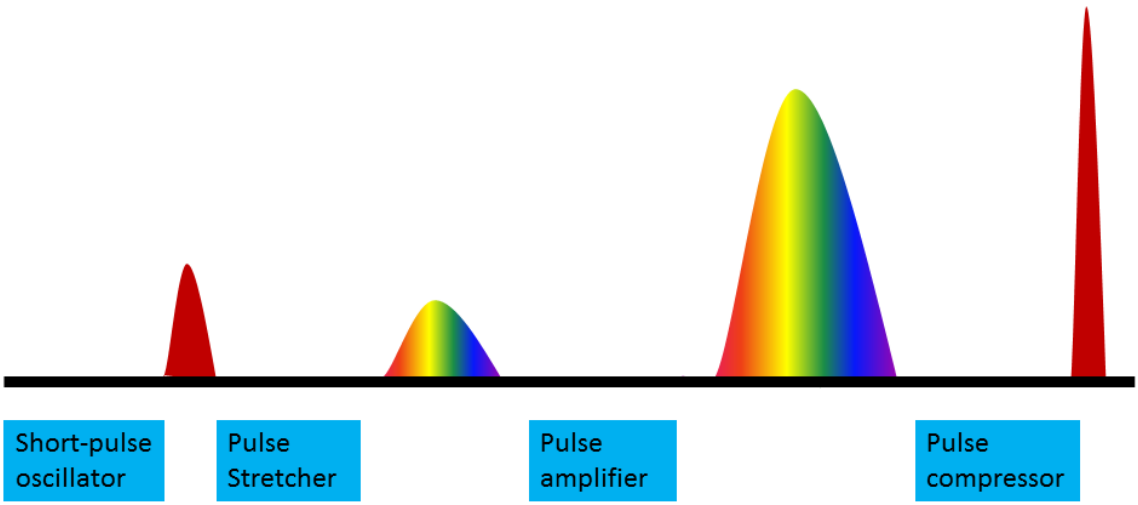

Figure 3.2: The principle of chirped pulse amplification.

3.2 Radiation sources

A 72/28 beam splitter is used to divide the pulse energy coming from the laser compressor for the HHG setup and THz-radiation generation setup. The major reflected part is used for higher harmonic generation and the minor transmitted part is used for generating THz-radiation. In the following the setups for generating both types of radiation are described.

3.2.1 HHG setup

This part of the beam is stabilized using an Aligna TEM stabilization unit, this is necessary for the sustainability of the source. For this purpose two mirrors in the beam path are equipped with two-axis piezo actuators each. Furthermore, the small transmission of another mirror is used for the precise determination of position and angle of the beam by means of PSD's (position-sensitive devices). The stabilization is controlled via special software and hardware.

The setup is sketched in Fig. 3.3. Starting from the top-right a combination of hollow core fiber and chirped mirrors is used to compress the pulses. For this purpose the beam is focused into a one meter long hollow core fiber filled with neon at a pressure in the range of 0.8-1.35 bar using a one inch spherical lens of focal length 3 m (not shown in the sketch). The length of the fiber and the focal length for focusing are determined on the basis of initial pulse energy and desired compression factor. The self phase modulation occurring inside the fiber (see section 2.2.3) introduces a negative chirp in the pulse along with broadening of the spectrum. A set of three chirped mirrors is used to compensate for this chirp (part a - c in Fig. 3.3.). Each chirped mirror introduces about -120 fs^2 group delay dispersion (GDD). For an accurate chirp compensation a little too much negative GDD is applied and to compensate this two fused silica glass wedges are used. The wedges are 30 x 20 mm in size and have thicknesses in the range of 0.2 to 1.25 mm and the wedge angle is 2°. To avoid losses due to reflection both sides are coated with one broadband transmission coating.

For the transportation of these pulses, with broad spectrum, further broadband silver mirrors from the company Layertec with a broadband reflection coating are used (part 1 - 3 in Fig. 3.3). After the chirp compensation the divergent beam is first collimated using a concave mirror with a focal length of 3 m. After collimation there is more folding of the beam until it reaches the focusing mirror with a focal length of 1.5 m. Between the focusing mirror and the target another motorized mirror is used at the smallest possible incidence angle to get possible beam path alteration in a ±10 mm range for manipulating the focus position relative to the target and achieve phase matching (the mirror labeled as 3 with a two sided arrow in Fig. 3.3). The focused beam interacts with the gas target consisting of a thin wall stainless steel tube, with inner diameter of 3 mm, closed from one end and filled with neon at a pressure around 100 mbar. The tube is fixed in the center of a separate chamber using a Swagelok holder. The focused laser has sufficient intensity to provide an entrance and an outlet hole in the tube. Thus, the smallest possible openings are formed. In order to monitor the focus position, the transmission of one silver mirror is focused with a lens of 750 mm focal length and is detected by a charge coupled device (CCD) camera to attain a copy of the focus (beam monitoring setup in Fig. 3.3.).

The generated harmonic beam propagates collinearly with the infrared beam through a mirror with a central hole of 2 mm diameter, this mirror serves as the first filter for infrared by reflecting back the divergent laser beam and letting the XUV beam though

the hole. In addition, aluminium or zirconium filters are used to filter out the rest of the infrared beam.

The spectral characterization of the harmonics is done using a spectrometer. A blaze grating with 600 lines per mm at a blaze angle of 2°is used for this purpose. The beam propagates through a vertical slit in front of the grating so that a spatial splitting of the harmonics up to about 77th order at a distance of about 300 mm from the grating can be done. The detector consists of a multi-channel plate(MCP) and a phosphor screen with 25 mm active area. The screen is imaged over a mirror with a lens on a CCD camera(characterization segment in Fig. 3.3.). The grating and the slit are taken out of the beam path during the experiment.

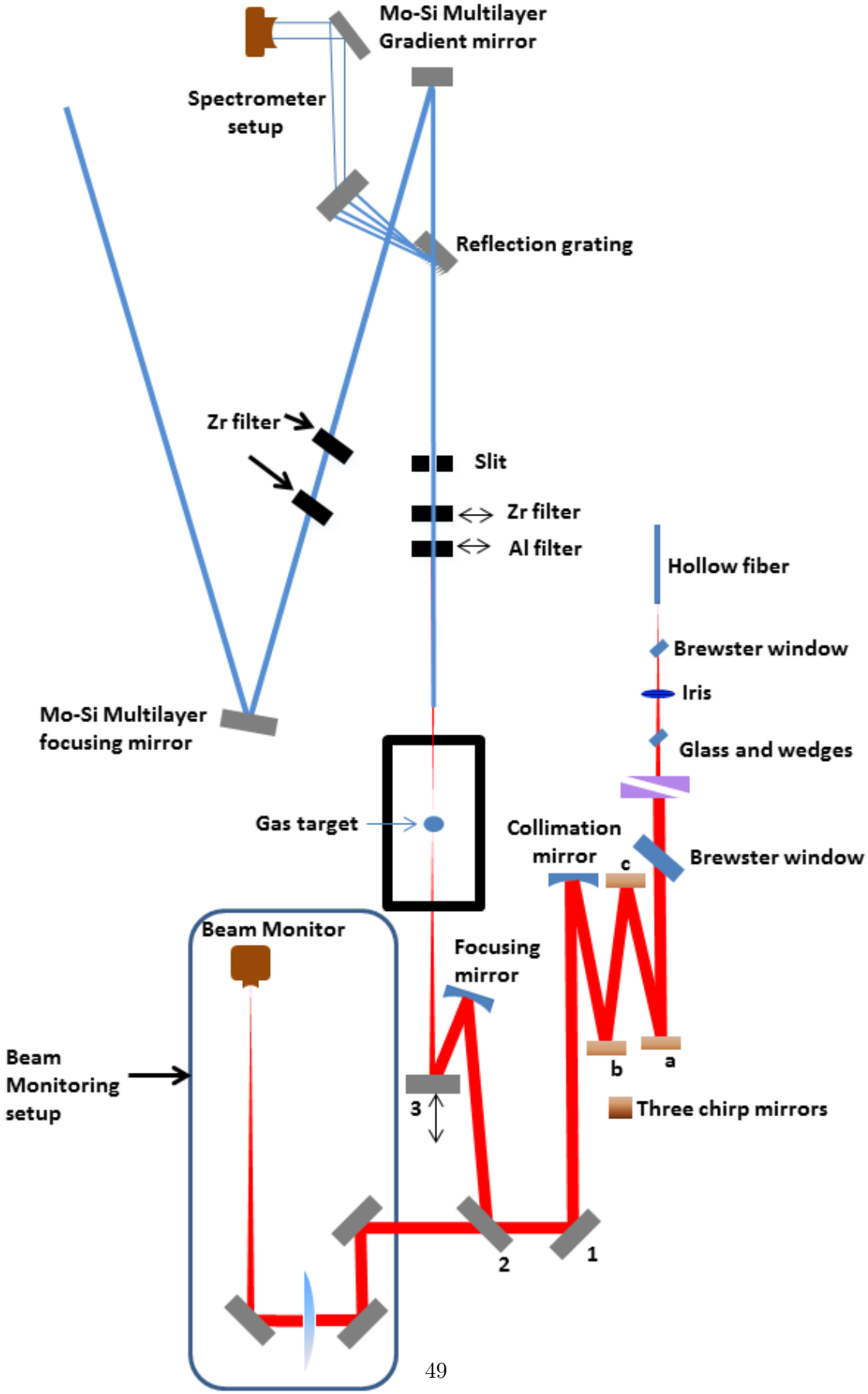

Figure 3.3: Higher Harmonic generation setup. Figure adapted from [108]

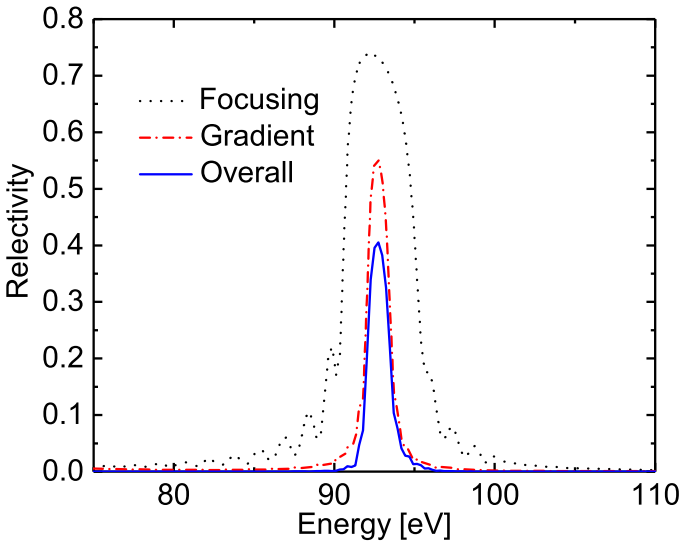

Figure 3.4: Individual and overall reflectivities of gradient and focusing multilayer mirrors.

The XUV beam, before it travels to the experiment, is incident on a gradient mirror at an angle of 5°which is used to select one single harmonic order. A gradient mirror is coated with a differential coating of Molybdenum and Silicon with smooth gradient, reflecting different harmonic orders depending on the position where the beam hits the mirror. In order to use this feature of the mirror the vertical motion of the mirror is motorized. By changing the mirror height relative to the incident beam the spectral range can be set between 85.5 and 98 eV. After this the beam is imaged into the target using another Mo/Si focusing mirror with a focal length of 750 mm. One important aspect to be mentioned is that the incidence and outgoing angle for the focusing mirror is 20°due to the experimental setup requirements, which gives an astigmatic focusing. The reflectivity curves of gradient and focusing mirror as well as the overall reflectivity are plotted in Fig. 3.4. It is evident from the plot that the gradient mirror narrows down the reflected bandwidth making selection of single harmonic possible.

The absorption length of the here produced harmonics is in millimeter range at atmospheric conditions. Therefore the setup from generation to interaction with the target(also the characterization setup) is kept under vacuum.

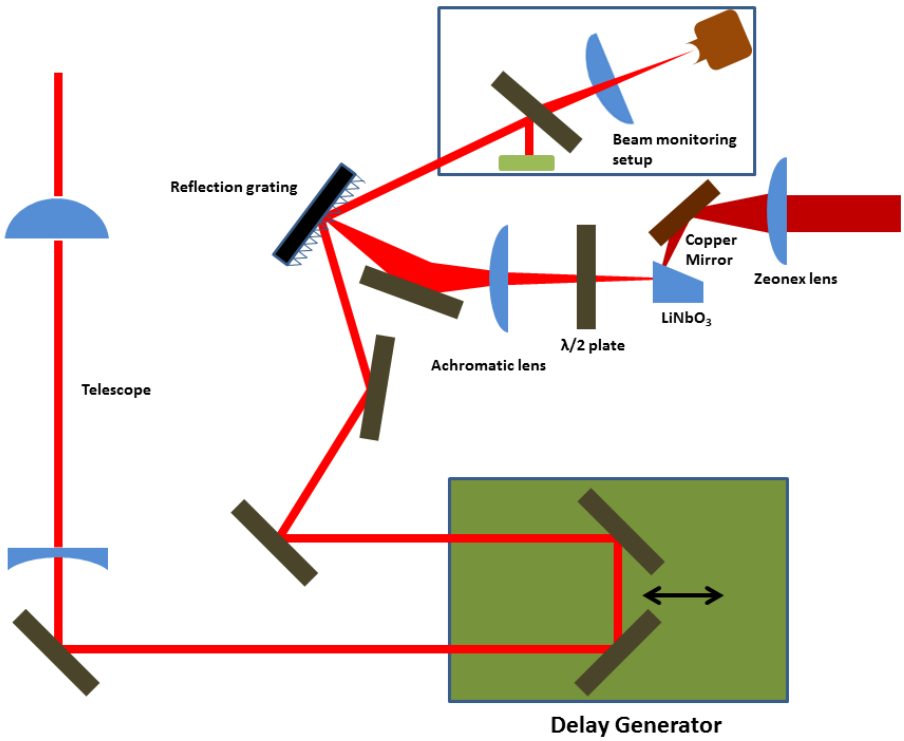

Figure 3.5: THz-radiation generation setup

3.2.2 THz-radiation source

The transmitted portion from the beam splitter is used for THz-radiation generation. In order to achieve a beam path length close to that of XUV beam, the infra-red beam passes through a delay line of about 12 m. For this purpose, the beam is folded several times with a small incidence angle at a distance of about two meters back and forth using zero degree 2" mirrors. The beam transport up to the source contains a total of 16 mirrors including 45° and 0° incidence angle mirrors. To prevent the beam from disturbance due to air major part of the delay line is covered in metal boxes.

The setup is schematically depicted in Fig. 3.5. Before setting up the source the incoming beam size is measured precisely using the knife edge scan technique and found to be $w_x = 9.5$ mm and $w_y = 12$ mm at the position of the source. At first, a Galilean telescope with a plane convex lens of focal length 1 m and plane concave lens of 0.2 m is implemented to get a demagnification factor of 5 followed by the delay unit. This unit is used to alter the beam path for THz pulses with respect to the IR/XUV beam for the electro-optical sampling/streaking experiment. The unit consists of a long delay stage with a delay range of ±150 ps with two 1" mirrors aligned at right angles to each other fixed on the stage plate. The next optic in the beam path is the crucial blazed grating with 2000 lines per mm. The alignment of the grating deviates from Littrow configuration by 9.5°to get best possible pulse front tilt for phase matching inside the $LiNbO_3$ crystal. The 0^{th} order of the grating is used for alignment purposes. It is deflected towards a 2" 45° mirror, the reflection of the mirror is directed to a white screen to monitor the beam position. The leakage of the mirror is focused by a 75 mm lens on a CCD camera to observe angular deviations (beam monitoring part in Fig. 3.5.)

The first order is imaged by an achromatic lens of focal length 75 mm onto the crystal with a further demagnification of factor 2, the beam size at the crystal then is w_x = 1 mm and w_y = 1.3 mm, full width at half maximum in horizontal and vertical directions respectively. A $\lambda/2$ plate is inserted in the beam path before the crystal to rotate the polarization of the pump beam to s-polarization.

The pulse energy, after all losses, reaching the crystal is 0.55 mJ. Taking the pulse duration of 40 fs this gives an intensity of 0.65 TW/cm^2 which is slightly below the damage threshold given as 0.7 TW/cm^2. The angle between the input and output surface of the crystal is 63°so that the THz-radiation is perpendicular to the crystal surface.

For the purpose of the optimization of the source it is necessary to introduce a significant number of degrees of freedom. The grating and crystal can be finely rotatable and movable in horizontal direction (using rotation and linear stages) in order to fix the pulse front tilt. The crystal position can also be changed along the beam path using another linear stage to vary the spot size on the crystal as well as the pulse front tilt. In order to alter the distance between telescope lenses the plane concave lens is placed on a linear stage. The achromatic lens can be moved along the beam path to change the imaging likewise the pulse front tilt.

The THz-radiation is transported using copper mirrors with a diameter of 5 cm . As the THz-radiation is highly divergent, a collimation optics is needed to be installed shortly after generating crystal. For this purpose two different lenses are tested at a distance less than 10 cm from the crystal, one made of Teflon and the other made of Zeonex with approximately same focal length. A periscope is used to bring the beam to experimental chamber height and switching the polarization from perpendicular to parallel to match with the polarization of XUV beam. For focusing the beam into the target a combination of two lenses (made of Zeonex480R) with a focal length of 50 mm each is used that gives an effective focal length of 34 mm together. The test focusing is however done with a Zeonex480R lens of focal length 100 mm.

Measurement of THz beam parameters

Two different pyro-electric detectors are used to measure the pulse energy of the generated THz-radiation after blocking the infra-red using a 0.7 mm thick black polymer plate. The transmission of this filter is measured to be 90%. One of the detectors has a circular chip with a radius of 5 mm. In addition a 2 x 2 mm pyro-electric detector (LME 301, Infratec) is utilized. For both detectors the original signal is amplified by a charge sensitive preamplifier module (CR 110, Fast ComTec). In order to map the beam profile a combination of the pyro-electric detector with a module consisting of four motors and a picoscope controllable from a Labview program is used.

3.3 Electro optical sampling setup

The electro-optical sampling (EOS)is carried out in the experimental chamber as close to the interaction region as possible. This measurement not only insured the spatial and temporal overlap of THz and Infrared(IR) beam (which propagates co-linearly with the XUV beam) but also characterize the THz pulse in time and spectral domain. The arrangement used for this purpose is depicted in Fig. 3.6.

The infrared beam is used as a probe beam to detect the electo-optical effect generated

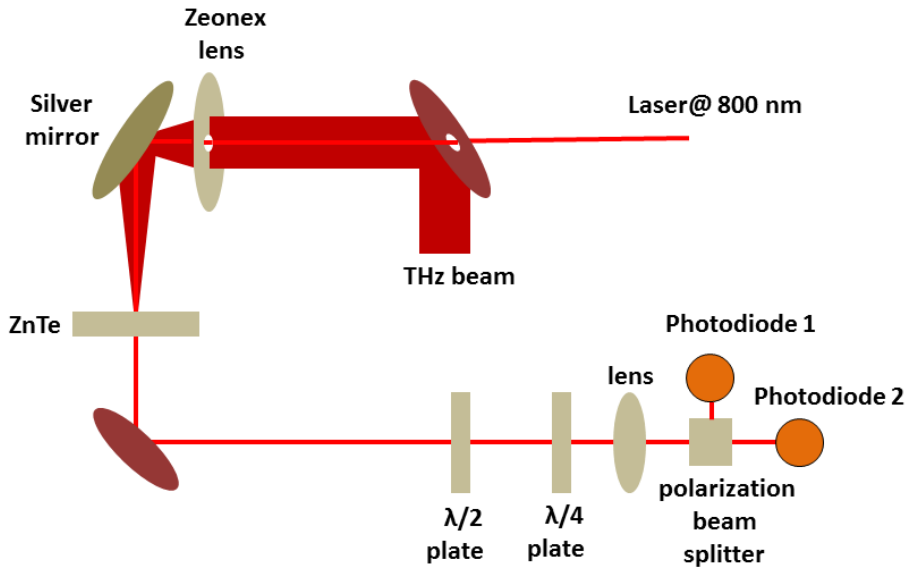

Figure 3.6: Setup for EOS. The THz and IR beams are focused into the ZnTe crystal. The polarization change induced by the THz beam is detected by polarizing beam splitter and two photodiodes.

by the THz beam(see section 2.3.5). The IR beam is the one coming on the XUV beam path, therefore it has the same timing as the XUV beam except the correction from air to vacuum as EOS is carried out under atmospheric conditions. Both THz and IR beam are deflected using a 2" silver mirror towards the EOS crystal, namely a ZnTe crystal with a thickness of 3 mm. After this the probe beam is transported to detection set-up. Here first a $\lambda/2$ plate and then a $\lambda/4$ plate is inserted to get a balanced detection or more precisely to get equal contributions for two orthogonal polarization components. Then follows a polarizing beam splitter to separate two polarizations and two photodiodes to measure the two signals. In order to detect the change caused by the THz field the difference signal of the two photodiodes is measured. As the probe beam is divergent and travels a long distance from the EOS crystal to the photo-diode a focusing lens is used before the polarizing beam splitter so that the beam parts can reliably placed on the photo-diodes.

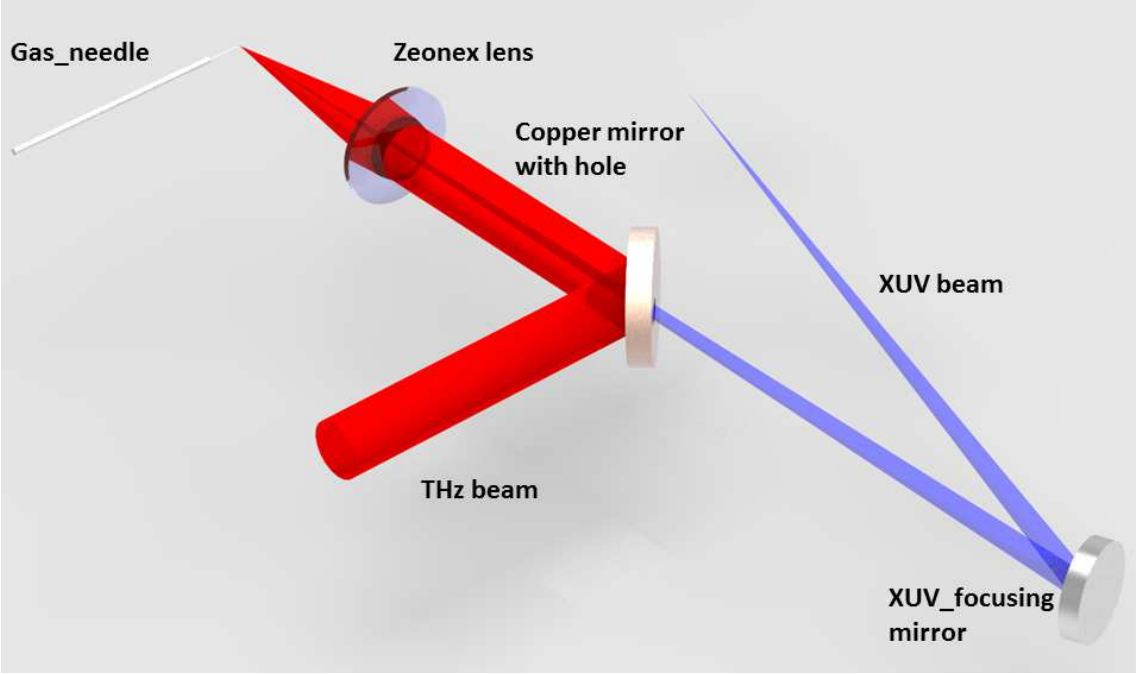

Figure 3.7: Setup for streaking. The THz and XUV beams are focused at the interaction point. The copper mirror and Zeonex lens are equiped with central holes for the in-coupling of the XUV beam. The target gas is supplied by a thin gas needle.

3.4 Streaking setup

For the purpose of electron streaking both XUV and THz beam are overlapped at the interaction point in the experiment, the setup is shown in Fig. 3.7.

The THz beam is reflected over a 2" copper mirror and is focused by a lens made of Zeonex-480R with a focal length of 100 mm.

For the in-coupling of the XUV beam a 3 mm central hole is drilled in the copper mirror at 45°. The lens is provided with a central hole of diameter 2 mm for the same purpose. The target gas is supplied via a thin needle.

The setup used for electron detection is described in the following section.

3.4.1 Velocity map imaging spectrometer with static voltage

The design used in this project is similar to the one proposed by Eppik and Parker [22] with only two modifications. One modification is the in-coupling of the excitation pulse and second is the target gas feeding. The beam propagation direction is along the detector normal, this arrangement is chosen to make the in-coupling of the invisible THz beam more convenient. The velocity map imaging detector consists of an assembly of three electrodes and a gas needle motorized in three dimensions shown in Fig. 2.9. The electrodes are made of aluminium with 5 mm thickness. The diameter of the repeller plate, the first electrode, is 155 mm with a central hole of diameter 22 mm. The extractor plate, the second electrode, has a diameter of 160 mm with a central hole diameter of 40 mm. The third electrode labelled as ground has a diameter of 200 mm with a central hole with a diameter of 40 mm. An exchangeable entrance port is added to the repeller plate with the

possibility to glue a thin plate with pinhole for beam in-coupling, the purpose is to test different sizes of the hole such that both beams can be brought to the interaction point without getting distortion of electric field. The distance between the repeller and extractor electrode is set to 18 mm and the distance between the extractor and ground electrode is set to 25 mm. The electrodes are connected together with rods made out of PEEK and the spacer are also made of PEEK, this is necessary to prevent the possibility of any electrical connection between the electrodes. The electrode surfaces are finely polished and examined using interferometric microscopy with a rms roughness values below 0.5 microns, this is essential to avoid any field emission due to sharp edges and have a homogeneous electric field. The distance between the interaction plane and the detector is as large as 28.5 cm This large distance is desired to optimize the resolution of the electron signal on the detector.

The gas nozzle is chosen such that it causes no distortion to the electric field between the repeller and the extractor. For this purpose a thin aluminium capillary with an inner diameter of 0.2 mm and an outer diameter of 0.3 mm is inserted inside a 1/16" aluminium capillary with an inner diameter of 0.5 mm and a length of 100 mm. It is first glued with adhesive conductive silver glue and afterwards is cut by a focused laser to the length of 15 mm to prevent any cloacking of the thin nozzle. The mounting of the capillary on the motorized stage assembly is done by pieces made of PEEK. The motorization of motion of the gas nozzle is necessary because the its position highly affects the circularity as well as the resolution of the acquired electron rings on the detector. In order to maintain a homogeneous field distribution an appropriate voltage is applied to the gas needle.

For the detection of electrons with energies as high as 80 eV at a high detection efficiency voltages as high as -10 kV and -8 kV are applied to repeller and extractor plates, respectively. High voltages are necessary as the detection efficiency depends on the kinetic energies electrons acquire from the DC field(see Sec. 5.4). Special care needs to be taken to work with such high voltages. The commercial voltage supplies (from iseg Spezialelektronik GmbH) are used with the desired voltage range. The advantage of using this supply is the possibility to read the applied voltage on the display with a step of 1 Volt. In order to prevent any short cut additional 1 mm thick silicon insulation is used for the Kapton insulated cables used for connecting the voltage feed-throughs to the electrodes.

3.4.2 Position sensitive detector

A higher energy resolution is a prerequisite for a meaningful study of photoproducts, for this reason the position sensitve detector (PSD) must have a very high spatial resolution.

In order to achieve a good count rate and be able to do long scans in a reasonable time a high detection efficiency is essential. Usually micro-channel plates (MCP) are used. However the MCP's with increasing sizes are extremely fragile and expensive and the quantum efficiency depending on the material used and acceleration voltage applied is as low as 50%.

A detector with a rather special design manufactured by Proxitronics is used in this project that can serve the required purposes it is schematically drawn in Fig. 3.8.

The first part of the detector is a phosphorous screen with a diameter of 150 mm and it will be called primary phosphor screen hereafter. The primary phosphor screen is coated with P43 (PrCeF) with a decay time between 1 to 10 μs. On the front of the primary phosphor screen a 5 - 50 nm thick aluminium coating is evaporated this coating shields the background light. In addition an absorption layer is deposited over the aluminum coating

which collects the wide band light while blocking the unwanted reflections. The electrons lose 3 keV energy while transmitting through these layers [109]. The spectral sensitivity of the first phosphor screen is calculated from the table given in the user manual of the detector [109] and it is 0.72 W/mA. In order to convert the spectral sensitivity S to photons/electron one needs to consider number of photons per unit time, with wavelength equal to emission wavelength of the phosphorous screen, generating a power of "S" W and the number of electrons per unit time creating a current of 1 mA, this leads to the following conversion

$$n_{ph} = \frac{S \mathrm{x} \lambda_{emission}}{6.24 \mathrm{x} 10^{15} \mathrm{x\,h\,x\,c}}, \tag{3.1}$$

where $\lambda_{emission}$ is the emission wavelength of the phosphorous screen, h and c are the Planck's constant and the speed of light respectively.

This screen is coupled via a fiber optic taper to a photocathode. This is the bell shaped part in Fig. 3.8. The fiber taper is made of a hexagonally packed glass fiber bundle and reduces the diameter from 150 mm to 40 mm and guides the photons generated due to the electron impact on the primary phosphor screen. The use of a taper has advantages over the use of a lens for imaging the phosphor screen. The fiber taper transports the light more efficiently than with an optical lens imaging. The aluminium coating on the primary phosphor screen reflects the light that is generated in the phosphor layer into the taper, this increases the brightness for electron events with more than 4 keV by up to 100%. The efficiency of the fiber taper for 1:1 coupling is 70% (the number is taken from the documentation provided at the time of purchase) and due to reduction of diameter from 150 mm to 40 mm it becomes 5%.

The next component in the detection system is a photocathode made of Quartz (Type S20). The photons hitting the photocathode generate electrons due to the photoelectric effect. The spectral sensitivity of the cathode for the wavelength of 545 nm is given as 45 mA/W [109]. The following formula relates the spectral sensitivity of the photocathode $S$to its quantum efficiency [109],

$$Q(\%) = \frac{124 * S(mA/W)}{\lambda(nm)}, \tag{3.2}$$

hence for the used photocathode the quantum efficiency is 10.2% at this wavelength. The photocathode can be used with the supplied pulse generator to be activated for a certain time. The potential of the photocathode U_{ph} is 12V (off) and -180V (on) [109]. The gate time can be either provided by the trigger or by eight firmly pre-programmed pulse lengths. The delay between trigger input and switching of the cathode is 130 ns, the maximum pulse repetition frequency is 14 kHz. The jitter supplied by the manufacturer is max. 1 ns, the rising time (10% to 90%) is 15 ns.

The photocathode is followed by two Chevron-shaped MCP's of type BV4063 QZ-V. The potential of the first multi-channel plate is 0 V, for the second plate the static voltage can be applied from the pulse voltage supply generator (Type IG 100N) in ten steps between 1000V and 1800V. The electrons generated by the photocathode are amplified by the MCP's. The amplification factor of this arrangement is 1000 per MCP at a voltage of 1800 V. The efficiency of this stack is 60% [110].

The last part is another phosphor screen labelled as secondary phosphor screen herafter. The phosphor screen is also provided with a conductive layer on the side facing the MCP. The potential of this layer is 6 kV. The detection efficiency of this secondary phosphor

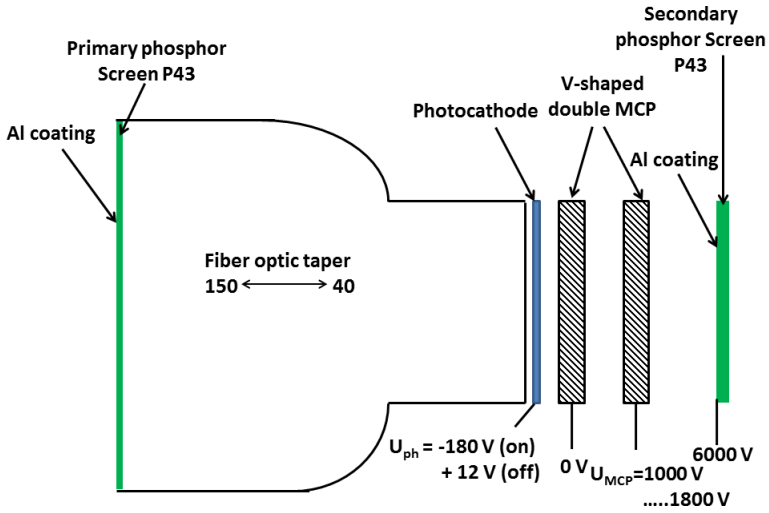

Figure 3.8: Schematic representation of different components of position sensitive detector. The voltages applied during operation are also given

screen is given as 0.6 W/mA for an applied voltage of 6 kV [109]; The combination of photocathode, MCP's and secondary phosphor screen is called the image intensifier. The amplified electrons ultimately produce the visible image on the secondary phosphor screen. The final resolution limit of the whole system is 24 line pairs per mm [111].

Two different cameras are tested to record the events occurring on the detector a Q cam (1392 x 1040 pixels) from Qimaging and a digital Basler camera (type acA1920-40 μm with 1920 x 1200 pixels).

For a high detection efficiency, for each electron that hits the primary Phosphor layer, a luminous spot should appear on the secondary phosphor layer. The product of the individual detection probabilities of the components involved must be as close to unity as possible.

Chapter 4

Characterization of radiation sources

In this chapter the specific properties of the radiation sources developed in this project are summarized.

4.1 Soft X-ray radiation generation and characterization

This section summarizes the performance of the hollow fiber compressor HFC and the HHG source. As the compressed pulses from the HFC are used to drive the HHG source, the performance critically depends on the successful operation of the HFC.

4.1.1 Operation of the hollow fiber for pulse compression

Several parameters affect the pulse compression achieved by a hollow fiber compressor. Starting from the optimization of the pulse compression inside the laser system to achieve the shortest possible chirp-free pulses, the average pulse duration used for this work is around 40 fs. This is critical for the self phase modulation (SPM) occurring inside the hollow fiber which requires a minimum critical intensity. The peak intensity is above 10^{14}W/cm^2 (the value is taken from the Ph D thesis of Roman Branaath [108]) to make SPM possible .

Another parameter is the gas pressure in the hollow fiber. Depending on the average output power of the laser, different pressures are needed in the fiber to attain the optimum broadening. During this work the gas pressure applied is in the range of 800 - 1350 mbar depending on the laser output, a higher average power from the laser demands a lower neon pressure in the fiber. Both fiber pressure and the beam in-coupling into the fiber affect the output mode of the fiber. For an efficient HHG process it is necessary that maximum power is contained in the central part of the fundamental EM11 mode.

For the current setup the maximum average power coupled into the hollow fiber is 2.2 W with the output power in the central mode equal to 0.9 to 1 W, giving a 50% useful transmission. The loss can be partly explained by the light scattered by the fiber cladding. The spectra for input and output beams are shown in Fig. 4.1.

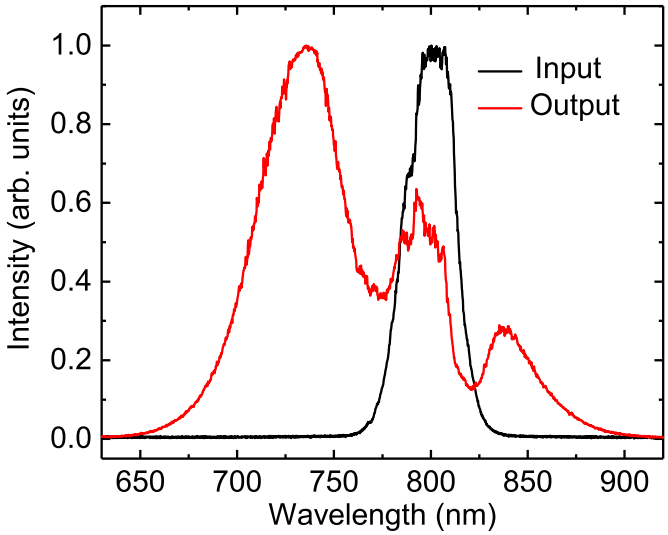

Figure 4.1: The input and output spectra for the Hollow fiber compressor. The broadening is evident.

The original spectrum is broadened. The FWHM for the shown input is 28.6± 0.1 nm. The central wavelengths are 800 nm and 745 nm for the original and the broadened spectrum, respectively. The positive chirp introduced by the fiber is compensated by the negative chirp of chirped mirrors. The calibration of the resulting pulse duration for a certain output spectrum is done in the master work of Brannath [47] by measuring the pulse duration using SPIDER (Spectral Phase Interferometry for Direct Electric field Reconstruction) for different width of the HFC output spectrum. If that is considered still valid pulses of duration down to 10 fs can be reached for the spectrum given in Fig. 4.1 leading to the conclusion that a compression factor of 4 (from 40 fs to 10 fs) can be attained with this setup.

4.1.2 XUV source optimization

The output of the HHG source is monitored using the spectrometer setup. A spectrum taken without any filter is shown in Fig. 4.2. The labelling of the harmonic orders is done with reference to the HHG spectrum measured after transmission through an aluminium filter. The aluminium filter allows energies below 73 eV to be transmitted as shown in Fig. 4.2. The focusing mirror directing the XUV beam to the experiment has maximum reflectivity for the 57th harmonic as shown in Fig. 3.4, thus the harmonic order of interest is the 57th. In the shown spectrum the cut-off occurs at the 67th harmonic order. It is important that the required harmonic order is within the plateau region in order to have sufficient flux for the experiment.

The first parameter to be optimized is the laser intensity at the target. The intensity affects the flux of higher harmonics as well as the the position of the cut-off. The factors affecting the intensity that can be manipulated are the chirp and the focus size. The chirp introduced by the HFC is minimized by matching the amount of glass (giving positive

chirp) with the chirped mirrors(giving negative chirp)(see Fig. 3.3). The focus size for maximum output is achieved by changing the size of the aperture (aperture in Fig. 3.3).

The second parameter critical for HHG source performance is the phase matching which is affected by the pump intensity as well as the target density. As the interaction length is fixed to 3 mm the gas density is mainly varied by changing the target gas pressure. In this work the target gas is neon and the applied target pressure ranges between 85 - 120 mbar. This gas pressure also affects the re-absorption of the generated harmonics, hence the gas pressure is optimized for the maximum output.

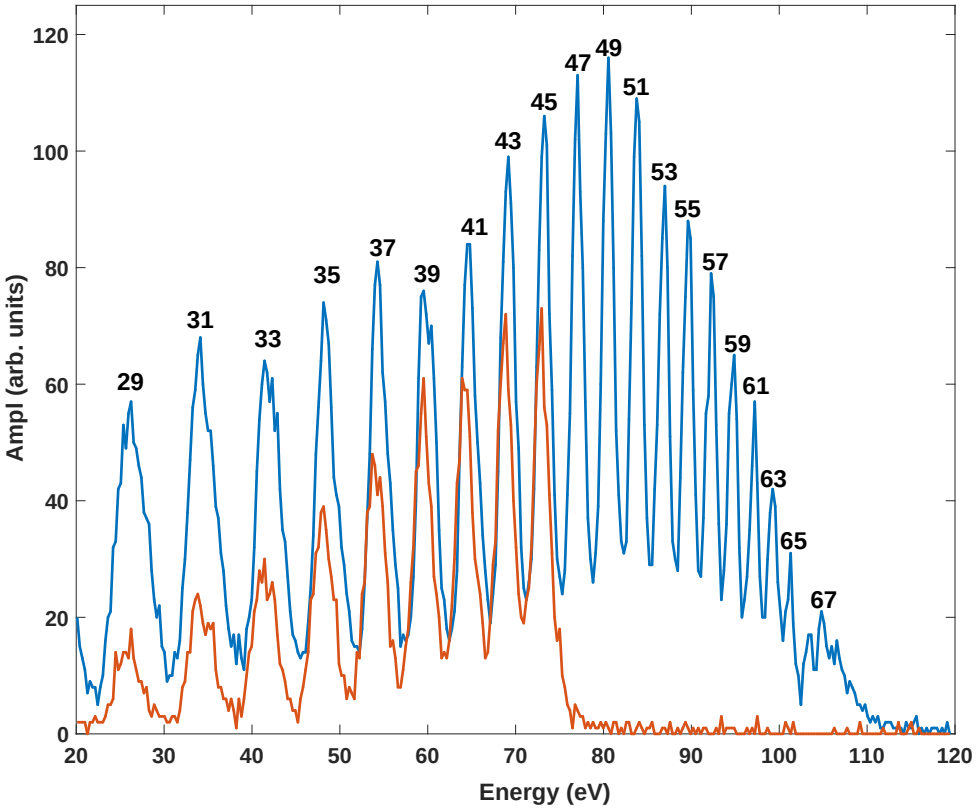

Figure 4.2: A spectrum of experimentally generated higher harmonics with no filter in blue and with Aluminium filter in red [112]

Multiple iterations of the optimization of all parameters are carried out until a maximum output in terms of flux and highest cut-off energy for higher harmonics is achieved.

4.1.3 Focus size and divergence estimation

The beam profile of the XUV beam and the Rayleigh length is critical particularly for this setup, as shown in Fig. 2.9. The beam size at the interaction point tells how close to the center of the beam the gas nozzle can be brought. Considering this the beam profile at the interaction point in the experimental chamber is investigated by imaging the XUV beam on a CCD-camera with phosphor (Type P43) coated chip. A scan along the optical

axis over a range of ±15 mm is carried out. The focus size is estimated by fitting a two-dimensional Gaussian. The FWHM for both transversal directions are $w_x = 18 \pm 1$ μm in horizontal direction and $w_y = 290 \pm 11$ μm in vertical direction. The Rayleigh length is estimated to be z_x =197 ± 7 mm with half angle divergence of 0.18 ± 0.01 mrad and z_y = 744 ± 60 mm with half angle divergence of 0.78 ± 0.19 mrad. An astigmatic behaviour is observed due to a rather large angle of incidence of 20°on the imaging multilayer mirror. The beam profile at the focus is depicted in Fig. 4.3.

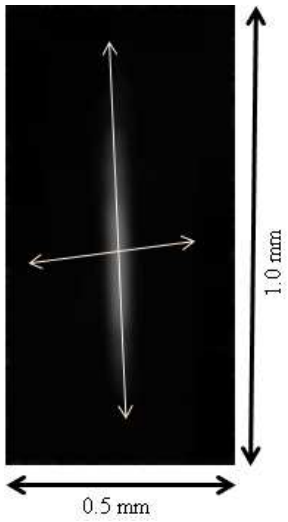

(a) Focus

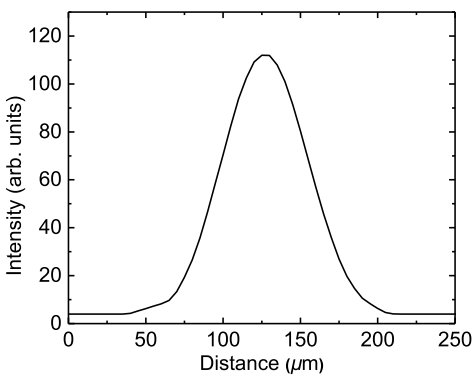

(b) Horizontal FWHM

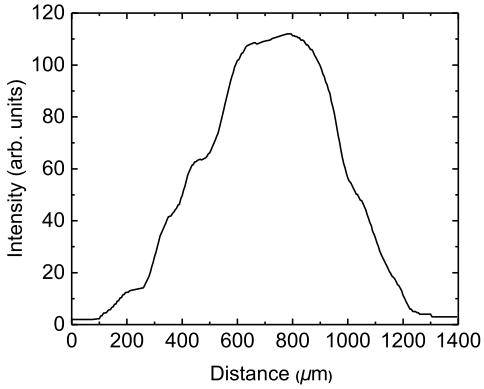

(c) Vertical FWHM

Figure 4.3: a:HHG beam profile at interaction point, Profile plots for b: Horizontal, c: Vertical directions.

The beam is slightly tilted in vertically direction. This tilt originates from the source itself and depends on the beam in-coupling inside the hollow fiber. As the target gas nozzle is inserted transversely [see section 3.4] a small width in the horizontal direction is beneficial in order to confine the interaction region. The interaction point is 4 mm in front of the focus due to system design however it is well inside the Rayleigh length.

4.1.4 Photon flux and conversion efficiency measurement

Assuming a pulse energy of 0.9 mJ and a pulse duration of 10 fs the maximum intensity reaching the HHG target is up to 5 x 10^{14} W/cm^2, this is an optimistic estimate as the pulse energy reduces after propagation from the HFC to the target(see Fig. 3.3). Using a silicon XUV photodiode(Type: SPD-1UVHCM, Technoexan LTD) the photon flux of the 57th harmonic order in the experimental chamber is measured to be 1.1 x 10 ^{4} photons/pulse after blocking the IR with two zirconium filters of thickness 200 μm each and 50% transmission each. The gradient and focusing multilayer mirrors give an overall reflectivity of 40% (see Fig. 3.4) this corresponds to 11x 10 ^{4} photons/pulse for 91.4 eV photons. This gives an energy conversion efficiency of 4.5 x 10^{-9} which is slightly higher than the efficiency achieved at setups developed with similar laser parameters [113, 114].

4.2 THz radiation generation and characterization

The THz source is characterized in terms of pulse energy, beam profile and beam divergence close to the source. The beam profile and pulse energy are also measured close to the interaction plane in order to investigate the possible influence of propagation in air and through a 3 mm thick in-coupling window made of TOPAS. Moreover it is important for the investigation of the focusing quality of the Zeonex lens with a 2 mm hole in the center. The THz beam is loosely collimated using a Zeonex lens with a focal length of 87.5 mm generating an intermediate focus at a distance of about 70 cm from the lens. Copper mirrors with 50 mm clear surface and a 99.99% reflectivity for THz radiation are used for transporting the beam from the source through air to the experiment. The total distance from the source to the interaction point is approximately 2.5 m.

4.2.1 Conversion efficiency

Due to the intense infra-red pump radiation hitting the crystal and getting scattered in random directions, a measurement of the pulse energy close to the crystal would have been highly misleading. For this reason the pulse energy is measured after the collimating lens by focusing the radiation using an off-axis parabolic mirror with a focal length of 100 mm. The collimation lens is made of Zeonex480R, which offers the minimum absorption coefficient of 0.015 mm^{-1} at 1 THz and a medium high refractive index of 1.5 [115]. The calibrated detector gave a signal of 471 mV corresponding to a pulse energy of 584 nJ. The calibaration factor of 1.24 nJ/mV is established by comparing the pyrodetector signal with THz-streaked signal in the work of Brannath [108]. However this number underestimates the actual pulse energy as the focus size, measured later, at this point is bigger than the detector size. With the knowledge of the absorption coefficient and the thickness of the collimation lens that is 10 mm the loss is 14%. Additionally there is an 8% loss due to reflection. Thus, the THz source provides about 712 nJ pulse energy. Compared to pump pulse energy of 550 μJ it corresponds to a conversion efficiency of 0.13%, which is comparable to the one achieved with other setups with similar pump parameters like in [78].

4.2.2 Beam transmission

After transporting the THz beam to the interaction point, the measured pulse energy in the focus is 320 nJ, Considering the pulse energy of 712 nJ delivered by the source this

corresponds to a beam line transmission of 45%. The transmission losses are quantified backward in the following:

The reflection and transmission losses at the focusing lens adds upto 22%. This means energy reaching the focusing lens is 410 nJ. The same reflection losses are associated with vacuum in-coupling window made of TOPAS, which also has a refractive index of 1.5 at 1 THz, the transmission loss through 3 mm window is just 4%, taking 90% transmission [115]. Adding this 12% the pulse energy reaching the window is approximately 467 nJ. The loss due to absorption in air is discussed in Sec. 4.2.6.

4.2.3 Beam quality estimation

For analysing the beam quality of the THz-radiation it is focused using a Zeonex480R lens with a focal length of 100 mm and the beam size at several positions behind the lens is measured applying a 2D-scan of the pyroelectric detector. The divergence of the THz beam is estimated from this focus scan. An image of THz-radiation test focus acquired by this arrangement inside the experimental chamber is shown in Fig. 4.4.

In order to estimate the beam waist and Rayleigh length the measured FWHM at different positions along the optical axis are fitted according to

$$\omega(z) = \omega_0 \sqrt{1 + (z/z_R)^2} \tag{4.1}$$

where z_R is the Rayleigh length given as $Z_R = \pi\omega_0^2/\lambda$ with ω_0 as the $1/e^2$ radius and λ as the wavelength of the radiation. It is important to mention that the obtained numbers do not correspond to the the source instead they only represent the used beam imaging system. The purpose of this characterization is to estimate the behaviour of the focused THz beam in the experiment. The fit for both transversal directions is depicted in Fig. 4.5. The fit results are given in Table 4.1. Where the first column gives the $1/e^2$ radius for the focus. The position of the focus is determined with respect to distance from surface of the focusing lens. The values of the divergence in horizontal and vertical directions are more

direction	$1/e^2$ beam radius (mm)	position of focus (mm)	Rayleigh length (mm)	divergence angle(degrees)
vertical	1.67 ± 0.5	88.9 ± 2	7.6 ± 0.6	2.4
horizontal	1.7 ± 0.6	90 ± 2.6	8.2 ± 0.6	2.7

Table 4.1: Experimentally extracted parameters for THz-radiation

close to each other as compared to for example the work of [83] where an elliptical pumping spot was used. In contrast in the present work the pump spot is rather symmetric but much smaller than the cited work hence reducing the absorption of THz-radiation inside the generation crystal and giving comparable divergence in the transverse directions. The beam waist at the focus is also very similar in both directions. After the intermediate focus the beam opens up. However the beam size is again measured close to the vacuum in-coupling window to make sure no clipping occurs and the full beam is transported to the interaction point. For the EOS and streaking experiment however a different focusing is used as mentioned in Sec. 3.2.2, using the effective focal length of 34 mm a focus spot with a FWHM of o.7 mm in both direction is achieved.

4.2.4 Polarization rotation

The polarization of the pump beam(for THz generation) is turned perpendicular to the optical table for efficient generation of THz-radiation before the generation crystal(see

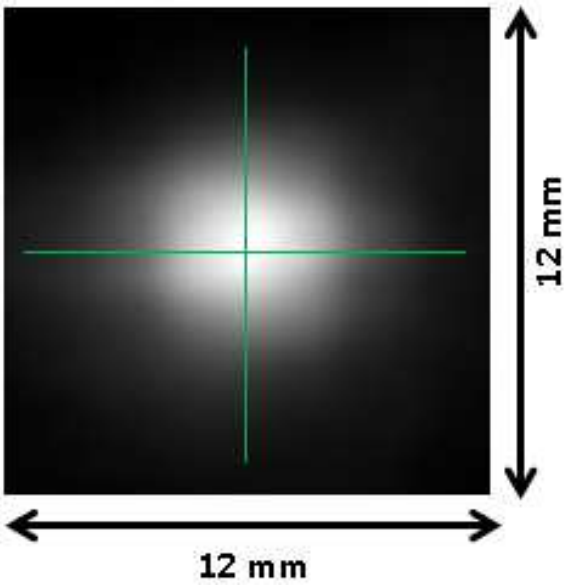

(a) THz focus in experiment

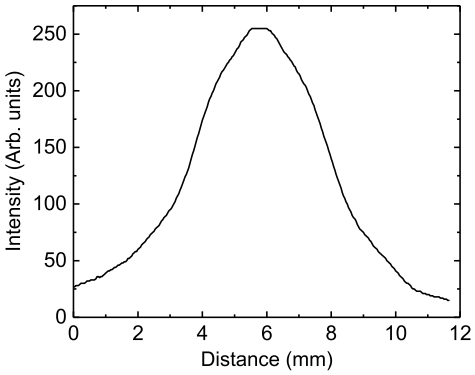

(b) Horizontal FWHM

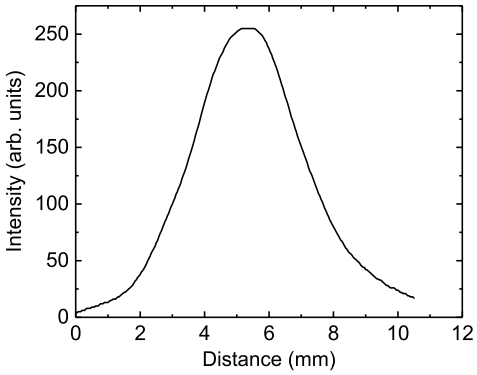

(c) Vertical FWHM

Figure 4.4: a. THz beam profile at test focus, Profile plots for b. horizontal and c. Vertical directions

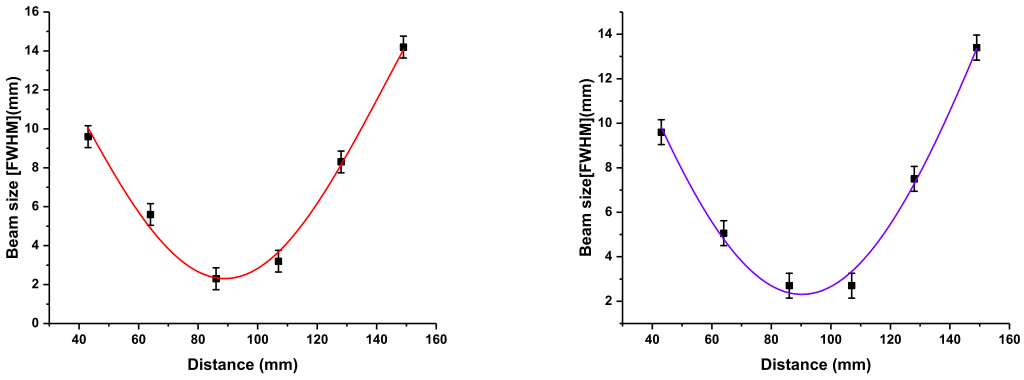

(a) Horizontal (b) Vertical

Figure 4.5: Depiction of the THz-beam size variation in a. horizontal and b. vertical direction achieved by beam profiling using the pyroelectric detector signal.

Sec. 3.2.2) and hence the THz-radiation is emitted with the same polarization from the crystal.

The XUV radiation is polarized along the direction parallel to the table. The polarization of the THz radiation is critical for the accurate measurement of derived parameters from the observed streaking, it should be parallel to the polarization of XUV beam in order to attain maximum streaking.

A periscope is installed to rotate the polarization of THz-radiation so that both, THz and XUV beam, are polarized parallel to the optical table. For the verification of the correct rotation of the polarization a home made wire-grid polarizer is brought in the beam path while measuring the signal on the pyro detector. It consists of an array of thin metal wires with a period of 3 mm. If the THz field is parallel to the wires, the electrons on the wire can move freely along the wire direction leading to strong reflection of the incident THz beam. Here the measured attenuation was 60%. As the polarizer is not perfect the signal is not attenuated completely. Whereas in the direction perpendicular to the wire the movement of the electrons is highly restricted so that for this orientation of the polarizer most of the THz intensity is transmitted. The measured signal was same as the initial signal, leading to the conclusion that the THz-radiation is polarized in this case parallel to the optical table after the periscope.

4.2.5 Infrared beam travelling with THz

In this work it is observed that a visible IR beam travels with the generated THz-radiation. It is challenging to figure out the source of this light in the crystal due to the intense pump-radiation. $LiNbO_3$ has a large refractive index discrepancy for IR and THz, for this reason it is very hard to realize that both beams leave the crystal with same angle and travel the same path. Stray light from the crystal is emitted in random directions, however this part of the light was observed to follow a similar path as the THz-radiation. This radiation even reaches the experiment. However using a fast photodiode the time difference between the two beams was measured to be almost 400 ps. Due to the spread of energy over a large time window it is safe to assume that the intensity of this wierd light is not high enough

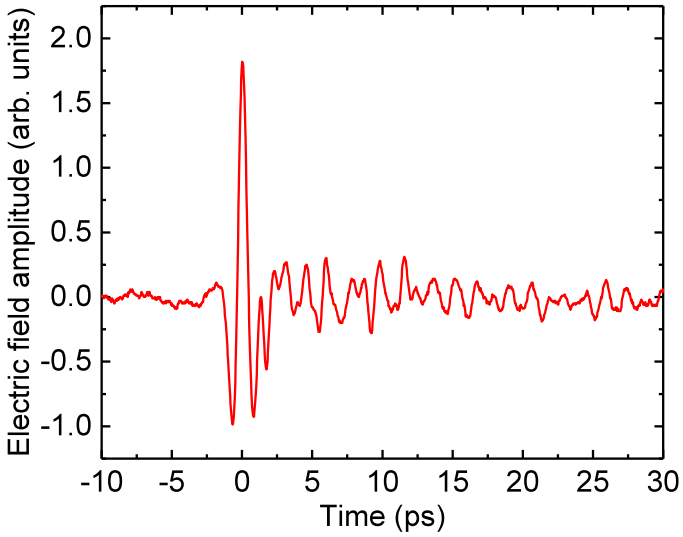

Figure 4.6: Electo-optical signal for different time delays between THz and IR beam.

to influence the experimental results.

Coming back to the time difference between the THz- radiation and this additional radiation it can not be explained by the reflections of the pump beam inside the crystal which would cause a time delay in the orders of a few ps. One possible explanation of this light is the back conversion of THz-radiation to IR. A detailed study of this stray light in terms of pulse energy and divergence may indicate the real source and with careful adjustment hopefully this radiation can be used as a convenient tool for guiding, the otherwise invisible, THz-radiation towards the experiment in the future.

4.2.6 Electro-optical sampling

The temporal and spectral properties of the THz pulses are investigated by electro-optic sampling(EOS). In this project EOS serves three purposes:

* achievement of temporal overlap of two beams,

* temporally and spectrally resolving the THz radiation, and

* measurement of the field strength of the THz radiation.

Fig. 4.6 depicts a delay scan of the measured signal for different time delays between the THz and the IR pulse showing the single-cycle behaviour of the THz pulses by the single main peak. This main peak is followed by a long oscillation. From the comparison of measured peak height of the signal and the background signal with no THz-radiation one can calculate the electric field strength according to Eq. 2.49. The maximum balanced detection signal acquired is $I_{max} = 0.8 I_p$. Taking into account Fresnel reflection losses for the intensity the THz radiation at the surface of the EOS-crystal of 28%, the corresponding field strength is 5 MV/m. Howeover it is known that EOS underestimates the THz field strength mainly due to saturation effects in the ZnTe crystal [83].

The spectrum of the THz radiation is obtained from a fast Fourier transform (FFT) of the temporal amplitude (Fig. 4.6) and is shown in shown in Fig. 4.7a. The central

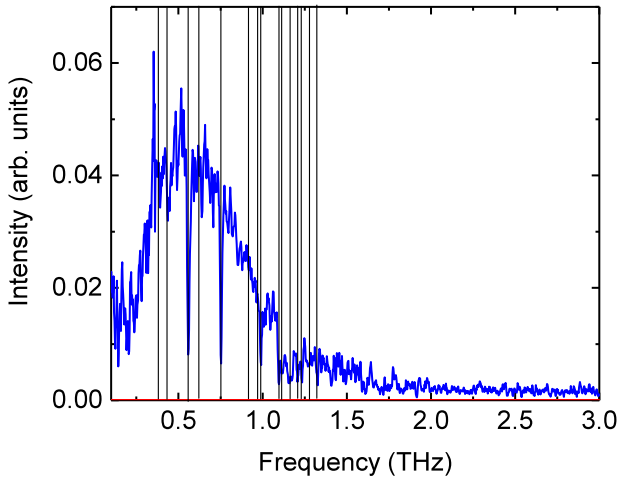

(a) Spectrum of THz-radiation, obtained through fast Fourier transform of EOS signal depicted in Fig. 4.6, with absorption dips marked with black lines

Number	Frequency(THz)
1	0.38
2	0.448
3	0.557
4	0.621
5	0.752
6	0.916
7	0.97
8	0.988
9	1.097
10	1.113
11	1.163
12	1.208
13	1.229
14	1.278
15	1.296
16	1.322

(b) Absorption dip positions

Figure 4.7: Spectrum of THz radiation with specified absorption dips

frequency is 0.6 THz. Some additional peaks are observed at 1.3 THz and 1.8 THz, these can be taken as the harmonics of the THz beam as mentioned in [83].

THz-radiation absorption in air

The water absorption dips marked with black lines in Fig. 4.7are caused by absorption by water present in air [116]. This absorption loss increases with relative humidity, propagation distance as well as the frequency of the THz-radiation. The positions of these absorption dips as measured in THz time dependent absorption spectroscopy for air with comparable relative humidity in [116] and [117] in the order of increasing frequency are listed in the table in Fiq. 4.7. Due to a long propagation distance in air, these dips are rather stronger as compared to Fig. 4.11 of [108] where the same source used. The reason is that in the present case the THz-radiation travels twice the distance compared to [108]. By adding the areas of the absorption dips and comparing it with the area under the whole spectrum the loss due to absorption amounts to 20%. Adding this loss the pulse energy is 584 nJ. which is same as the energy after the collimation lens.

Chapter 5

VMI spectrometer

A VMI spectrometer with several new features is implemented for electron spectroscopy. The purpose is to investigate the final energy and angular distribution of electrons created as a result of the interaction of the XUV beam with an atomic gas. As the electron signal detected by a VMI spectrometer is distributed over the whole 4π steradians angular range the extraction of the spectral information e.g. an energy spectrum requires the inversion of measured 2D images to a three-dimensional distribution. These special features of VMI setup implemented in this work in order to be efficiently used with the laser based XUV source are discussed in the following in detail.

5.1 VMI spectrometer with collinear geometry

Typically a VMI setup is oriented such that the beam propagates parallel to the detector [21, 23, 91, 92, 118–121]. In this work, a VMI spectrometer with collinear geometry, that is the beams propagate along the VMI axis, is successfully implemented. For a VMI spectrometer the critical prerequisite is that the electron distribution is symmetric along an axis parallel to the two dimensional detector, only then the measured two dimensional data can be inverted to a three dimensional distribution and meaningful information can be extracted. For dipole excitation the symmetry of electron distribution is governed by the polarization axis of the exciting radiation. Hence the experimental arrangement should be such that the polarization axis of the exciting radiation is oriented parallel to the detector surface. The advantage of the collinear geometry is that this setup can be used for any orientation of linear polarization. This is shown in Fig. 5.1 for any orientation of linear polarization the polarization will still be parallel to the detector and hence the 3D-momentum information will be preserved.

The disadvantage of this arrangement is that it can not be used with circularly polarized light which produces an asymmetric electron distribution along the optical axis. The preferred direction for electron ejection will be towards the detector to which the beam is travelling and less electrons are ejected in opposite direction making the inversion unreliable.

The second advantage is that the light beam is visible on the detector and hence the alignment is more convenient, otherwise, this also can be a disadvantage in the sense that if a detector is exposed to an intense beam for some time its detection efficiency degrades [122]. In our work we made sure that the beam was blocked with a thin beam blocker made of copper after the VMI assembly to not hit the detector during the measurement.

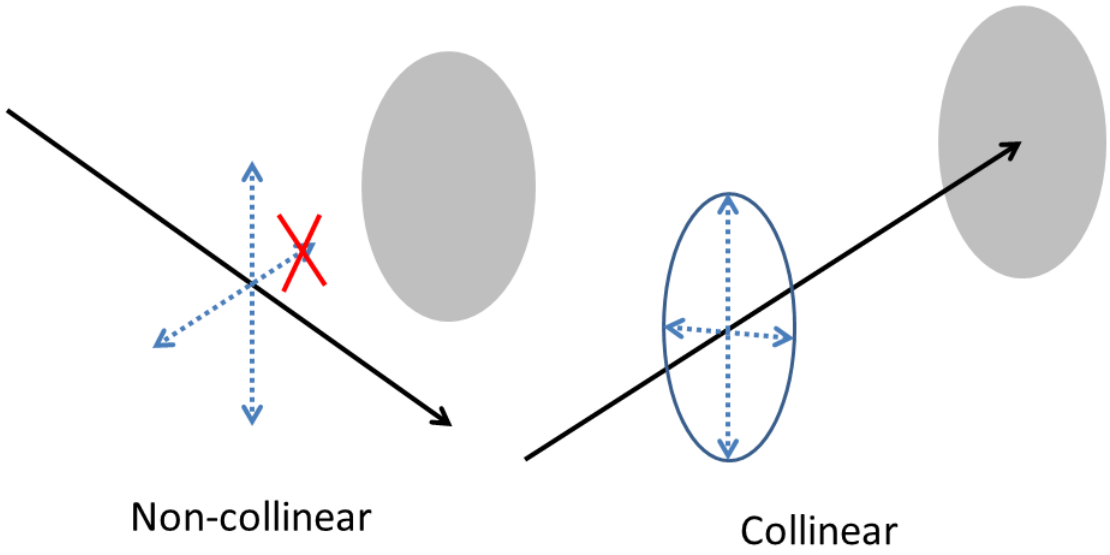

Figure 5.1: Setup schemes for VMI's in collinear and non colinear geometry. The non collinear geometry can not be used for certain orientations of linear polarization. Whereas with our collinear case any orientation of linear polarization can be used.

As the slow electron signal appears at the center of the detector it can be blocked if the beam is appearing in the center of the electron signal. However, in our cases the beam hits slightly above the slow electron signal (due to the experiment's geometry) and the signal blocked by the beam blocker is not significant as shown in Fig. 5.2.

A further advantage of this arrangement is a convenient in-coupling of the XUV and THz beams for the streaking experiment.

To obtain optimal imaging conditions for the VMI, the central repeller aperture is exchangeable since this affects the local electric field close to the interaction point. The effect of the different sizes of this in-coupling pinhole on the final radial position of neon 2p electrons signal with initial energy of 70 eV is depicted in Fig. 5.3. An ensemble of 1000 electrons are taken for each size of the pinhole. The smallest pinhole size of 2.4 mm gives a radial position 42 $\pm$ 1.64 mm, the 4 mm pinhole gives 41.8 $\pm$ 0.53 mm and the 5 mm pinhole gives 41.5 $\pm$ 0.52 mm. The radial position of the electron signal changes slightly due to the change of the local electric field at the interaction point. The resolution seems to get better with a bigger pinhole mainly due to a better focusing conditions.

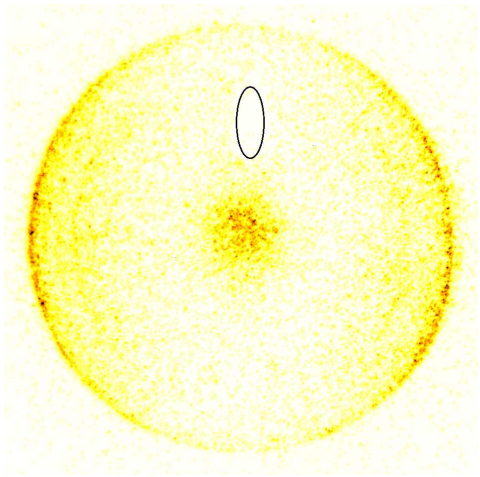

Figure 5.2: A raw VMI image for neon accomulated over 100000 shots, the signal blocked by beam blocker is marked.

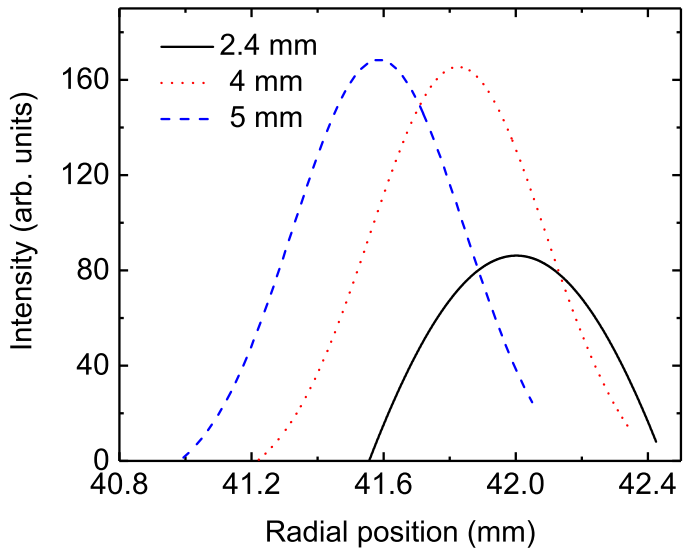

Figure 5.3: Effect of the repeller aperture size on the imaging properties of the VMI. Shown are three different aperture sizes 2.4 mm: solid line, 4 mm: dots, 5 mm: dashed.

5.2 Simulation of new design

Before operating the VMI spectrometer it is simulated with a 3D geometry in an ion-optics simulation software SIMION. Light optics can be modelled by physical optics-benches giving the possibility to place light sources, lens or detectors. An ion-optics bench consists of similar elements for charged particles. Using SIMION a 3D-optic bench is virtually modelled and can be investigated internally. Here a 3D- electron-optics bench is designed

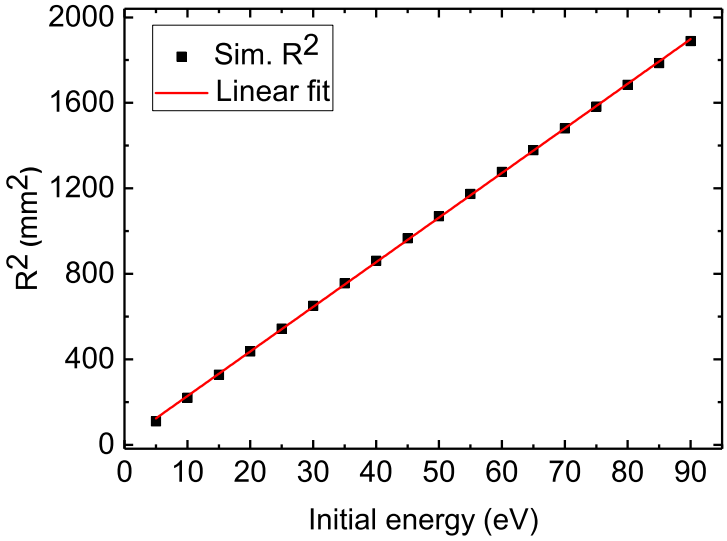

Figure 5.4: Initial kinetic energy E versus radius square of electron ring's radius R, simulated data using SIMION

that resembled the actual VMI setup. Referring back to Fig. 2.9 the voltage applied to the repeller electrode is V_R, for extractor electrode it is V_E. With decreasing V_R the rings on the detector expand towards the detector edges, hence the resolution gets better. However the detection efficiency of the PSD decreases the signal strength drops as the acceleration voltage is lowered(see Fig. 5.9). Experimentally the best compromise between resolution and signal strength is found at the repeller voltage of 8000 V. Hence for simulations this acceleration voltage is considered.

An important feature of a VMI spectrometer is the linear relationship between an electron's initial transversal momentum and the radial distance of the blobs on the detector. This relationship can be verified by checking the dependence of the initial kinetic energy E and the square of the electron rings's radius R^2. For the current spectrometer the simulated E-R^2 plot for an optimum Voltage setting is shown in Fig. 5.4. It is necessary to verify this relationship for the reliable calibration of the VMI spectrometer. The other critical parameter for the VMI spectrometer is the radial and hence the energy resolution. In order to extract the energy resolution from the radial resolution the following relationship for relative resolution is used

$$\frac{\Delta E}{E} = 2\frac{\Delta R}{R}, \tag{5.1}$$

which is derived from the relation $R^2 \propto E$. Using this the simulated relative resolution curve for 8000 V V_R with optimum V_E of 6356 V and for gas nozzle voltage at 7690 V is shown in Fig. 5.5. For this simulation an interaction region of radius 400 μm is considered, the energy range is 5 - 90 eV and for each energy 1000 electron trajectories are considered. For electrons with kinetic energy above 25 eV energy the relative resolution stays less than 5% or on average less than 1.2 eV. Here the spatial resolution of the detector is not taken into account, which will reduce the resolution further. For slow electrons the resolution

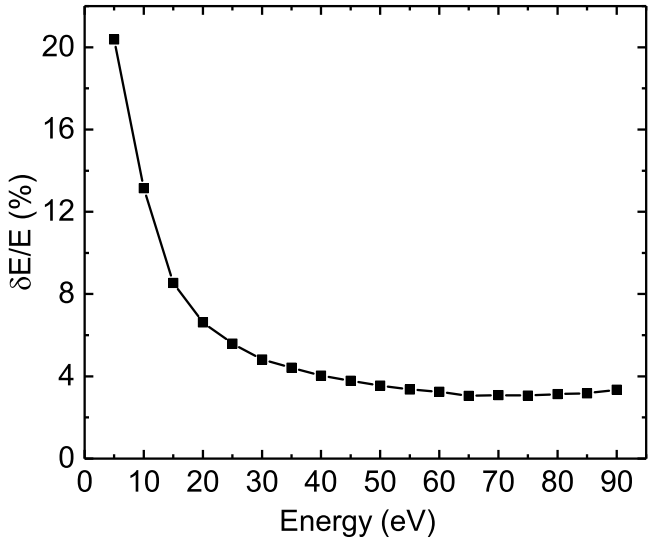

Figure 5.5: Simulated relative resolving power of VMI at optimum repeller voltage

gets worse mainly due to the accumulation close to the detector center.

5.3 Transverse Insertion of gas nozzle

For linear photoionization processes the ionization takes place all along the beam path which means that the interaction region is not confined along the optical axis causing the destruction of focusing of the electron signal by the VMI setup on the detector. This can be solved by using a localized gas inlet very close to the interaction region between the electrodes. With this arrangement electrons are born at the same potential. For this reason a thin gas nozzle is inserted transversely between the extractor and repeller electrode (Fig. 2.9). As the gas nozzle is placed in the space of a field gradient, it has to be supplied with the according potential and aligned exactly parallel to the equipotential lines, such that it does not distort the field gradient. This arrangement not only allows for a high target density but also confines the interaction length along the optical axis as the nozzle can be approached closely to the optical axis.

The spatial position of the gas nozzle is critical for the homogeneity of the electric field between the repeller and the extractor electrodes and hence a displacement from the optimal position will lead to a distortion of the expected circular ring structures on the detector, hence reducing the resolution. After optimizing the nozzle position in all three directions manually different strategies are used for fine adjustment under vacuum conditions. In order to optimize the horizontal position a knife edge scan of the beam by the gas nozzle is carried out such that the nozzle cuts the beam in two halves. The beam size at the interaction point is 400 μm FWHM in vertical direction and 18 μm FWHM in horizontal direction. As the nozzle's outer diameter is just 290 μm FWHM it does not block the beam completely. Then the nozzle is first set to a position such that the full

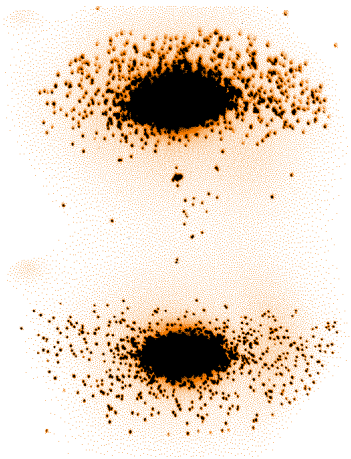

Figure 5.6: Surface electron signal when the gas needle is crossing the HHG beam

beam is visible on the detector.

For the optimization of the vertical position of the nozzle with respect to the beam the nozzle is moved inside and the voltages are switched on to see the surface electron signal on the detector. The vertical position is optimized after applying nominal voltages and making the surface electron signal symmetric in vertical direction, as can be be seen in Fig. 5.6.

The position of the nozzle in the z-direction (which is the propagation direction of the beam as well as the direction of the DC field of the VMI) determines the required voltage to be applied on the gas nozzle. The VMI spectrometer resolution also gets affected by the position of the nozzle in the z-direction at most. For the current configuration of the VMI the nominal position of the gas nozzle is 4.5 mm from the repeller. After adjusting this distance carefully, the voltage on the gas nozzle is optimized to obtain electron rings with optimum sharpness and circularity. The effect of a detuned nozzle voltage is visible in the images shown in Fig. 5.7. With V_R and V_E set to 10 kV and 8 kV respectively the gas nozzle voltage is varied to get sharp and symmetric rings on the detector. Starting from the nominal voltage of 9470 V it is found that at a voltage of 9355 V at the gas nozzle the rings get symmetric. A deviation of $\pm 0.16\%$ already deforms the ring. The amount of acceptable voltage detuning depends on the electric field magnitude at the nozzle position which decreases with decreasing absolute value of voltages making the acceptable voltage for gas needle more restricted. A deformed electron signal hinders the possibility to acquire reasonable spectral information after Abel inversion where a perfect circular signal is required.

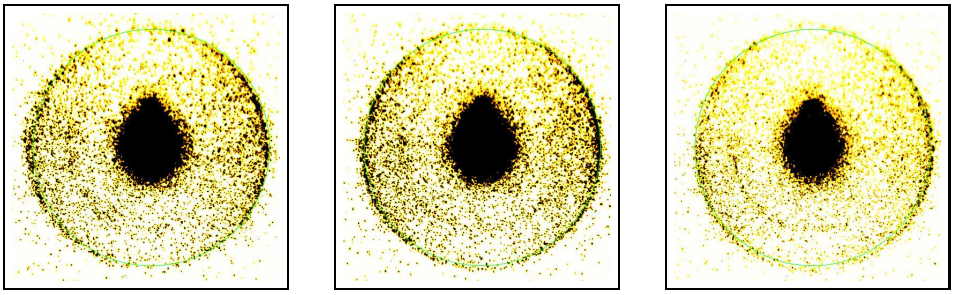

Figure 5.7: The image on the right is with nozzle set to a voltage less than optimum: a deformation of the signal on the right side is visible. The central image is with optimum voltage having a sharp ring shaped signal which is nicely circular. The image on the left is with more than optimum voltage where the ring is deformed to an ellipse.

The main feature of the gas nozzle is to supply the sample gas under investigation at a desirable high partial pressure in the interaction region. Hence, the throughput of the gas nozzle has been simulated using a Direct Simulation Monte Carlo (DSMC) simulation software DS2V, specifically used for simulating two dimensional axially symmetric gas flow. For this purpose the geometrical design of the gas nozzle is sketched in the software and an input pressure is given. The value of this input pressure is estimated by using the backing pressure in the vacuum chamber, and comparing the size of the vacuum chamber and the gas inlet. The program gives various choices for the gas to be used. Once all the parameters are given, the program calculates the two dimensional spatial distribution of particles at the exit of the gas nozzle taking into account the fluid dynamics and the mean free path. The conversion equations for fluid dynamics are satisfied here. Taking xenon as the gas of interest with a backing pressure of 1E-4 mbar in the chamber, which gives a initial pressure of 0.4 bar at start of the tubing before the gas nozzle the simulation results for the used gas nozzle are shown in Fig. 5.8. At the tip of the nozzle the resulting particle density is 1.75x $10^{22}/\mathrm{m}^3$ corresponding to a pressure of 0.58 mbar. As the minimum distance between the gas needle and the beam has to be 0.4 mm due to the surface electron signal, the gas density at this position is of interest since the nozzle can not be moved closer to the interaction region. A plot showing the drop of the number density of gas atoms per cubic meter is shown on the right side in Fig. 5.8b. At the distance of 0.4 mm the number density drops by a factor of 2.4, the absolute density at the working point is 3 x 10^{21} $/\mathrm{m}^3$ that is the local pressure in the interaction region is upto 10^{-1} mbar.

In a conventional VMI setup the gas is supplied through a skimmed atomic (or molecular) beam. Although in that scheme the gas is used at a position of well defined initial velocity, the drawback is that a higher backing pressure of gas is necessary to be applied in order to achieve reasonable gas density at the interaction point. Our scheme of transversal insertion of gas nozzle is superior to that as the distance between the gas nozzle and the beam is just 0.4 mm enabling the use of orders of magnitude higher target densities. An improvement of conventional gas inlet was implemented by Ghafur et. al. in [21] by using a gas injection integrated in the repeller plate but that scheme is much more complicated and hard to implement especially in the simulations where a discretization of the gas nozzle is required in order to model it correctly. Whereas with our scheme with transversally inserted gas nozzle, both simulations and experimental work is less tedious and gives same photon absorption probability. Hence this scheme is specially suitable for

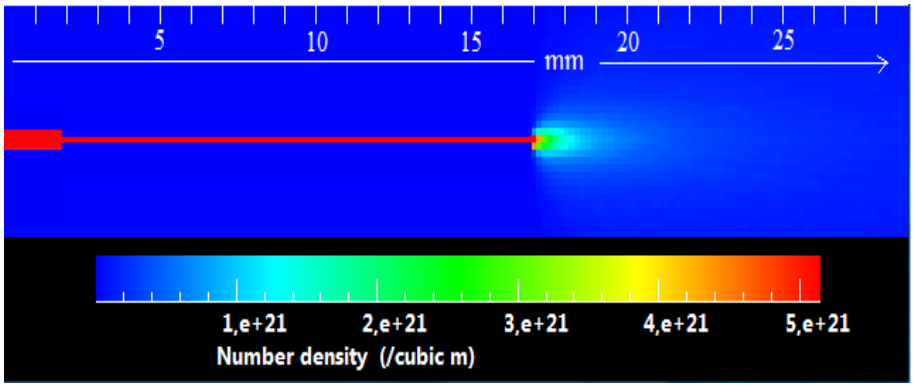

(a) Snapshotz of gas flow simulations

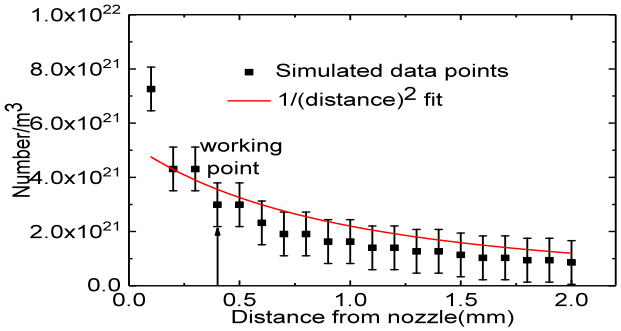

(b) Plot of gas density as a function of distance from nozzle

Figure 5.8: a: False color map of gas flow from gas nozzle, b: Number density of gas atoms as a function of distance from the gas nozzle

weak light sources for example the laser based HHG sources. With the presented setup a count rate as high as 20 counts per shot with xenon is achieved.

5.4 High efficiency electron imaging detector

As described in Sec. 3.4.2 a novel PSD with a special design is used in this project. The commercial PSD has a cascade of signal amplification components and hence offers a quantum efficiency of close to 1, giving a measurable signal for almost each incident electron. The calculation of this quantum efficiency and its influence on the resultant signal to noise ratio is explained in the following.

The large size of the detector (diameter 150 mm) gives the possibility to detect electrons with energies upto 200 eV with optimum efficiency. Moreover, this size of the detector also ensures improved energy resolution by projecting Newton spheres of increasing diameter at distinct radial positions and less fitting of high-KE distributions to the detector size is required [123].

Referring back to Fig. 3.8, the electrons created in light-matter interaction at first encounter a phosphor screen where a part of their energy is converted to photons, the rest of the energy is converted into heat. This conversion depends on the kinetic energy the electrons gained during their acceleration in the VMI field hence the photon yield is

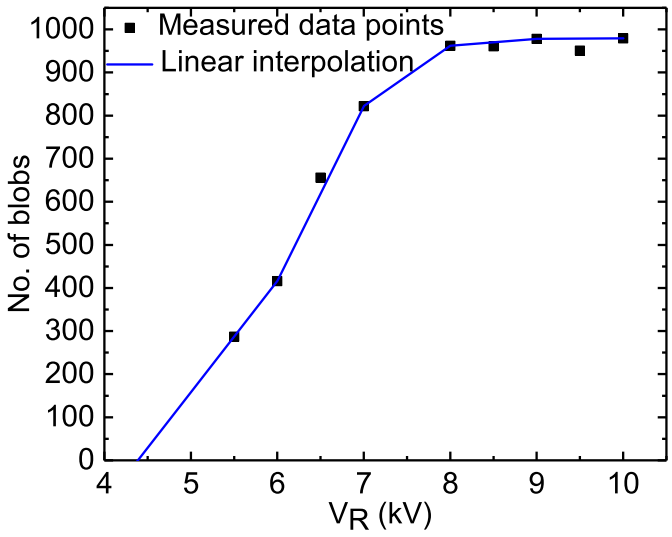

Figure 5.9: Number of blobs detected as a function of applied repeller voltage

expected to be directly proportional to the voltages applied to the electrodes of the VMI. As depicted in Fig. 5.9, the measured number of blobs show a increase with increasing voltage V_R up to 8.5 kV, above this voltage a stabilization of detection efficiency value is observed. The drawback of this detection scheme is that only those electron are transmitted which have already acquired a kinetic energy above 3 keV (see Sec. 3.4.2). This directly puts a limit on the applicable acceleration voltage V_R which is above 4 kV as depicted in Fig. 5.9. Here we calculate the detection efficiency for an acceleration voltage of 10 kV. After the energy loss due to transmission through coating layers(Refer to Sec. 3.4.2) the electron has an energy of 7 keV . At this energy the efficiency for the phosphor screen is 0.72 W/mA , this value is estimated from the table given in [109] for varying electron acceleration potentials. Using Eq. 3.1 this number is converted to number of photons/electron. Each electron impinging on the phosphor screen may be converted into about 317 photons on average. The taper coupling the phosphor screen to the photocathode has a transmission of 5% reducing the number of photons to 16 photons/electron. The photocathode has a quantum efficiency of 10.2%. Hence the average number of electrons delivered by the photocathode is 1.6 per one initial electron. In this way the MCP-stack gets 1.6 electrons/initial electron to be amplified. In a conventional detection system comprising of a MCP assembly followed by a single phosphor, the number of electrons amplified per incident electron is well below 1 [110]. The reason behind this that for a conventional MCP the Open Area Ratio(OAR) is 60% and not each electron hitting the MCP gets amplified, instead the amplification process follows a probability distribution. For the double MCP stack in chevron shape the efficiency can be taken as 60% based on the data presented in [110, 124, 125] leading to delivery of 0.96 electron per one initial electron. Giving a quantum efficiency of 96%. Which is a factor of 1.6 higher than the one offered by a chevron shaped double MCP stack+ phosphor.

The numerical aperture of the objective imaging the phosphor screen is 0.44 giving the

collection efficiency of 5%. In the end the efficiency of the Basler camera at 545 nm is 50%.

A higher quantum efficiency of an imaging system gives a higher signal to noise ratio [126]. An analysis of the Pulse Height Distribution (PHD) for this detector is carried out in the following. A PHD is a histogram for the brightness of a blob appearing on the output phosphor screen. PHD illustrates how well the differentiation of signal and noise is possible with the given detector. PHD generated from stacks of 502 images attained with $V_R = 8$ kV is shown in Fig. 5.10a where 10 counts/image are recorded. For comparison the PHD for a conventional two stage MCP + phosphor detector imaged with digital Basler camera(type acA1920-16 μm) is depicted in Fig. 5.10b for the same number of images with 20 counts per image. For the purpose of comparison same binning and same range of mean gray values is used. The ratio of the peak and valley for current detector at this voltage is

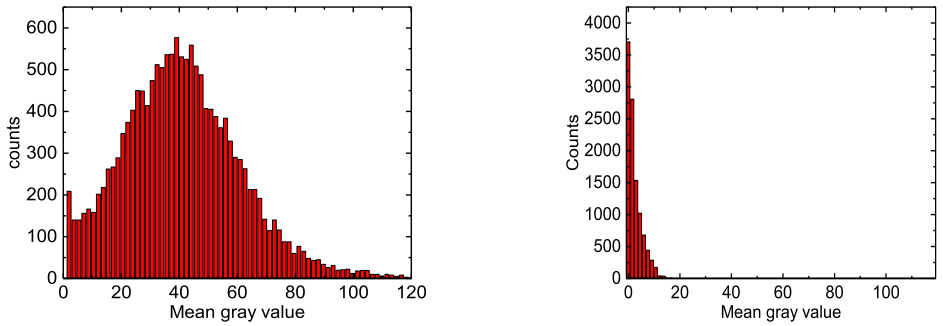

(a) VMI detector at 8 kV with Basler camera (b) Typical two stage MCP with 1kV/plate

Figure 5.10: PHD for a. current detector. and b. Typical MCP taken from [124]

3.7:1. It is also found that for current detector the peak shifts to higher gray values with increasing V_R making it more efficient than typical imaging detector. The pulse height resolution is given as

$$\text{pulse height resolution} = \frac{\text{FWHM}}{A}, \tag{5.2}$$

where FWHM is the width of the distribution at half maximum and A is the difference of mean gray value for peak and noise. For the used detector it is 120% at 8 kV acceleration voltage giving a reasonable separation between the noise and the signal for this detector making the acquisition of noise free data possible, this feature is utilized in Blob analysis in Subsec.5.5.2. For the typical detector it is not possible to extract these numbers.

5.5 Operation of the VMI spectrometer

The XUV beam with photon energy of 91.4 eV interacts with the target gas supplied through the thin gas nozzle.

One of the goals of the experiment is to apply the highest possible target density and measure the electron streaking in order to investigate the interaction of one electron with its environment. As a first step a voltage breakdown test is performed. For this purpose the detector is replaced by a blind flange, the voltages are switched on setting the V_R to 10 kV, V_E to 8 kV and the nozzle voltage set to 9.355 kV. The gas pressure is increased

slowly in order to check for the breakdown of the voltage. The pressure reached without any voltages breakdown are 1.4 x 10^{-3} mbar for neon and 1 x 10^{-4} mbar for xenon.

The gas pressure used for neon in this work is 5.7 x 10^{-4} mbar considering the calibration factor the estimated target density is then 3 x 10^{22} /m^3.

5.5.1 Image inversion

VMI spectroscopy has the advantage that both spectral and angular information can be extracted from a single measured image. However, in order to extract this information of electrons from a raw VMI image the 2D image has to be transformed to a 3D distribution. As mentioned in Sec. 2.5.4 in this work the Vrakking code [95] and the POP code [96] are used to transform the measured images. An example raw VMI image accumulated over 960,000 shots with neon and the corresponding transformed image are depicted in Fig. 5.11. The Vrakking code seems to retain the angular distribution however it exhibits a very bad signal to noise ratio and it does not show the 2s ring. in contrast the POP code gives a meaningful inverted image. The image inverted using the Vrakking code shows some

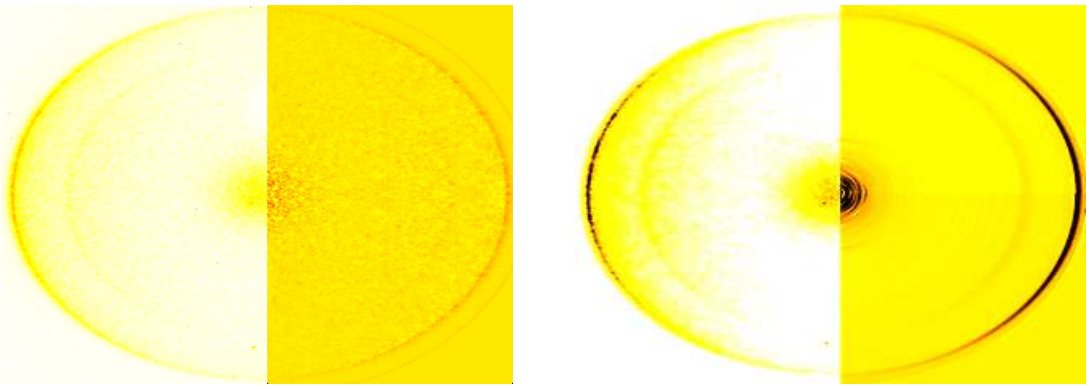

(a) Inversion using Vrakking iteration code (b) Inversion using POP code

Figure 5.11: Left:Left half is raw image right half is the Vrakking code inversion and right: left half raw image and right half transformed using POP technique. For the purpose of visibility different gray value scaling is used for both images.

signal free area along the central vertical line. The image inversion using POP gives a much better result retaining the angular distribution as well as all involved photoelectron rings.

The VMI-setup can be used to extract angular information, as well. As discussed before, the Photoelectron Angular Distribution(PAD) follows a well defined distribution with respect to the polarization axis of the ionizing beam, by extracting the value of β-parameter one can determine this polarization state. An extensive study of PADs is not the scope of this work, therefore only one example for neon data is presented. At an excitation energy of 91.4 eV the possible photoelectron rings correspond to electrons originating from neon 2p and 2s states. The spin orbit spiting of 0.1 eV of the 2p-state can not be resolved. The image obtained on the detector is the sum of contributions from photoelectrons from the two shells. For extraction of information of the angular distribution the measured PAD with respect to the polarization axis is fitted according to Eq. 2.50.

The fit and the polar plot for neon 2p are shown in Fig. 5.12. The beta parameter for 2p is estimated to be 1.06 $\pm$ 0.04 which is quit close to the expected value of 1.1 [127].

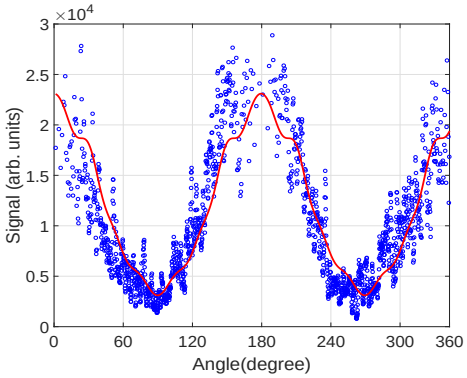

(a) Fit for neon 2p

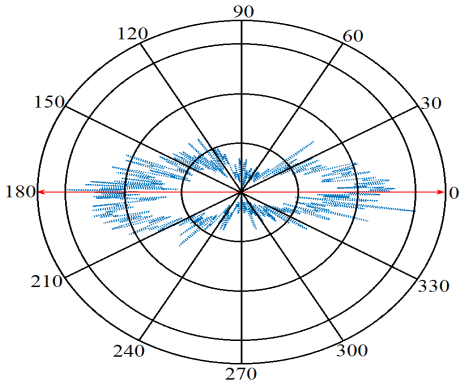

(b) Polar plot for neon 2p electrons

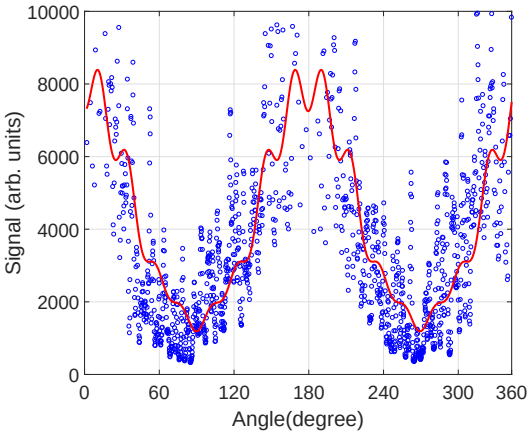

(c) Fit for neon 2s

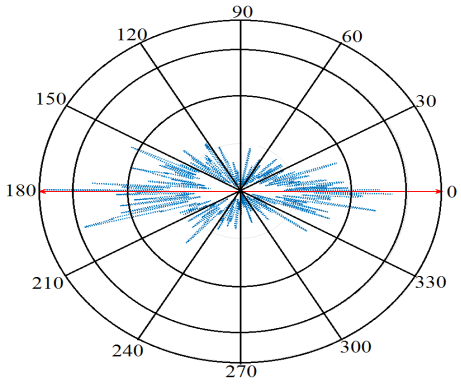

(d) Polar plot for neon 2s electrons

Figure 5.12: Fit and Polar plot for neon 2p. The polarization axis is indicated by the red arrow.

Similarly the beta parameter for neon 2s is found to be 0.79 ± 0.05 which is slightly away from expected value of 0.60 [127] most probably the reason is the very low signal to noise ratio which makes the fitting worse. The left right asymmetry is 3.6% the possible reason for this is an asymmetric efficiency of detector. In order to deal with this a contrast matching on both sides of electron momentum maps can be applied.

5.5.2 Blob analysis

The resolution of the PSD is limited to 24 lines/mm as stated in the manual [111], in order to overcome this limit the technique of blob analysis is used. A blob is a region of connected pixels with Gaussian like intensity originating from a single event/particle hitting the detector. The principal idea is to identify these regions in an image and determine the center for each blob, which can be identified with a high precision. A threshold intensity value is set to remove the noise. All blobs with intensity above the given threshold are replaced by a single pixel blob. The motive behind implementing the blob analysis protocol is to improve the resolution by making the signal blobs more distinct, at sufficient signal to noise ration (SNR), sub-pixel resolution can be achieved. In the following the advantage of the blob analysis routine is demonstrated by comparing evaluated data with and without applied blob analysis. For this purpose data measured with neon is used. A camera image accumulated for 10,000 shots and the respective spectrum (achieved after image inversion using POP algorithm) without blob analysis is depicted in Fig.5.13a and Fig. 5.13b.

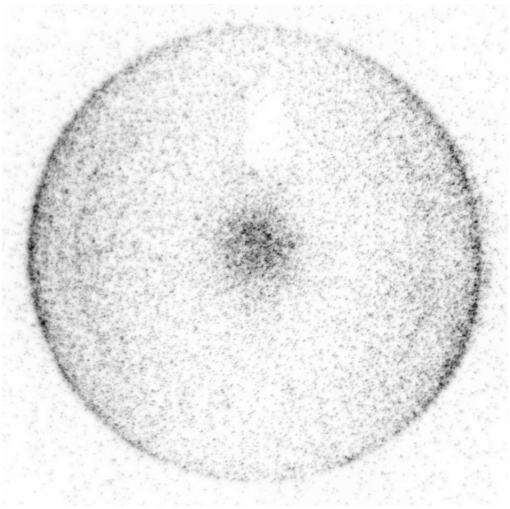

(a) A raw camera image

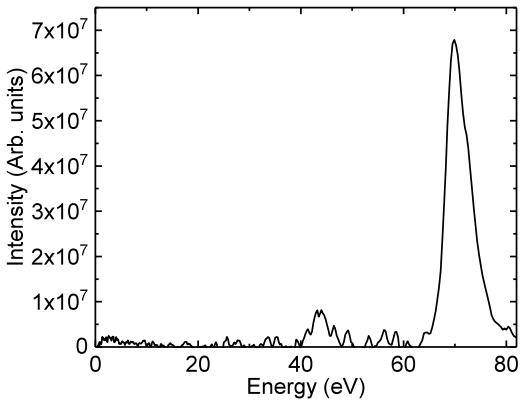

(b) spectum extracted from raw image using POP inversion

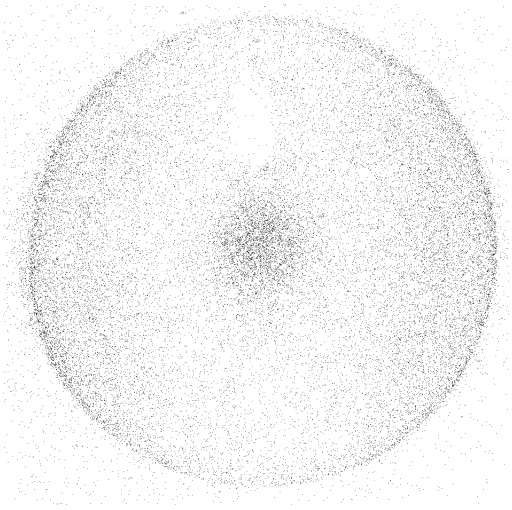

(c) Blob plot

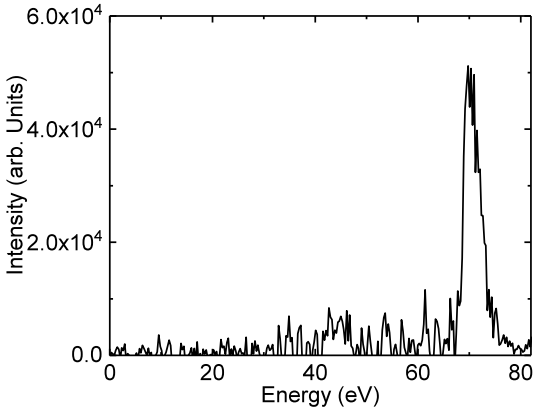

(d) spectum extracted from blob plot using POP inversion

Figure 5.13: (a) A raw camera image, (b) spectrum from camera image, (c)Blob plot, (d) spectrum from blob plot.

For blob analysis, or more precisely to replace each blob belonging to the signal by a single pixel(which can be smaller than the pixel in the original image), the first step is to separate the noise from signal. This is done by estimating the threshold for the intensity for a blob to be considered as signal blob. Once this threshold is given the algorithm starts separating the signal blobs. For the purpose of accumulation of data with signal blobs a Region Of Interest (ROI) is selected on the live image of the camera. The algorithm spreads this ROI over an image of size 1024 x 1024 pixels. A blob image and respective spectrum (obtained after image inversion using POP algorithm) is presented in Fig. 5.13c and Fig. 5.13d.

The energy resolution for the camera image is 6.8% at 70 eV. For blob plot it is 4.6% at same energy value. There is a factor of 1.5 improvement with Blob analysis. The performance of a blob analysis depends on the successful differentiation of the image that is separating the signal blobs from noise blobs. The improvement of resolution confirms

that this approach can be applied successfully with the novel detector. In order to measure the experimentally achieved resolution the above mentioned number must be de-convoluted with the excitation bandwidth of 1.4 eV(extracted from the plot given in Fig. 3.4). The resulting numbers are 6.5% without and 4% with blob analysis. The blob analysis gives a relative resolution close to the simulated value of 3%. Hence the Blob analysis protocol is successfully implemented to beat the limiting detector resolution.

5.6 Zero kinetic energy electrons

A large number of electrons are detected in the center of the detector. These are very slow electrons also known as zero kinetic energy electrons. In order to estimate the minimum resolvable energy value it is important to have the knowledge of the range energy for these very slow electrons. Referring back to the Fig. 5.13c the central spot covers upto 3 eV$\pm$ 1 eV.

Chapter 6

THz streaking using VMI spectroscopy - simulations and experiment

In this chapter two final aspects of the project are presented. In the first part the results of a 3D-simulation of the THz streaking observation using a collinear VMI spectrometer are summarized. In the second part the findings of the proof of principle THz streaking experiment are listed.

6.1 Electron-optical simulations of THz streaking

6.1.1 The case of small VMI electric fields

The DC field from the VMI is parallel to the electron propagation in this work as depicted in Fig. 2.16. In order to investigate the influence of this DC field on the streaking dynamics, a simulation is carried out in SIMION. The time dependence for the THz-field is implemented with the help of an embedded script where a transient field is introduced for the particles after their creation. The properties of the THz field are modelled according to the experimentally measured values. These are the focal spot of 1 x 1 mm^2, the oscillation frequency is taken as 0.6 THz and the period of 1.6 ps and the pulse duration is taken as 900 fs. The geometry used for the simulation is depicted in Fig. 6.1. The y-axis is designated as polarization axis and the electron travel along this axis initially. The streaking field is introduced between two thin sheets A and B as shown in Fig. 6.1 and is also polarized along y-axis.

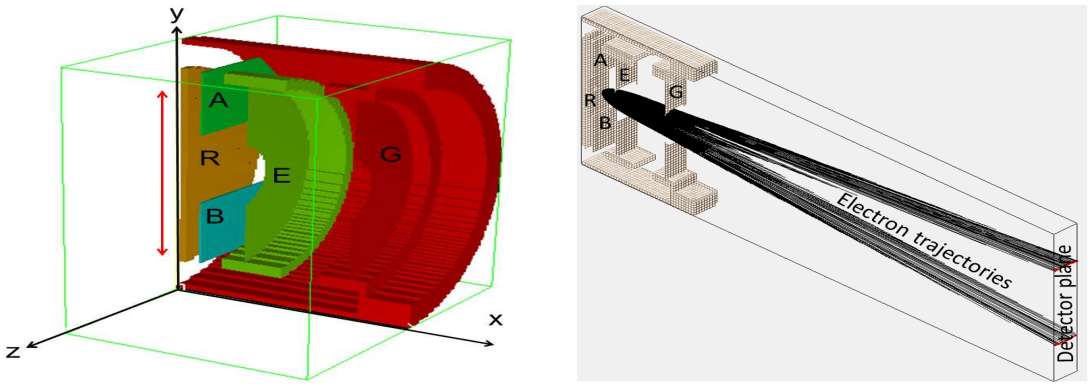

(a) Geometry of the simulated setup (b) Trajectories of the simulated electrons

Figure 6.1: Depiction of geometry used for electro-optical simulations. a. The 3D dimonstration of VMI electrodes R:repeller, E: extractor and G: ground and electrodes used to implement time dependent streaking field at interaction point A and B, b. A cut along yz plane of the setup showing the electrodes and trajectories of simulated electrons.

For the validation of the simulation, the shift of the electron signal for typical THz-field strengths with a typical small DC field is compared to the theoretically calculated values based on the analytical formula in Eq. 2.79(see Fig. 6.2) where no dc field is included. For this simulation trajectories of 500 electrons are considered. It is obvious that the theoretical and the simulated values of the energy shift match well within the accuracy limits represented by the error bars. This assures that the simulated setup can be reliably used for further investigations.

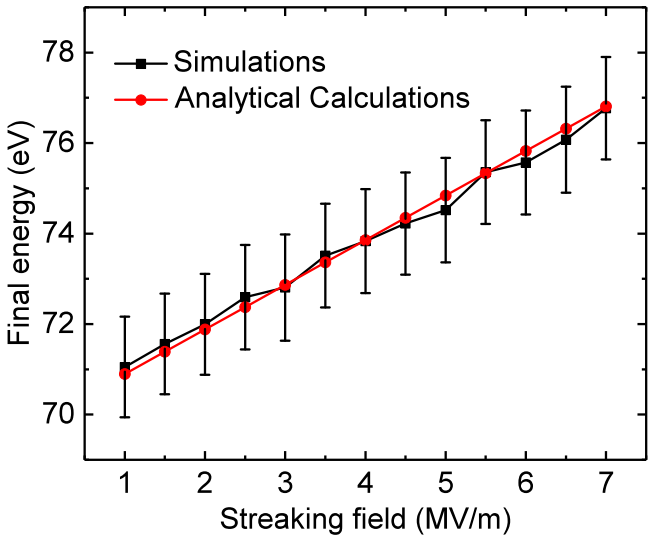

Figure 6.2: Simulated and calculated electron final kinetic energy as a function of THz-field strength.

In order to investigate the possible effect of the VMI field on the streaking process, in a first step, the experimentally available range of the VMI voltages is considered. The simulation result is depicted in Fig. 6.3. For this simulation the initial energy of electrons is taken as 70 eV, the THz field strength is taken as 10 MV/m and for each value of V_R the respective energy calibration is taken into account. For better statistics here trajectories of 10000 electrons are taken into account.

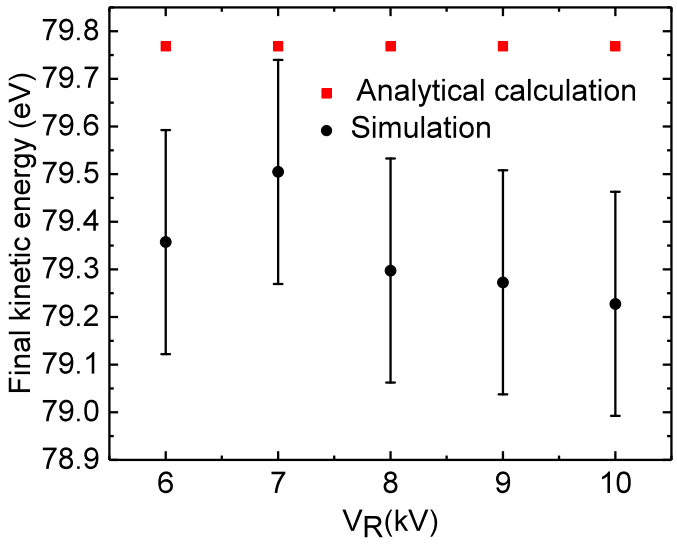

Figure 6.3: Simulated and calculated electron final kinetic energy as a function of typical VMI repeller voltage V_R

The final kinetic energy of the electron varies only slightly with the VMI field due to a change of the local field and the mean value of the electron's final kinetic energy stays below the analytical one (obtained from Eq. 2.79). However no particular trend is obvious and the variation is below 1 eV that is below minimum resolvable energy (see Sec. 5.2)it can be concluded that measured streaking dynamics is not significantly affected by the VMI DC field in this range of the VMI dc field.

6.1.2 The case of comparable THz and static VMI DC fields

Next step is to investigate the case where THz and DC fields are of comparable strengths. The typical DC field is in the order of some hundreds of kV/m in the case where the THz field strength matches this field no significant streaking is observable.

The developed VMI spectrometer is capable of being used for highly energetic electrons specially if even higher voltages are used. However the question is, when the magnitude of the DC field matches the magnitude of the streaking field if the trajectories of the streaked electrons get influenced by the DC field.

After the validation of the simulations for conventional DC field with typical THz field strengths the rather higher amplitudes of DC field coming from the VMI setup are considered such that the DC field matches the typical THz field. The purpose of this

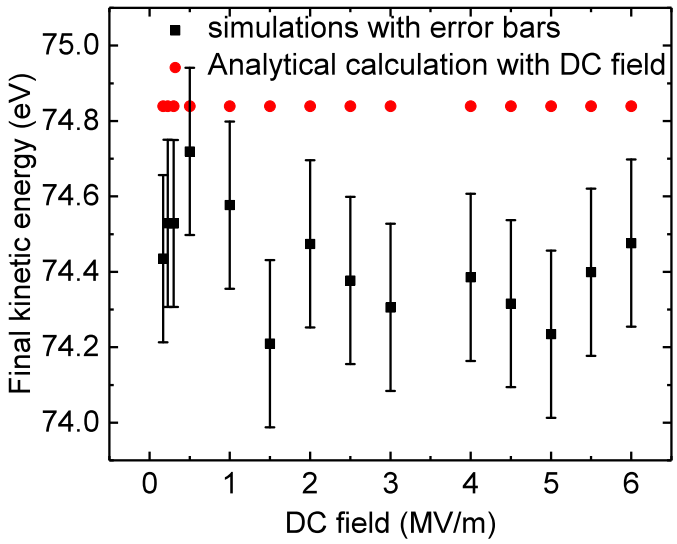

Figure 6.4: Simulated electron final kienetic energy as a function of VMI field comparable to streaking field

simulations is to see the effect of the high DC field on the trajectory of a streaked electron, it is to be figured out if the momentum consideration is enough to exploit the electron dynamics or at some point the individual electron's trajectory needs to be considered. For electrons with an initial energy of 70 eV and a THz field strength of 5 MV/m the variation of the final electron kinetic energy with the VMI DC field is depicted in Fig. 6.4. Here also trajectories of 10000 electrons are considered. For comparison again the calculated value based on Eq. 2.79 with no dc field consideration ismarked with red dots. The simulated values stays below the expected value. The variation does not show any trend however it is in the range well below the resolution of the VMI. Hence it can be concluded that the developed VMI spectrometer is also suited for studying the dynamics of highly energetic electrons.

6.1.3 Effect of the signal to noise ratio

The Signal to Noise Ratio (SNR) plays a crucial role in imaging spectroscopy. A lower SNR hinders the resolution and hence makes the extraction of valuable information from an image challenging. Considering this the influence of the SNR on the possibility of observing streaking phenomena with the collinear VMI spectrometer is simulated.

Referring to Eq. 2.79 the amount of streaking an electron of certain energy experiences depends on the phase of the THz field at the time of electron creation. In order to simulate the complete waveform of the THz field the phase of the field is varied in steps of $\pi/4$ between 0 and 2π. The position of the blobs on the detector generated by streaked electrons changes accordingly. The number of electron trajectories is varied to investigate the influence of SNR. For this simulations the initial electron energy is assumed to be 70 eV, the maximum THz field strength is taken as 0.6 MV/m and V_R is set to 6000 V. A rather small field strength is considered to investigate the possibility of observing streak-

ing with weak field. Moreover the THz-field strength is based on the initial estimation of the field strength present at the interaction point. V_R is taken as 6000 Volts to give the better resolutions. Experimentally the SNR at this V_R is worse. Moreover the particles are assumed to fly within a cone of 20°around the polarization axis to have the maximum streaking. The outcome of the simulation is depicted in Fig. 6.5 where the position of the vertex point of the electron's signal as a function of time delay between the THz and the XUV pulses is plotted. No inverse Abel inversion is applied due to rather low SNR.

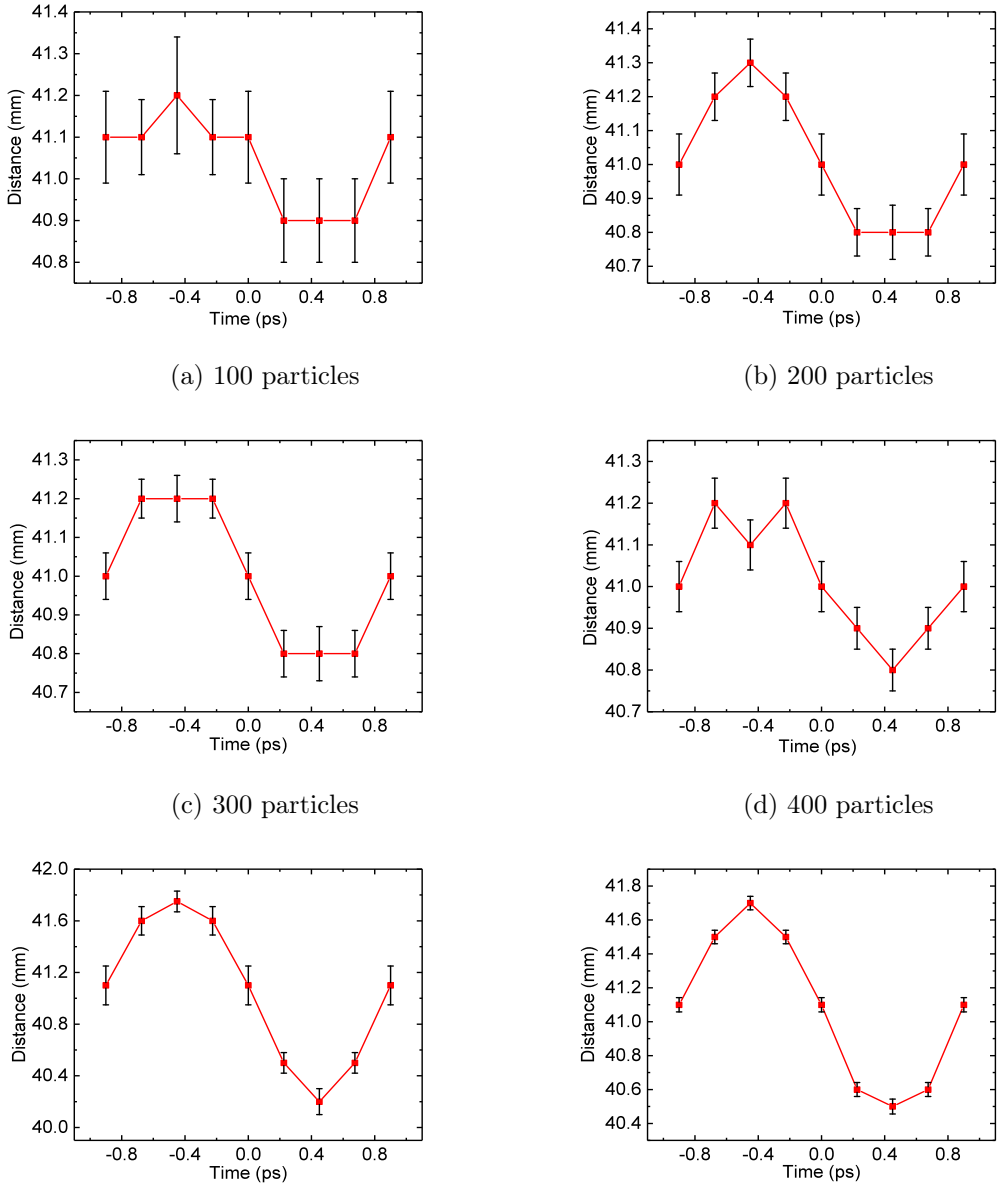

(a) 100 particles

(b) 200 particles

(c) 300 particles

(d) 400 particles

(e) 500 particles

(f) 600 particles

Figure 6.5: The variation of precision with SNR and its effect on the visibility of the streaking effect. The plots shown correspond to 100, 200, 300, 400, 500 and 600 particles flying in a cone of 20°around polarization axis.

It is obvious that with increasing SNR the visibility of the streaking effect is improving. For 100 particles the streaking effect is hard to be observed under these settings. The visibility will increase with higher streaking field strength and SNR. However, if V_R is increased to improve the SNR the resolution gets worse in particular for slow electrons. For this simulation it can be concluded that for a streaking field strength of 0.6 MV/m the minimum number of electrons to be collected in a range of 20% around the polarization axis should be above 150.

6.2 Proof of principle experiment

For the purpose of electron streaking both, XUV and THz beam are spatially and temporally overlapped in a gas target. In the present work xenon is used as the target in order to obtain a high count rate for the momentum maps to be measured. This is critical, as a laboratory based XUV source is used and in order to extract the desired parameters a high SNR is a prerequisite. Using xenon a count rate of upto 20 counts per shot is achieved due to the rather high cross section of the 4d state caused by a shape resonance around 100 eV [127].

In the presence of the THz pulse the electron signal on the detector oscillates along the polarization axis of the THz-field. The amount of oscillation depends on the THz-field strength. As the change of momentum is linearly related to the streaking field and the momentum is linearly mapped onto a radius at the detector the same amount of streaking is observed for electrons with different energies detected at different radial distances from the detector center. The two dimensional momentum map can be converted to a one dimensional energy axis, applying the POP image inversion, to find out the kinetic energy dependence of streaking.

The streaking effect as observed in the experiment is shown in Fig. 6.6 where the shift of the electron signal is depicted in arbitrary units in dependence of the XUV-THz-delay.

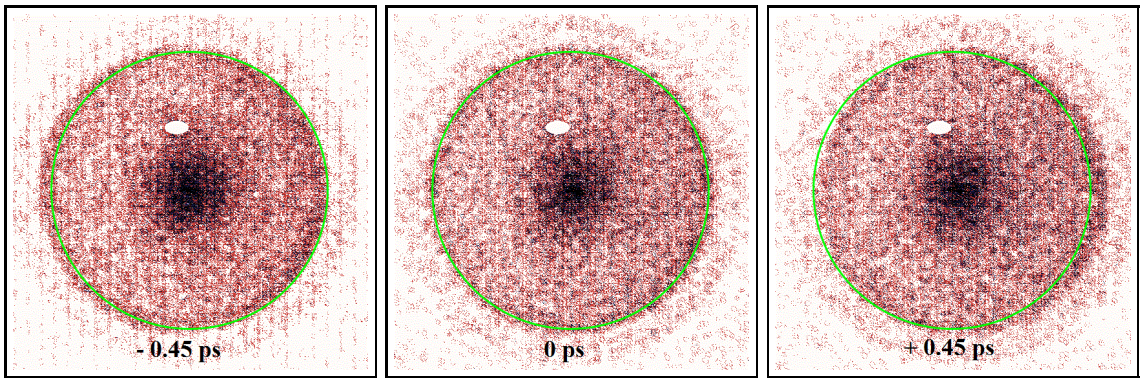

Figure 6.6: Electron momentum map as the THz pulse overlaps with the XUV pulse. The shift of the electron signal along the horizontal polarization axis is clearly visible.

For the purpose of analysing the spectrum the POP code is modified such that the image is cut into two halves perpendicular to the polarization axis. Both parts are inverted separately and afterwards are combined together. The streaking trace obtained from this analysis for electrons going parallel and opposite to the to the THz field are shown in Fig. 6.7. Where the bright line around 23 eV corresponds to the 4d doublet and the less

intense line around 32 eV corresponds to Auger electrons. The shift of the signal due to streaking is obvious.

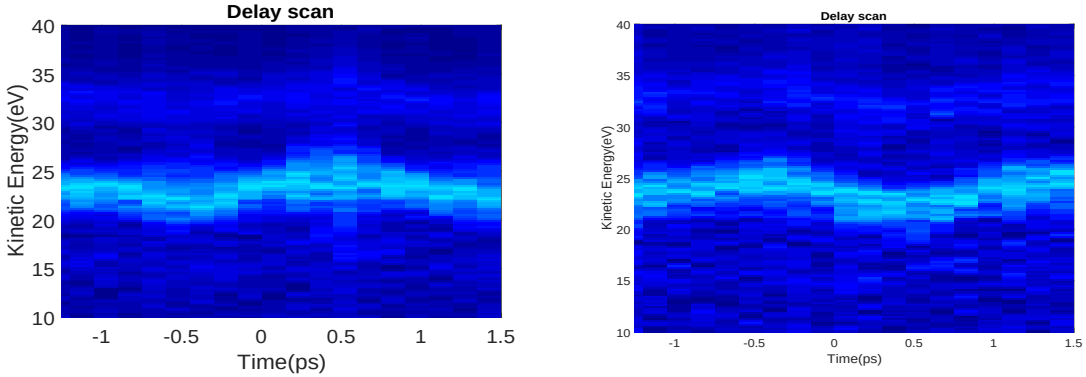

(a) (b)

Figure 6.7: The streaking trace delay scan for a. acceleration(right hand side of VMI) direction, b. deacceleration(left hand side of VMI)

6.2.1 Extraction of XUV-pulse parameters

For the extraction of the XUV pulse parameters the behaviour of the spectrum at the zero crossing of the THz electric field has to be examined. As discussed in Sec. 2.6.2 streaking causes the broadening of the spectrum at this point in time. The spectra for electrons ejected parallel and opposite to the THz field at this time delay are depicted in Fig. 6.8.

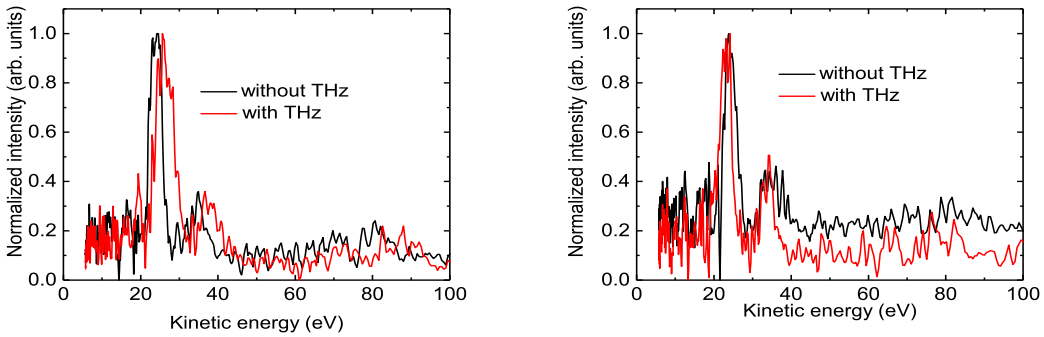

(a) (b)

Figure 6.8: The xenon spectrum with and without THz field. a. For electrons detected going parallel to the THz field. b. for electron going opposite to the THz field

In order to estimate the broadening introduced by streaking Gaussian fit is applied to the 4d-doublet. For the direction parallel to the THz field (this the right hand side for momentum maps given in in Fig. 6.6 the FWHM corresponding to the unstreaked and streaked spectra are 1.43 eV and 2.34 eV respectively. Whereas for the electrons detected on the left hand side the corresponding FWHM are 1.31 eV and 1.54 eV. Using $\Delta\sigma_{\pm}^2 = \sigma_{st}^2 - \sigma_0^2$ the broadenings $\Delta\sigma_{\pm}$ are 1.85 eV and 0.81 eV respectively. The measured streaking speed from Fig. 6.7 is 15± 6 meV/fs. Using these numbers the pulse duration of the XUV pulse is

calculated using Eq. 2.81 as 94.8± 7 fs. The effect of the Gouy phase can not be neglected due to tight focusing. The focus spot is estimated to have a FWHM of 0.7 mm. In order to estimate the influence of the Guoy phase quantitatively we can use the following approach suggested in [101]. For estimating the interaction length one can consider the distance between the gas nozzle and the XUV beam which is approximated to be 0.4 mm in our case. The Rayleigh length for the given spot size is around 5.3 mm. Hence the phase shift can be calculated using $\phi(z) = \tan^{-1}(z/z_R)$ and it is 8.5°. The shift in time applicable for a streaking experiment can then be calculated from $\Delta t = \phi(z)$ T/360°. Taking the period $T = 1.6$ ps the time shift is found to be 37.8± 3 fs. Deconvolving the estimated pulse duration with the time shift the final estimation is 87 ± 10 fs. This is a rather higher number as compared to the expected value of less than 40 fs which is the pulse duration of pump laser. Pulse duration measured for this source in other work [108] where TOF spectrometer is used and the streaking strength was measured to be up to 37 meV/fs is 41.4 ± 5.2 fs. The difference is due to the low energy resolution of the VMI spectrometer and the low streaking speed. A higher field strength and hence a higher streaking speed is required to measure the pulse duration accurately.

6.2.2 Extraction of THz field parameters from the streaking trace

The electron streaking can not only yield information about the pulse parameters of the XUV pulse but also about the properties of the THz pulse. The electron momentum directly maps the THz vector potential and a time derivation of the vector potential gives the THz electric field. A comparison between EOS and streaking can be drawn by matching the extracted numbers for the THz field strength. The streaking technique is somewhat superior to EOS in the sense that no crystal is involved which imposes limitations like saturation and/or dispersion.

The THz vector potential can be derived by plotting the shift of the electron momentum map as a function of delay. For the present experiment this is shown in Fig. 6.9. From this plot a maximum value for the vector potential of

$$A_{max} = 2.7\,\mathrm{x}\,10^{-6}\mathrm{Vs/m} \tag{6.1}$$

can be deduced. Taking the time derivative of the vector potential gives the THz electric field as shown in Fig. 6.10. Here, the maximum amplitude of the THz electric field extracted from streaking is 5.5 MV/m. If compared to the field strength expected from the pulse energy and focus size using the following formula

$$E_{max} = \sqrt{\frac{2I}{c\epsilon_0}} \tag{6.2}$$

where c is speed of light, ϵ_0 is the permittivity of free space and $I = \dfrac{E_{pulse}}{A\tau_{THz}}$ is the maximum intensity with E_{pulse} the pulse energy, A the area of the focus and τ_{THz} the pulse duration of THz-radiation. Taking E_{pulse} equal to 320 nJ, A equal to 1.5 mm^2 and pulse duration of 900 fs the field strength is 13 MV/m. Comparing the values of field strength achieved from streaking and energy and focus size it is found that streaking yields a much smaller value. The possible reasons are possible overestimation of pulse energy or likewise underestimation of focus size. Moreover the calibration used for pulse energy can also be questioned.

If the shape of the waveform attained through EOS and streaking are compared, it is obvious that a more balanced signal (same amplitude in positive and negative directions)

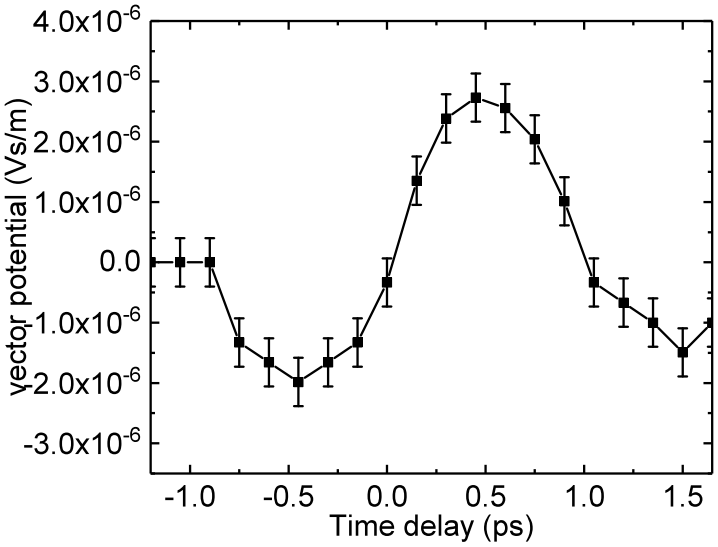

Figure 6.9: The extracted vector potential for the THz mapped by plotting the shift of the electron momentum map as a function of delay

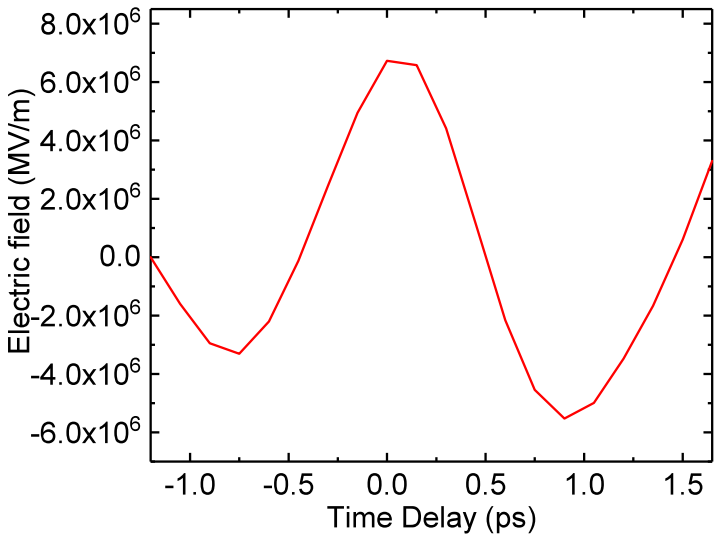

Figure 6.10: The electric field of the THz pulse inferred by calculating the derivative of the vector potential.

is achieved in the case of streaking. One argument supporting this behaviour can be a different Guoy phase, that is the phase of the THz pulse changes while travelling through the focus as observed in the Ph D works [83, 108]. Moreover the spectrum of the THz-radiation can also be extracted by taking the Fourier transform of the electric field transient. It is depicted in Fig. 6.11. The central frequency here also is 0.66 THz as for the spectrum extracted from EOS, however due to a shorter time window the absorption dips observed in the spectrum from EOS are not visible in the spectrum from streaking.

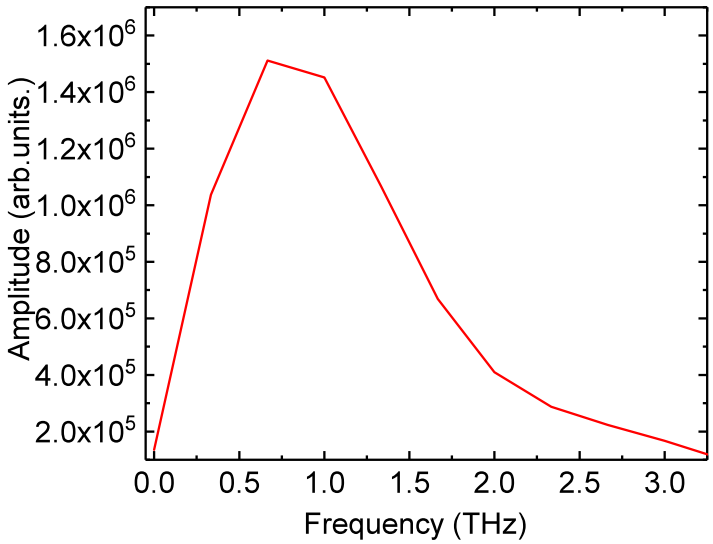

Figure 6.11: The spectrum of the THz pulse extracted from the streaking measurment.

Chapter 7

Conclusion and outlook

The project has demonstrated the first proof of principle experiment of a THz streak camera based on a collinear VMI spectrometer. The collinear geometry used for the VMI spectrometer has been implemented for the first time, to our knowledge, and it offers significant advantages over the non-collinear geometry, especially the freedom of rotating the linear polarization to any transversal orientation.

As for the HHG source the photon flux for one of the best output of the HHG source is measured giving a energy conversion efficiency upto 9.45 x 10^{-9}.implementation of pulse compression using HFC is implemented however the expected compression factor of 4 is not confirmed in the pulse duration measurement. In order to figure out where exactly the problem is an independent measurement of the pulse length should be carried out in the best case directly before the HHG target in order to investigate the actual achieved pulse compression and possible chirping of the pulse along the beam path.

A THz source with a conversion efficiency upto 0.13% is implemented. The efficiency of the source can be enhanced upto an order of magnitude by cooling the crystal in order to decrease the re-absorption of the THz-radiation inside the generation crystal [128]. Although the beam propagates about 2.5 m in air the absorption estimated from the spectrum measured at the experiment is found be only 20%. It is important to have a better calibration of the pulse energy measurement using pyro detector in order to minimize the discrepancy in the field strength estimation via pulse energy and streaking.

A VMI spectrometer with dc field parallel to the electron propagation is successfully commissioned. With the successful implementation of the blob analysis protocol energy resolution of 4% for 70 eV electron is accomplished which is found to be close to the simulated value of 3%. Moreover with the use of a transversely inserted gas nozzle the use of higher target densities is made possible. The simulation based on DSMC program suggest that a backing pressure of 10^{-4} mbar in the experimental chamber will give a target density of upto 3 x 10^{22} /m^3 for neon. This is particularly important for studies targeted at the electron interaction with other atoms around it the so called interaction with bath.

The detection efficiency of the used high efficient detector is calculated and found to be a factor of 1.6 better than the conventional MCP + phosphor imaging detector. Which makes this setup highly suitable for weak light sources with low photon flux. A count rate of up to 20 counts per shot is achieved for xenon.

The VMI spectrometer part of the setup has been simulated in SIMION. In particular the effect of the DC VMI electric field on the streaked electrons has been investigated because of the special design of the setup for comparable field strengths of THz and VMI fields.

It is found that the DC field does not influence the streaking phenomenon significantly and the setup can be successfully used for highly energetic electrons.

The pulse duration of the XUV pulse is estimated to be 86.7 $\pm$10 fs. Which is about a factor of 2 worse than the expected value of 40 fs, if the pulse duration of only the laser is considered and the influence of the HFC is not taken into account. By improving the VMI resolution and the field strength at the interaction point the time resolution can be enhanced to make the setup a suitable candidate for time-resolved studies at femtosecond time scales; this work has provided the first working example with this purpose.

This experiment opens up plenty of possibilities for future measurements. The setup can be used for studies of effects like PCI including a full momentum map of the generated electrons.

The VMI spectrometer also offers the possibility of observing the influence of variable polarization and can be used for polarization-dependent studies. A rotation of a linear polarization does not requires any modification of the setup.

The setup can be used for multidimensional angular THz-streaking with a circularly-polarized THz beam. The idea is taken from the attosecond metrology [129] where a reaction microscope is used to measure the angular momentum offset as a result of a delay between the electron's exit and the maximum of external electric field. In our scenario the rotating polarization of the THz beam is strong enough to deflect the electron in the radial spatial direction. With the spatial resolution provided by the VMI spectroscopy the time of electron creation is then mapped to the final angle of momentum vector in the plane of polarization. this offset of electron signal can be measured to reveal information on the time difference between the maximum of THz field and the creation of electron. This arrangment can be used to study interfernce effects as suggested in [130].

Appendices

Appendix A

VMI image inversion Algorithms

The mathematical formalism of iterative and Polar onion peeling inversion codes is given.

A.1 Vrakking inversion

The rings appearing on the detector in a VMI experiment are due to accumulation of electrons ejected perpendicular to the detector axis. For these electrons the detected position varies only very slowly with the azimuthal angle φ, see Fig. A.1. Therefore the detected image can be considered as a slice through the 3D velocity and angular distribution perpendicular to the detector axis. This assumption is the basis of this iterative procedure. The 3D velocity and angular distribution can be written as a product of a velocity distribution and a velocity dependent angular distribution as

$$P(v_x, v_y, v_z) = P(v, \theta, \varphi) = P_1(v)P_2(v, \theta), \tag{A.1}$$

where the fact is utilized that in the experiment there exists a cylindrical symmetry and therefore there is no dependence on the azimuthal angle φ. This symmetry axis is the axis of polarization of the laser, in our case it is the the x-axis, whereas the z-axis is the detector axis and the y-axis is the axis perpendicular to the symmetry axis in the VMI image as shown in the Fig. A.1. The polar angle θ represents the angle between the velocity vector of the ejected particle and the positive (x>0) part of the symmetry axis. Generally the limits for this angle are from 0 to π. However, to account for the fact that the upper (y>0) and lower (y<0) part of an experimental image represent two independent measurements for the same velocity and angular distribution, which can be individually analyzed and then compared, we consider that θ varies from 0 to π for y >0, and from π to 2π for y<0. The normalization of the 3D-distribution reads

$$2\pi \int\int P_1(v)v^2 P_2(v, \theta) sin\theta d\theta dv = 1. \tag{A.2}$$

Similar to the 3D velocity and angular distribution, the 2D experimental image can be written as the product of a radial distribution $Q_{1,exp}(R)$ and a radially dependent angular distribution $Q_{2,exp}(R, \alpha)$:

$$Q_{exp}(x, y) = Q_{exp}(R, \alpha) = Q_{1,exp}(R) * Q_{2,exp}(R, \alpha), \tag{A.3}$$

and the normalization of the 2D image implies that

$$\int\int Q_{1,exp}(R) * Q_{2,exp}(R, \alpha) d\alpha dR = 1. \tag{A.4}$$

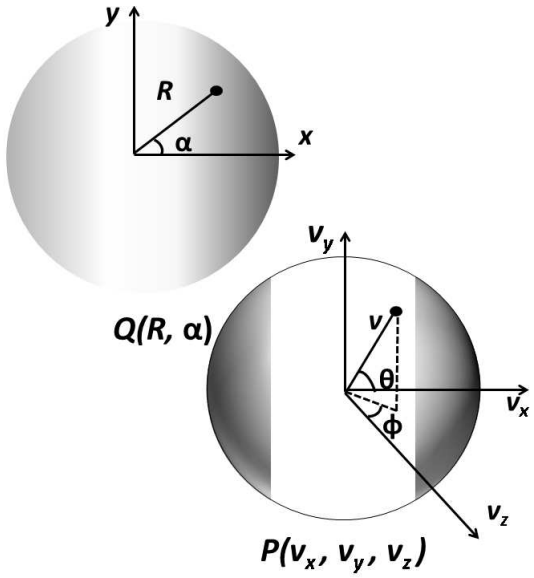

Figure A.1: Depiction of the co-ordinate system for VMI image inversion through an iteration code. The 3D velocity and angualar distribution is $P(v_x, v_y, v_z)$, and the $Q(R, \alpha)$ is the measured 2D radial and angular distribution.

Here α varies from 0 to π for y >0, and from π to 2π for y<0. Now $Q_{1,exp}(R)$ and $Q_{2,exp}(R, \alpha)$ are used to estimate and iteratively correct $P_1(\upsilon)$ and $P_2(\upsilon, \theta)$. The ansatz used for this purpose is given by

$$P_{1,i=0}(\upsilon) = Q_{1,exp}(R)/2\pi R \quad \text{and} \tag{A.5}$$

$$P_{2,i=0}(\upsilon, \theta) = Q_{2,exp}(R, \alpha = \theta) \tag{A.6}$$

where i is the iteration index. The radius R and velocity υ are related through $R = s_0 \upsilon t$. Where s_0 is a constant which depends on the electric field geometry and is close to unity. Using this ansatz a 2D image is calculated from which a new 2D radial and angular distribution $Q_{1,i=0}(R) * Q_{2,i=0}(R, \alpha)$ can be extracted. Then an iterative procedure is carried out where a calculated 2D radial and angular distribution $Q_{1,i}(R) * Q_{2,i}(R, \alpha)$ is compared with the experimental 2D radial and angular distribution $Q_{1,exp}(R) * Q_{2,exp}(R, \alpha)$ and based on the differences found in the experimental and calculated distribution - corrections are applied to the 3D velocity and angular distribution following the relations

$$P_{1,i}(\upsilon) = P_{1,i-1}(\upsilon) - c_1[Q_{1,i-1}(R) - Q_{1,exp}(R)]/2\pi R \quad \text{and} \tag{A.7}$$

$$P_{2,i}(\upsilon, \theta) = P_{2,i-1}(\upsilon, \theta) - c_2[Q_{2,i-1}(R, \alpha = \theta) - Q_{2,exp}(R, \alpha = \theta)]. \tag{A.8}$$

The parameters c_1 and c_2 determine the amount of correction applied to the 3D velocity and angular distribution. Typically it is assumed that $c_1 = 2.0$ and $c_2 = 1.0$ to achieve a convergence in a reasonable number of iterations. As in an experiment a positive number of particles gives a meaningful image the negative values of $P_{1,i}(\upsilon)$ and $P_{2,i}(\upsilon, \theta)$ are set to zero. In this method an acceptable level of convergence is achieved in about 10-20 iterations.

A.2 Polar onion peeling

Considering the linear polarization of the laser the electron 3D radial distribution function $f(r, \theta, \phi)$ is cylindrically symmetric around the x-axis, as shown in Fig. A.2. In velocity map imaging, $f(r, \theta, \phi)$ is mapped onto the 2D plane parallel to x-axis, producing the measured distribution $Q(R, \alpha)$. For electrons emitted with a certain kinetic energy, a radial distribution described by a delta function $\delta(r)$, the image $Q(R, \alpha)$ has also signal at radii smaller than the radius defined by the velocity of the electrons that is at $R < r$. The origin of this signal is the ϕ-dependence of the electron cloud, which may be calculated and subtracted from $Q(R, \alpha)$ for all $R < r$ leaving only the radial delta function $\delta(r)$ at $R = r$. The resultant distribution is then equivalent to a slice through 3D-distribution $f(r, \theta, \phi = 0)$ and from this the full 3D distribution can be recovered because of the cylindrical symmetry around the x-axis of $f(r, \theta, \phi)$.

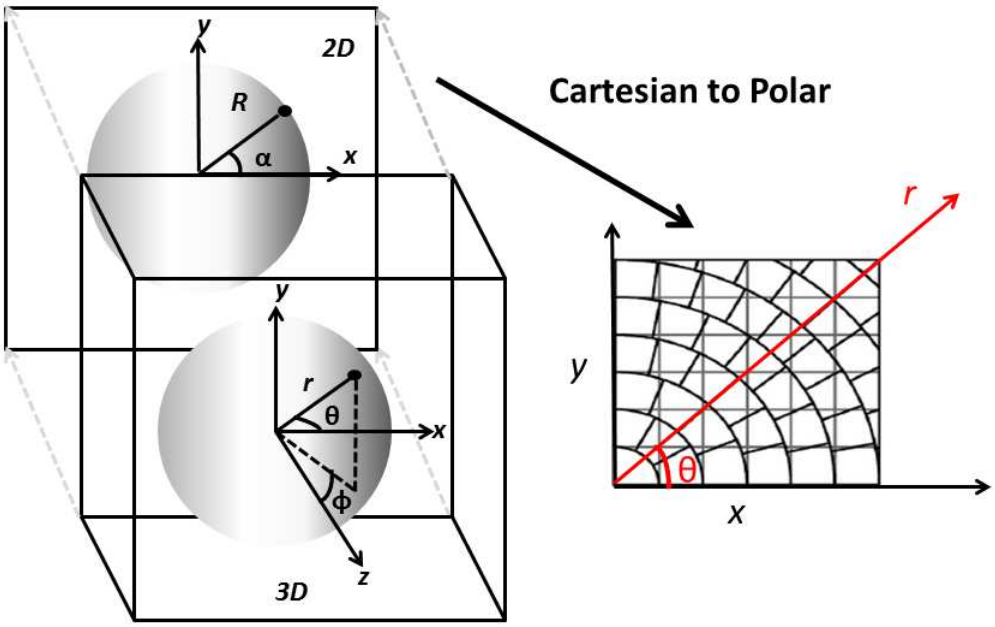

Figure A.2: Projection of a 3D sphere onto a 2D plane and conversion from Cartesian pixels to Polar pixels.

For broad radial distributions with signals at different radii, the 2D projection $Q(R, \alpha)$ can be expressed as the sum of the individual 2D projections $q(r; R, \alpha)$ for all r components of the full 3D distribution $f(r, \theta, \phi)$

$$Q(R, \alpha) = \int_0^{r_{max}} q(r; R, \alpha) dr, \tag{A.9}$$

where $R \leq r$ and the semicolon denotes that the 2D projections are given at specific radii r. Similar to the case of the radial delta function, $f(r, \theta, \phi = 0)$ can be recovered by removing the contributions of ϕ for $R < r$, starting at $r = r_{max}$ and incrementally decreasing in steps of dr until $r = 0$ is reached. At each r , $q(r; R, \alpha)$ is subtracted from $Q(R, \alpha)$, which in turn peels the ϕ-contributions at each r.

Conversion of Cartesian to Polar pixels is done by mapping the camera pixel array onto a polar array. The signal in one single polar pixel is calculated by rotating it by α about

its pivot. Its fractional overlap with the four close by Cartesian pixels and their respective signal intensity is then used to define the polar pixel's intensity. The resulting raw polar image $Q(R, \alpha)$ is then a triangular array because the number of angles α at which pixels can be defined scales linearly with R. From this polar image one can simply read off the radial distribution along the R-axis and the angular distribution by comparing the signal levels along the angular axis.

This image $Q(R, \alpha)$ is the sum over all r components as given by Eq. A.9. For the case where there is no signal at radii larger than the detector, the outermost ring contains no contribution from ϕ and the substitution

$$q(r; R, \alpha) = h(r, \theta), \tag{A.10}$$

at $r = R$ is valid. Starting at the outermost radius, $h(r, \theta)$ is fitted to the well known angular distribution

$$I(r, \theta) = N(r) \sum_{n}^{n_{max}} \beta_n(r) P_n[cos(\theta)], \tag{A.11}$$

where $P_n[cos(\theta)]$ is the n^{th} order Legendre polynomial, $N(r)$ is an intensity factor and β_n is the anisotropy parameter. The integer n depends on the physics of the process just that $n_{max} = 2$ for single photon processes and $n_{max} = 4$ for double photon processes. The Legendre polynomials are used as the angular distribution of electrons can be described by these polynomials(as discussed in section.2.4). From $N(r)$ and β_n the distribution $q_{fit}(r_{max}; R, \alpha)$ is calculated which is then subtracted from $Q(R, \alpha)$ for all $R \leq r_{max}$ such that

$$Q^{\dagger}(R, \alpha) = Q(R, \alpha) - q_{fit}(r_{max}; R, \alpha). \tag{A.12}$$

Now $Q^{\dagger}(R, \alpha)$ is a modified image containing $Q(R, \alpha)$ for $R < r_{max}$. The process is incrementally repeated for $r = r_{max} - dr$ until $r = 0$ is reached. Finally $Q^{\dagger}(R, \alpha)$ is a 2D-image of all residuals from the subtraction. The 2D slice $f(r, \theta, \phi = 0)$ is constructed by using Eq. A.10 at each increment.

In order to calculate $q_{fit}(r_{max}; R, \alpha)$ in a robust way, basis functions are used to fit the experimental 2D data. The basis functions are the idealized radial distribution functions $b_r(R)$ produced by angular integration of perfectly isotropic images. To relate it with the experimental image the basis functions are generated by simulating images at a given r onto a Cartesian grid, transforming to the polar form and integrating over angle α. The basis set $B(r, R)$ is generated from basis functions at all possible r, and $B(r, R)$ is consequently a 2D triangular array. All basis functions are normalized such that the intensity at $r = R$ is unity. $B(r, R)$ is constructed once using a stand alone program and then supplied to the reconstruction routine. The size of $B(r, R)$ is determined by the size of the imaging device in terms of pixels. During the POP routine the relevant basis function $b_r(R)$ is retrieved from the $B(r, R)$ basis set. An idealized perfectly isotropic polar image $g_{ideal}(r; R, \alpha)$ is then constructed from $b_r(R)$ using

$$q_{ideal}(r; R, \alpha) = \rho(r, R) b_r(R), \tag{A.13}$$

where $\rho(r, R)$ is the ratio of the number of polar pixels at r to R and accounts for the fact that the number of polar pixels changes with respect to R that is the polar image is a 2D triangular array. The idealized image $q_{fit}(r; R, \alpha)$ with experimentally observed anisotropy

and intensity is then generated through

$$q_{fit}(r;R,\alpha) = q_{ideal}(r;R,\alpha)N(r)\sum_{n}\beta_n(r)P_n[\frac{R}{r}cos(\alpha)], \tag{A.14}$$

where the parameters $N(r)$ and $\beta_n(r)$ have been obtained from the fitting of the outer ring $h(r,\theta)$ to the Eq. A.11, the factor R/r accounts for the transformation of the coordinate system from r,, θ and ϕ to R and α.

Acknowledgement

I am in debt of paying thanks to many people who have been a great support in course of this project.

First of all I am grateful to Prof. Dr. Markus Drescher for giving me the opportunity to work under his precious supervision. I am truly humbled by the confidence and assurance he gave me during our discussions. I felt he kept believing in me also in the times when I was not believing in myself.

Next I would like to thank Prof. Dr. Ulrike Früling for her continuous guidances. She was always there to answer my question.

I am grateful to Prof. Dr. Kobashnik for his valuable discussion on simulations of THz streaking observed with VMI. His precious input helped me a lot to perform the simulations in the right direction.

A big thanks to Prof. Dr. David Parker for his advice regarding the improvement of detector performance.

I am also thankful to Prof. Dr. Per Johnson for his valuable discussion which helped me a lot to clarify my understanding for the concepts regarding VMI.

A big thanks goes to Dr. Marek wieland who helped me not only with all experimental challenges but was a helping hand for administrative problems. His kindness and dedication was a great source of inspiration of me. It will not be wrong to say I could not get to this point without his continuous encouragement.

Dr. Armin Azima had been the person showing most concern to my success. He had been a great moral support in the times of challenging situations in the experiment. I have no words to thanks him for the incidence when he even considered taking my children with him so that I could finish my measurement.

Thanks to Oliver Becker who had been a big help for me specially for making the solid-edge drawings acceptable for the mechanical workshop. I am thankful for all his logistic support.

I am grateful to Dr. Roman Branaath for being a great support for the harmonic source used in the project.

I would like to thank Khatharina Wenig, Arne Baumann, Oliver Schepp, Martin Ranke, Anastosos, Stefan Wiegand, Masud Raufi and Yannic Ristau for their support in one way or other.

I am grateful to Mr. Flieg and other members of mechanical workshop for delivering the mechanical part on time.

I am humbly thankful to my family for their moral support. A big thanks to my husband who supported me completely so that I can finish this work. I am thankful to my children Faiq(6) and Mishel(4) who have seen their mother not so much during the days of experimental work.

Bibliography

[1] M. Drescher, M. Hentschel, R. Kienberger, G. Tempea, C. Spielmann, G. A. Reider, P. B. Corkum, and F. Krausz, "X-ray pulses approaching the attosecond frontier," *science 291, 1923*, 2001.

[2] F. E. Lytle, R. M. Parrish, and W. T. Barnes, "An introduction to time-resolved pump/probe spectroscopy," *Appl. Spectrosc. 39, 444*, 1985.

[3] S. Hüfner, *Photoelectron spectroscopy Principles and applications.* Springer-Verlag Berlin Heidelberg GmbH, 2003.

[4] B. Fain, S. H. Lin, and V. Khidekel, "Limitations of pump-probe femtosecond time-resolved experiments: Time-dependent absorption and dispersion line shapes," *Phys. Rev. A. 47, 3222*, 1993.

[5] M. M. Murnane, H. C. Kapteyn, M. D. Rosen, and R. W. Falcone, "Ultrafast x-ray pulses from laser-produced plasmas," *Science 251, 531*, 1991.

[6] D. H. Auston, "Picosecond optoelectronic switching and gating in silicon," *Appl. Phys. Lett. 26, 101*, 1975.

[7] A. McPherson, G. Gibson, H. Jara, U. Johann, T. S. Luk, I. A. McIntyre, K. Boyer, and C. K. Rhodes, "Studies of multiphoton production of vacuum-ultraviolet radiation in the rare gases," *J. Opt. Soc. Am. B. 4, 595*, 1987.

[8] A. S. E Constant, V D. Taranukhin and P. B. Corkum, "Methods for the measurement of the duration of high-harmonic pulses," *Phys. Rev. A. 56, 3870*, 1997.

[9] J. M. Schins, P. Breger, P. Agostini, R. C. Constantinescu, H. G. Muller, A. Bouhal, G. Grillon, A. Antonetti, and A. Mysyrowicz, "Cross-correlation measurements of femtosecond extreme-ultraviolet high-order harmonics," *J. Opt. Soc. Am. B 13, 197*, 1996.

[10] E. S. Toma, H. G. Muller, P. M. Paul, P. Breger, M. Cheret, P. Agostini, C. L. Blanc, G. Mullot, and G. Cheriaux, "Ponderomotive streaking of the ionization potential as a method for measuring pulse durations in the xuv domain with fs resolution," *Phys. Rev. A, Volume 62, 061801*, 2000.

[11] F. Quere, Y. Mairesse, and J. Itatani, "Temporal characterization of attosecond xuv fields," *Journal of Modern Optics, 52, 339*, 2005.

[12] R. Kienberger, M. Hentschel, M. Uiberacker, C. Spielmann, M. Kitzler, A. Scrinzi, M. Wieland, T. Westerwalbesloh, U. Kleineberg, U. Heinzmann, M. Drescher, and F. Krausz, "Steering attosecond electron wave packets with light," *Science 297, 1144*, 2002.

[13] M. Uiberacker, E. Goulielmakis, R. Kienberger, A. Baltuska, T. Westerwalbesloh, U. Keineberg, U. Heinzmann, M. Drescher, and F. Krausz, "Attosecond metrology with controlled light waveforms," *Laser Physics. 15,195*, 2005.

[14] J. Gagnon and V. S. Yakovlev, "The robustness of attosecond streaking measurements," *OPTICS EXPRESS. 17, 17678*, 2009.

[15] R. Kienberger, E. Goulielmakis, M. Uiberacker, A. Baltuska, V. Yakovlev, F. Bammer, A. Scrinzi, T. Westerwalbesloh, U. Kleineberg, U. Heinzmann, M. Drescher, and F. Krausz, "Atomic transient recorder," *Nature 427, 817*, 2004.

[16] P. P Eckle, M. Smolarski, P. Schlup, J. Biegert, A. Staudte, M. Schöffler, H. G. Muller, R. Dörner, and U. Keller, "Attosecond angular streaking," *Nat. Phys. 4, 565*, 2008.

[17] K. Varju, P. Johnsson, J. Mauritsson, T. Remetter, T. Ruchon, Y. Ni, F. Lepine, M. Kling, J. Khan, K. J. chafer, M. J. J. Vrakking, and A. L'Huillier, "Angularly resolved electron wave packet interferences," *J. Phys. B: At. Mol. Opt. Phys. 39 (2006) 3983–3991*, 2006.

[18] S. Zherebtsov, A. Wirth, T. Uphues, I. Znakovskaya, O. Herrwerth, J. Gagnon, M. Korbman, V. S. Yakovlev, M. J. J. Vrakking, M. Drescher, and M. F. Kling, "Attosecond imaging of xuv-induced atomic photoemission and auger decay in strong laser fields," *J. Phys. B: at. Mol. Opt. Phys. 44, 105601*, vol. 44, p. 105601, 2011.

[19] B. Schütte, S. Bauch, U. Frühling, M. Wieland, M. Gensch, E. Plönjes, T. Gaumnitz, A. Azima, M. Bonitz, and M. Drescher, "Evidence for chirped auger-electron emission," *Phys. Rev. Lett. 108, 253003*, 2012.

[20] U. Frühling, "Light field streaking for fels," *J. Phys. B: At. Mol. Opt. Phys. 44, 243001*, 2011.

[21] O. Ghafur, W. Siu, P. Johnsson, M. F. Kling, M. Drescher, and M. J. J. Vrakking, "A velocity map imaging detector with an integrated gas injection system," *Rev. Sci. Inst. 80, 033110*, 2009.

[22] A. J. B. Eppink and D. H. Parker, "Velocity map imaging of ions and electrons using electrostatic lenses: Application in photoelectron and photofragment ion imaging of molecular oxygen," *Rev. Sci. Inst. 68, 3477 (1997);*, 1997.

[23] D. H. Parker and A. J. B. Eppink, *IMAGING IN MOLECULAR DYNAMICS*, ch. Velocity map imaging: applications in molecular dynamics and experimental aspects, pp. 20 – 64. cambridge University Press, 2003.

[24] M. Ryazanov and H. Reisler, "Improved sliced velocity map imaging of h photofragments," *J Chem Phys. 138, 144201*, 2013.

[25] G. Gademann, Y. Huismans, A. Gijsbertsen, J. Jungmann, J. Visschers, and M. J. J. Vrakking, "Velocity map imaging using an in-vacuum pixel detector," *Rev. Sci. Inst. 80, 103105*, 2009.

[26] S. Düsterer, G. Hartmann, F. Babies, A. Beckmann, G. Brenner, J. Buck, L. Costello, J. Dammann, A. De Fanis, P. Geßler, L. Glaser, M. Ilchen, P. Johnsson, A. K. Kazansky, T. J. Kelly, T. Mazza, M. Meyer, V. L. Nosik, I. P. Sazhina, F. Scholz, J. Seltmann, H. Sotoudi, J. Viefhaus, and N. M. Kabachnik, "Angle resolved photoelectron spectroscopy of two-color xuv-nir ionization with polarization control," *J. Phys. B: At. Mol. Opt. Phys. 49, 165003*, 2016.

[27] B. Baguenard, J. B. Wills, F. Pagliarulo, F. Lepine, and B. Climen, "Velocity-map imaging electron spectrometer with time resolution," *Rev. Sci. Instrum. 75, 324*, 2004.

[28] Available at `http://www.lbl.gov/MicroWorlds/ALSTool/EMSpec/EMSpec.html.960105`.

[29] M. Wiedenhoeft, S. E. Canton, A. A. Wills, T. Gorczyca, J. Viefhaus, U. Becker, and N. Berrah, "Coincidence energy and angular distribution in xenon 4d5/2 inner-shell double photoionization," *J. Phys. B: At. Mol. Opt. Phys. 41, 095202*, 2008.

[30] M. Y. Kuchiev and S. A. Sheinerman, "Post-collision interaction in atomic processes," *Usp. Fiz. Nauk 158,353*, 1989.

[31] M. Y. Kuchiev and S. A. Sheinerman, "Resonant processes involving the production of three charged particles," *Zh. Eksp. Teor. Fiz. 90, 1680*, 1986.

[32] K. Miyazaki and H. Sakai, "High-order harmonic generation in rare gases with intense subpicosecond dye laser pulses," *1. Phys. B: At. Mol. Opt. Phys. 25, L83*, 1992.

[33] C. G. Wahlström, J. Larsson, A. Persson, T. Starczewski, and S. Svanberg, "High-order harmonic generation in rare gases with an intense short-pulse laser," *Phys. Rev. A. 48, 4709*, 1993.

[34] J. Zhou, J. Peatross, M. M. Murnane, I. P. Christov, and H. C. Kapteyn, "Enhanced high-harmonic generation using 25 fs laser pulses," *Phys. Rev. Lett. 76, 752*, 1996.

[35] A. L'Huillier and P. Balcou, "High-order harmonic generation in rare gases with a 1-ps 1053-nm laser," *Phys. Rev. Lett. 70, 774*, 1993.

[36] P. B. Corkum, "Plasma perspective on strong field multiphoton ionization," *Phys. Rev. Lett. 71, Number 13, 1994*, 1993.

[37] M. V. Ammosov, N. Delone, and V. P. Krainov, "Tunnel ionization of complex atoms and of atomic ions in an alternating electromagnetic field," *Sov. Phys. JETP 64, 1191*, 1986.

[38] M. F. Kling and M. J. J. Vrakking, "Attosecond electron dynamics," *Annual Rev. Phys. Chem. 59, 463*, 2008.

[39] P. Salieres and I. Christov, *Strong field laser physics*. Springer, 2009.

[40] A. L. Lytle, *Phase matching and coherence of high-order harmonic generation in hollow waveguides.* PhD thesis, University of Colorado, 2008.

[41] M. Mittenzwey, *High Harmonic Generation for the XUV seeding experiment at FLASH.* PhD thesis, University of Hamburg, 2011.

[42] E. Balogh, *Macroscopic study and control of high-order harmonic and attosecond pulse generation in noble gases.* PhD thesis, University of Szeged, 2014.

[43] P. Balcou, P. Sali'eres, A. L'Huillier, and M. Lewenstein, "Generalized phase-matching conditions for high harmonics: The role of field-gradient forces," *Phys. Rev. A 55, 3204*, 1997.

[44] R. H. Stolen and C. Lin, "Self-phase-modulation in silica optical fibers," *Phys. Rev. A. 17, 1448*, 1978.

[45] M. Nisoli, S. De Silvestri, and O. Svelto, "Generation of high energy 10 fs pulses by a new pulse compression technique," *Appl. Phys. Lett. 68, 2793*, 1996.

[46] C. Fourcade Dutin, A. Dubrouil, S. Petit, E. Mevel, E. Constant, and D. Descamps, "Post-compression of high-energy femtosecond pulses using gas ionization," *Optics Letters 35 (Number 2), 253*, 2010.

[47] R. Brannath, "Kompression von pulsen eines femtosekunden-lasersystems in einem nichtlinearen gasmedium," Master's thesis, Universität Hamburg, 2012.

[48] K. P. Auston, D. H. Cheung, J. A. Valdmanis, and D. A. Kleinman, "Cherenkov radiation from femtosecond optical pulses in electro-optic media," *Phys. Rev. Lett. 53, 1555*, 1984.

[49] B. B. Hu, X. C. Zhang, D. H. Auston, and P. R. Smith, "Free-space radiation from electro-optic crystals," *Appl. Phys. Lett. 56, 506*, 1990.

[50] X. C. Zhang, Y. Jin, and X. F. Ma, "Coherent measurement of thz optical rectification from electro-optic crystals," *Appl. Phys. Lett. 61, 2764*, 1992.

[51] L. Xu, X. C. Zhang, and D. H. Auston, "Terahertz beam generation by femtosecond optical pulses in electro-optic materials," *Appl. Phys. Lett. 61, 1784*, 1992.

[52] A. A Nahata, A. S. Weling, and T. F. T F Heinz, "A wideband coherent terahertz spectroscopy system using optical rectification and electro-optic sampling," *Appl. Phys. Lett. 69, 2321*, 1996.

[53] Q. Wu and X.-C. Zhang, "Free-space electro-optics sampling of mid-infrared pulses," *Appl. Phys. Lett. 71, 1285 (1997);*, 1997.

[54] I. Wilke and S. S Sengupta, *Terahertz Spectroscopy: Principles and Applications*, ch. Nonlinear Optical Techniques for Terahertz Pulse Generation and Detection—Optical Rectification and Electrooptic Sampling, pp. 41 – 72. CRC Press, 2007.

[55] A. Tomasino, A. Parisi, S. Stivala, P. Livreri, A. C. Cino, A. Busacca, P. M., and R. Morandotti, "Wideband thz time domain spectroscopy based on optical rectification and electro-optic sampling," *Scientic Report 3, 3116*, 2013.

[56] M. Bass, P. A. Franken, J. F. Ward, and G. Weinreich, "Optical rectification," *Phys. Rev. Lett. 9, 446*, 1962.

[57] Z. Jiang and X. C. Zhang, *Sensing with Terahertz Radiation*. Springer, 2002.

[58] K. Wynne and J. J. Carey, "An integrated description of terahertz generation through optical rectification, charge transfer, and current surge," *Optics Communications 256, 400*, 2005.

[59] D. H. Auston and M. C. Nuss, "Electrooptic generation and detection of femtosecond electrical transients," *IEEE JOURNAL OF QUANTUM ELECTRONICS 24, 184*, 1988.

[60] J. Hebling, A. G. Stepanov, G. Almasi, B. Bartal, and J. Kuhl, "Tunable thz pulse generation by optical rectification of ultrashort laser pulses with tilted pulse fronts," *Appl. Phys. B 78, 593*, 2004.

[61] L. Palfalvi, J. Hebling, J. Kuhl, A. Peter, and K. Polgar, "Temperature dependence of the absorption and refraction of mg-doped congruent and stoichiometric linbo3 in the thz range," *J. Appl. Phys. 97, 123505*, 2005.

[62] X. C. Zhang, X. F. Ma, Y. Jin, T. M. Lu, E. P. Boden, P. D. Phelps, K. R. Stewart, and C. P. Yakymyshyn, "Terahertz optical rectification from a nonlinear organic crystal," *Appl. Phys. Lett. 61, 3080*, 1992.

[63] M. Shalaby, C. Vicario, K. Thirupugalmani, S. Brahadeeswaran, and C. P. Hauri, "Intense thz source based on bna organic crystal pumped at ti:sapphire wavelength," *Optics Lett. 41, 1777*, 2016.

[64] T. P. Dougherty, G. P. Wiederrecht, and K. A. Nelson, "Impulsive stimulated raman scattering experiments in the polariton regime," *J. Opt. Soc. Am. B 9, 2179*, 1992.

[65] K.-L. Yeh, *The generation of high field terahertz radiation and its application in terahertz nonlinear spectroscopy*. PhD thesis, MASSACHUSETTS INSTITUTE OF TECHNOLOGY, USA, 2009.

[66] G. D. Boyd and M. A. Pollack, "Microwave nonlinearities in amsotropic dielectrics and their relation to optical and electro-optical nonlinearities," *Phys. Rev. B. 7, 5345*, 1973.

[67] B. Bartal, I. Z. Kozma, A. G. Stepanov, G. Almasi, J. Kuhl, E. Riedle, and J. Hebling, "Toward generation of microj range sub-ps thz pulses by optical rectification," *Appl. Phys. B 86, 419–423 (2007)*, 2007.

[68] R. L. Sutherland, *Handbook of Nonlinear Optics*. Marcel Dekker, Inc, 2003.

[69] J. Hebling, K. L. Yeh, M. C. Hoffmann, B. Bartal, and K. A. Nelson, "Generation of high-power terahertz pulses by tilted-pulse-front excitation and their application possibilities," *J. Opt. Soc. Am. B 25, B6*, 2008.

[70] D. H. Auston, "Subpicosecond electro-optic shock waves," *Appl. Phys. Lett. 43, 713*, 1983.

[71] J. Hebling, G. Almasi, and I. Z. Kozma, "Velocity matching by pulse front tilting for largearea thz-pulse generation," *OPTICS EXPRESS 10, 1161*, 2002.

[72] I. H. Baek, B. J. Kang, Y. J. Jeong, and F. Rotermund, "Diffraction-limited high-power single-cycle terahertz pulse generation in prism-cut linbo3 for precise terahertz applications," *Journal of the Optical Society of Korea. 18, 60-64*, 2014.

[73] J. A. Fülöp, L. Palfalvi, G. Almasi, and J. Hebling, "Design of high-energy terahertz sources based on optical rectification," *Optics Express 18, 12311*, 2010.

[74] K.-L. Yeh, J. Hebling, M. C. Hoffmann, and K. A. Nelson, "Generation of high average power 1 khz shaped thz pulses via optical rectification," *Opt. Comm. 281, 3567*, 2008.

[75] C. Weiss, G. Torosyan, J. P. Meyn, R. Wallenstein, and R. Beigang, "Tuning characteristics of narrowband thz radiation generated via optical rectification in periodically poled lithium niobate," *Optics Express 8, 497*, 2001.

[76] K. Ravi, W. R. Huang, S. Carbajo, X. Wu, and F. X. Kärtner, "Limitations to thz generation by optical rectification using tilted pulse fronts," *Opt Express. 22, 20239*, 2014.

[77] K. Ravi, W. R. Huang, S. Carbajo, E. Nanni, D. Schimpf, E. P. Ippen, and F. X. Kärtner, "Theory of thz generation by optical rectification using tilted-pulse-fronts," *Opt Express. 23, 5253*, 2015.

[78] X. Wu, S. Carbajo, K. Ravi, F. Ahr, G. Cirmi, Y. Zhou, O. D. Muecke, and F. X. Kärtner, "Terahertz generation in lithium niobate driven by ti:sapphire laser pulses and its limitations," *Optics Lett. 39, 5403*, 2014.

[79] Y. S. Lee, *Principles of Terahertz science and Technology.* Springer, New York, 2009.

[80] S. G. Park, M. R. Melloch, and A. M. Weiner, "Comparison of terahertz waveforms measured by electro-optic and photoconductive sampling," *Appl. Phys. Lett 73, 3184*, 1998.

[81] G. Gallot and D. Grischkowsky, "Electro-optic detection of terahertz radiation," *J. Opt. Soc. Am. B. 16, 1204*, 1999.

[82] B. R. Steffen, *Electro-Optic Methods for Longitudinal Bunch Diagnostics at FLASH.* PhD thesis, Universität Hamburg, 2007.

[83] B. Schütte, *Laser based Terahertz field driven streak camera for the temporal characterization of ultrashort processes.* PhD thesis, Universität Hamburg, 2009.

[84] G. Gallot, J. Zhang, R. W. McGowan, T. I. Jeon, and D. Grisschkowsky, "Measurements of the thz absorption and dispersion of znte and their relevance to the electro-optic dtection of thz radiation," *Appl. Phys. Lett 74, 3450*, 1999.

[85] C. Winnewisser, P. U. Jepsen, M. Schall, V. Schyja, and H. Helm, "Electro-optic detection of thz radiation in litao3, linbo3 and znte," *Appl. Phys. Lett. 70, 3069*, 1997.

[86] Q. Wu and X. C. Zhang, "Ultrafast electro-optic field sensors," *Appl. Phys. Lett. 68, 1604*, 1996.

[87] J. Cooper and R. N. Zare, "Angular distribution of photoelectrons," *The Journal of Chemical Physics 48, 942 (1968);*, 1968.

[88] S. J. Smith and G. Leuchs, "Angular correlation in multiphoton ionization of atoms," *Adv. At. Mol. Phys. 24, 158*, 1988.

[89] S. Hara and M. Nakamura, "Determination of the photoionisation asymmetry parameter," *J. Phys. B: At. Mol. Phys. 19, L467-L469*, 1986.

[90] D. W. Chandler and P. L. Houston, "Two-dimensional imaging of state-selected photodissociation products detected by multiphoton ionization," *The J. Chem. Phys. 87, 1445*, 1987.

[91] C. Bordas, F. Paulig, H. Helm, and D. L. Huestis, "Photoelectron imaging spectroscopy: Principle and inversion method," *Review of Scientific Instruments 67, 2257*, 1996.

[92] M. N. R. Ashfold, N. H. Nahler, A. J. Orr-Ewing, O. P. J. Vieuxmaire, R. L. Toomes, T. N. Kitsopoulos, I. A. Garcia, D. A. Chestakov, S. M. Wu, and D. H. Parker, "Imaging the dynamics of gas phase reactions," *Phys. Chem. Chem. Phys. 8, 26*, 2006.

[93] M. Reid, *Velocity map imaging: from gases to surfaces.* PhD thesis, University of Manchester, 2013.

[94] A. J. R. Heck and D. W. Chandler, "Imaging techniques for the study of chemical reaction dynamics," *Annu. Rev. Phys. Chern. 46, 335*, 1995.

[95] M. J. J. Vrakking, "An iterative procedure for the inversion of two-dimentional ion/photoelectron imaging experiments," *Rev. Sci. Inst. 72, 4084*, 2001.

[96] G. M. Roberts, J. L. Nixon, J. Lecointre, E. Wrede, and J. R. R. Verlet, "Toward real-time charged-particle image reconstruction using polar onion-peeling," *Rev. Sci. Instr. 80, 053104*, 2009.

[97] S. Manzhos and H.-P. Loock, "Photofrafment image analysis using the onion-peeling algorithm," *Comp. Phys. Comm. 154, 76-87*, 2003.

[98] G. A. Garcia, L. Nahon, and I. Powis, "Two-dimensional charged particle image inversion using a polar basis function expansion," *Rev. Sci. Inst. 75, 4989*, 2004.

[99] C. Wheatstone, "An account of some experiments to measure the velocity of electricity and the duration of electric field," *Phil. Trans. R. Soc. Lond. 1834 124, 583*, 1834.

[100] M. M. Shakya and Z. Chang, "Achieving 280fs resolution with a streak camera by reducing the de ection dispersion," *Appl. Phys. Lett. 87, 041103*, 2005.

[101] U. Frühling, *Lichtfeld getriebene Streak-Kamera zur Einzelschuss Zeitrukturmessung der XUV-Pulse eines Freie-Elektronen Lasers.* PhD thesis, Unversität Hamburg, 2009.

[102] J. Itatani, F. Quere, G. L. Yudin, M. Y. Ivanov, F. Krausz, and P. B. Corkum, "Attosecond streak camera," *Phys. Rev. Lett. 88, 173903*, 2002.

[103] R. Kienberger, E. Goulielmakis, M. Uiberacker, A. Baltuska, V. Yakovlev, F. Bammer, A. Scrinzi, T. Westerwalbesloh, U. U. Kleineberg, U. Heinzmann, M. Drescher, and F. Krausz, "Atomic transient recorder," *Nature 427, 817*, 2004.

[104] I. Gorgisyan, *Femtosecond pulse length and arrival time measurement of hard X-Ray FELs.* PhD thesis, Swiss Federal Institute of Technology in Lausanne, 2016.

[105] S. A. Aseyev, Y. Ni, L. J. Frasinski, H. G. Muller, and K. J. J. Vrakking, "Attosecond angle-resolved photoelectron spectroscopy," *Phys. Rev. Lett. 91,*, 2003.

[106] D. E. Spence, P. N. Kean, and W. Sibbett, "60-fsec pulse generation from a self-mode-locked ti:sapphire laser," *Optics Lett. 16, 42*, 1991.

[107] D. Strickland and G. Mourou, "Compression of amplified chirped optical pulses," *Optics Communications 56, 219*, 1985.

[108] R. Brannath, *Zeitliche Verteilung von Auger-Electronen-Wellenpaketen aus der Photoionisation von Atomen.* PhD thesis, Universität Hamburg, 2016.

[109] *High performance Image intensifiers, Proxitronic detector systems.* available at `https://www.proxivision.de/datasheets/image-intensifier-general-information.pdf`.

[110] *MCP assembly, Hamamatsu.* Available at `https://www.hamamatsu.com/resources/pdf/etd/MCP_TMCP0002E.pdf`.

[111] *40 mm MCP Image Intensifiers, Proxivision.* `https://www.proxivision.de/adatasheets_11_04_2014/ProxiVision_40mm_Image_Intensifiers_20140221.pdf`.

[112] K. Wenig, "Matlab code for extraction of spectrum from camera image." Personal communication.

[113] M. Wieland, *Entwicklung hochauflösender röntgenoptischer Verfahrung für Hohe-Harmonische-Strahlung im extrem ultravioletten Spektralbereich.* PhD thesis, Rheinischen Friedrich-Wilhelms-Universität Bonn, 2004.

[114] R. Kalms, *Eine lasergestutzte Apparatur für Experimente zum magnetischen Linaerdichroismus in der Photoemission.* PhD thesis, Universität Hamburg, 2010.

[115] C. Brückner, *THz-optiken für Bildgebungssysteme.* PhD thesis, Friedrich-Schiller-Universität Jena, 2010.

[116] D. M. Slocum, E. J. Slingerland, R. H. Giles, and T. M. Goyette, "Atmospheric absorption of terahertz radiation and water vapor continuum effect," *J. Quan. Spec. Rad. Trans. 127, 49*, 2013.

[117] Y. Yang and D. R. Grischkowsky, "Broadband thz pulse transmission through the atmosphere," *IEEE transactions on terahertz science and technology.1, 264*, 2011.

[118] D. M. Neumark, "Slow electron velocity-map imaging of negative ions: Applications to spectroscopy and dynamics," *J. Phys. Chem. A. 112, 13287*, 2008.

[119] S. Kauczok, N. Gödecke, A. I. Chichinin, M. Veckenstedt, C. Maul, and K. H. Gericke, "Three-dimensional velocity map imaging: setup and resolution improvement compared to three-dimensional ion imaging," *Rev. Sci. Inst. 80, 083301*, 2009.

[120] X. Wu, Z. B. Qin, H. Xie, R. Wu, X. H. Ran Cong, and Z. C. Tang, "Collinear velocity-map photoelectron imaging spectrometer for cluster anions," *Chin. J. Chem. Phys. 23, 373*, 2010.

[121] P. Zhang, Z.-P. Feng, S.-Q. Luo, and Z. Wang, "Influence of the interaction volume on the kinetic energy resolution of a velocity map imaging spectrometer," *Chin. Phys. B 25, 033202*, 2016.

[122] S. J. Alexander, "Phosphor coated uvresponsive ccd image sensors," Master's thesis, University of Waterloo, 2002.

[123] G. A. Garcia, L. Nahon, C. J. Harding, E. A. Mikajlo, and I. Powis, "A refocusing modified velocity map imaging electron/ion spectrometer adapted to synchrotron radiation studies," *Rev. Sci. Inst. 76, 053302*, 2005.

[124] J. L. Wiza, "Microchannel plate detectors," *Nuclear Instruments and Methods . 162, 587*, 1979.

[125] M. Galanti, R. Gott, and J. F. Renaud, "A high resolution, high sensitivity channel plate image intensifier for use in particle spectrographs," *Review of Scientific Instruments 42, 1818*, 1971.

[126] G. Zanella and R. Zannoni, "The detective quantum efficiency of an imaging detector," *Nuclear Instruments and Methods in Physics Research A 359, 474*, 1995.

[127] U. Becker and D. A. Shirley, *VUV and soft X-ray photoionization.* Plenum press, 1996.

[128] S.-W. Huang, E. Granados, W. R. Huang, K.-H. Hong, L. Zapata, and F. X. Kärtner, "High conversion efficiency, high energy terahertz pulses by optical rectification in cryogenically cooled lithium niobate," *OPT. LETT. 38, 796*, 2013.

[129] U. S. Sainadh, H. Xu, X. Wang, W. C. Atia-Tul-Noor, Wallace, N. Douguet, A. Alexander Bray, I. Ivanov, K. Bartschat, A. Anatoli Kheifets, R. T. Sang, and I. V. Litvinyuk, "Attosecond angular streaking and tunnelling time in atomic hydrogen," *https://arxiv.org/ftp/arxiv/papers/1707/1707.05445.pdf*, 2018.

[130] A. K. Kazansky, A. V. Bozhevolnov, I. P. Sazhina, and N. M. Kabachnik, "Interference effects in angular streaking with a rotating terahertz field," *Phys. Rev. A 93, 013407*, 2016.

List of Figures

List of Tables

Abbreviations

DSMC Direct simulation Monte Carlo

EOS Electro-Optical Sampling

HFC Hollow fiber compressor

HHG Higher Harmonic Generation

IR Infra Red

OAR Open area ratio

OR Optical Rectification

PAD Photoelectron angular distribution

PCI Post Collision Interaction

PES Photoemission or photoelectron spectroscopy

PHD Pulse height distribution

POP Polar Onion Peeling

PSD Position Sensitive Detector

ROI Region of interest

SNR Signal to noise ratio

SPM Self Phase Modulation

TOF Time of flight

VMI Velocity Map Imaging

XUV Extreme Ultra Violet

Declaration on oath

I hereby declare, on oath, that I have written the present dissertation by my own and have not used other than the acknowledged resources and aids.

Hamburg, October 2018

- Mamuna Anwar -